Multi-Functional nano-structures in Nature: from optics to mechanics

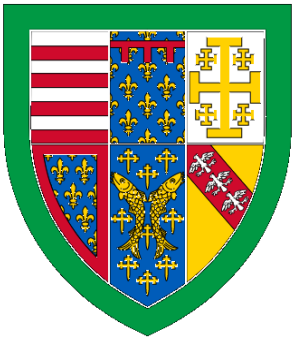

Yin Chang

Supervisor: Prof. Silvia Vignolini

Department of Chemistry/ Department of Engineering

University of Cambridge

This thesis is submitted for the degree of

Doctor of Philosophy

Queens' College Dec 2020

Declaration

I hereby declare that except where specific reference is made to the work of others, the contents of this dissertation are original and have not been submitted in whole or in part for consideration for any other degree or qualification in this, or any other university. This dissertation is my own work and contains nothing which is the outcome of work done in collaboration with others, except as specified in the text and Acknowledgements. The thesis contains fewer than 65,000 words, including abstract, tables, and footnotes.

Yin Chang

Dec 2020

Multi-Functional nano-structures in Nature: from optics to mechanics

Yin Chang

Abstract

Living organisms can process natural building blocks into hierarchical architectures under mild environmental conditions to produce varieties of architectures and display extraordinary properties. Some properties such as outstanding mechanical performances or vivid structural colours displayed by natural materials are difficult to be achieved in man-made materials because of the integration of structures from nano- to macro-scales. Biological and bio-inspired studies been attracting researchers in physics, biology, and engineering. However, such nanostructures are often studied in the context of a specific function by different communities and rarely intersect. This thesis aims to combine spectroscopic and mechanical analyses of different types of natural nanostructures. My comparisons on spectra and nanomechanics of helicoidally arranged cellulose microfibrils in the cell walls of *Pollia condensata* fruits shed light on the origin of the chirality assembling in the plant cell walls. By studying the structural colours developed in the close affinity of *Pachyrhynchus sarcitis* weevils and their first filial generations, I understand the hereditary characteristics of these photonic nanostructures. Finally, my comparison study on the mimicry pair of *Pachyrhynchus nobilis* weevils and the *Doliops similis* longhorn beetles reveals the role of structural colour on the co-evolved traits.

Acknowledgements

I would like to acknowledge the help of my co-supervisor Prof. Silvia Vignolini and thank her for the training, inspiration and supports. I'm grateful to Cambridge Trust Scholarship and Prof. Silvia Vignolini for additional funding.

I would also like to acknowledge the help of Prof. Hui-Yun Tseng, Dr Richard Langford, Dr Yu Ogawa, Dr Rox Middleton, Dr Miranda Sinnott-Armstrong, Dr Richard Parker, Dr Olimpia Onelli, who contributed scientifically to the projects presented in this thesis as specified in the text, and the biophotonics research community whose work motivated this research. I would like to thank Dr Olimpia Onelli, Dr Mike Casford and Dr Richard Langford for their patience in helping me and developing my lab skills and especially Dr Yu Ogawa and Prof. Silvia Vignolini for working together closely on all the projects listed in the thesis.

I'd like to thank all the other members of the Bio Inspired Photonics group for their supports, those mentioned above and also Dr Johannes Haataja, Dr Lisa Steiner, Dr Bruno Frka-Petesic, Dr Hsin-Ling Liang, Dr Floriana Misceo, Dr James Dolan, Dr Lukas Schertel, Dr Han Yang, Aurimas, Axel, Mélanie, Clement, Thomas, Gea, Sally, Laura, Junyoung, Zihao, Tianheng, Xiaotian, Zhen, Gianni, Cyan, Alyssa, John.

Finally, I am grateful for the supports and love from my family.

List of Figures

List of Tables

Contents

Outlines of the thesis

This thesis tackles the subject of structural materials in nature with a focus on the analyses of optical and mechanical properties. The thesis is structured as follows:

Chapter 1 introduces up-to-date research on structural colours and structural mechanics in organisms. Discussions from the physics behind the outstanding properties to their relationships with hierarchical structures are included.

Chapter 2 organizes the theoretical background of light-matter interference and structural mechanics.

Chapter 3 introduces the experimental and computational techniques necessary to image nanostructures and to characterize optical properties and mechanical properties.

Chapter 4 compares the nano-mechanics, optical properties and distributions of cells with opposite chirality in the fruits of *Pollia condensata*.

Chapter 5 presents the hybridized colouration in *Pachyrhynchus sarcitis* and hereditary phenotypes of structural parameters of the three-dimensional photonic crystals.

Chapter 6 compares the sympatric Batesian pair of *Pachyrhynchus nobilis* and *Doliops similis* from the aspects of microstructures and optical and mechanical responses from nano- to macro-scales.

Chapter 7 summarises the main findings of the thesis and provides a perspective on future works.

Appendix organizes the three-dimensional photonic crystals found in the two superfamilies in Coleoptera insects: Curculionidae and Cerambycidae families.

Chapter 1
Introduction

This chapter begins with an introduction of structural materials found in living organisms including a literature review on the recent interdisciplinary approaches used to study structural colours and structural mechanics in natural architectures.

In specific, the commonly found architectures responsible for structural colours are categorized by the dimensions, with a special focus on one-dimensional and three-dimensional photonic crystals. Representative organisms in each structural category are discussed. The extraordinary mechanical responses of biological materials and their unique structural designs are introduced. Finally, I listed some examples of bio-inspired applications.

1.1 Functional architectures in nature

Living organisms develop complex hierarchical structures over millions of years of evolution. A huge variety of nanostructures with arbitrary morphologies have been found in different tissues of many living species. These special architectural designs have been speculated to serve for several functions including sexual selections [1], territorial displays [2], defence, [3,4] camouflage [5–9], thermoregulation [9–11], self-cleanness, [12,13] or a mixture of the above. For example, the non-toxic *Heliconius* butterflies intimidate predators by developing a similar appearance on the wings as the toxic *Heliconius* butterflies. In addition, such structures also provide self-cleaning functions on the *Heliconius*'s wings [14]. Another example is *Copris ochus* beetles. They developed hexagonally arranged trabeculae and pore canals in the elytra, which make them lighter and provide high strength and impact resistance [15].

In 1859, Charles Darwin set out his theory of general principle natural selection. This implies some architectural designs developed in organisms might fulfil specific biofunctions. D'Arcy Wentworth Thompson's publication "On Growth and Form" in 1917 [16] was the first to analyse biological structures with engineering models which opened up a new interdisciplinary field of structural biological materials. During the 20th century, numerous biological materials from plants to the animal kingdom have been investigated. These intricated and diverse structures in nature are mainly constructed by simple skeletal biopolymers with different levels of mineralization. Therefore, biological materials have sparked worldwide attention as an inspiration for making miniatured and robust materials and devices. Commonly seen components in biological materials such as the skeletal biopolymers (Table 1.1) and inorganic minerals (Table 1.2) are provided [17–19]:

Table 1.1 A summary of the distribution, structures and functions of biopolymers in biological materials (Adapted from Chen *et al.* [20])

	Distribution	Structure	Major functions
Polysaccharides			
Chitin	The exoskeleton of crustaceans, insects, squid beaks	Long-chain	Structural support, Protection
Cellulose	Plant cell walls	Long-chain	Structural support
Proteins			
Collagen	Bone, teeth, tendons, vessels	Fibrous, triple helix	Structural support, connection
Keratin	Hair, nails, claws, bird beaks, feathers, horn, hooves	Fibrous, α-helix or β-sheet	Protection, strengthening, water barrier
Elastin	Skin, ligaments, lungs, artery walls	Fibrous, random coil	Connection, shape retention
Resilin	Insect wing hinges	Fibrous, random coil	Resilience
Abductin	Hinged ligament of bivalve molluscs	Fibrous, random coil	Compressible elasticity
Fibroin	Silkworm silk, spider web	Fibrous, β-sheet	Toughness, flexibility
Actin	Muscle, cytoskeleton	Globular	Movement, structural support
Tubulin	Microtubule in cytoskeleton	Globular	Transport, movement

Table 1.2 Common minerals in biological systems. Adapted from Chen et al. [20]

Mineral	Formula	Distribution
Calcium carbonate	$CaCO_3$	Mollusc shells, eggshells, sponge spicules
Hydroxyapatite	$Ca_5(PO_4)_3(OH)$	Bones, teeth, osteoderms
Calcium oxalate	CaC_2O_4	Plants
Calcium sulphate	$CaSO_4$	Jellyfish larvae
Dolomite	$CaMg(CO_3)_2$	Sea urchin spicules and teeth
Silica (hydrated)	$SiO_2 \cdot nH_2O$	Diatom exoskeleton, sponge spicules
Ferrihydrate	$5Fe_2O_3 \cdot 9H_2O$	Ferritin (animals), plants
Greigite	Fe_3S_4	*Crysomallon squamiferum* foot
Iron (III) oxide/hydroxide	FeOOH	Chiton and limpet teeth
Magnetite	Fe_3O_4	Mollusk radula, bacteria
Pyrite	FeS_2	*Crysomallon squamiferum* foot
Atacamite	$Cu_2Cl(OH)_3$	*Glycera dibrianchiata* jaw
Barium sulfate	$BaSO_4$	Algae

The integration of different hierarchical levels in biological materials creates synergistic effects on their astonishing bulk properties. For example, the chitin biopolymers in insects and the cellulose biopolymers in plants are both colourless and light-weight polysaccharides [20]. However, once they are organised into the helicoidal structures in plant cell walls or in insects' exoskeletons, such fibrous composites produce circularly polarized colours [21,22] and excellent mechanical properties [23,24]. Biofunctions of the mechanical properties have been proposed to serve as a matrix for growing epicarp cells of plants [25], or an armour for protecting soft tissues in insects [26]. However, the significance of optical properties of helicoidally structured tissues remains obscure. First, the reflecting light produced by helicoids in nature can range from ultraviolet to infrared region [27]. Second, evidence of animals' sensory systems to detect circularly polarized light is lacking [25,28].

How organisms control material structures and compositions from atomic to macroscopic scale is intriguing. Here, I introduced the current understanding of the formation of some biological photonic structures. The morphogenesis of helicoidal structures has been proposed to be controlled actively by biological forces [29,30], or passively by physical forces [24,31]. In addition, in the secondary cell walls of plants, hemicellulose is proposed to guide the cellulose orientation [32–36].

The formation of three-dimensional photonic crystals in insects has been a popular topic recently, so far our understanding is based on the studies of butterflies' wing scales. Each wing scale is a cellular extension from the wing epithelium [37], and the membrane-cuticle units fill in the spaces around the smooth and rough endoplasmic reticulum membrane and form a gyroid network [38,39]. The endoplasmic reticulum system and the

plasma membrane templates are degraded as the cell dies off leaving the single gyroid of cuticles.

Studies of the structural properties in biological systems may improve the understanding of nature' solutions to environmental challenges, and some might provide novel ideas to solve problems we face in our society. However, many of the properties exhibited by biological materials are still challenging to be achieved with man-made materials mainly because highly hierarchical structures require very precise manipulation at different length scales. In the late twenty years, 3D printing, laser holography and lithography have been developed progressively offering effective industrial approaches for manufacturing complex topologies. These new techniques allow researchers to fabricate structures at microscales and to mimic structures of biological materials in three dimensions [40]. However, fabricating materials with such top to down methods is still challenging when nanoscale control is required [41]. Nowadays, while some researchers are making effort to enhance the spatial resolution or simplify the fabrication steps of the top to down techniques, some other researchers are trying to develop the bottom-up self-assembly of nanostructured materials [42–46].

In the following sections, few selected functional structures in nature such as one-dimensional multilayer structures, helicoidal structures, and three-dimensional structures are introduced. Studies on their outstanding optical properties or mechanical properties were reviewed.

1.2 Structural colours

Colours can be produced either *via* absorption or *via* interference mechanisms. Colours generated by these two different mechanisms can vary in hue, brightness, and saturation. For example, colours created by pigments are usually matt and dull: the light that is not absorbed by the pigment molecule is reflected and scattered away from the object and detected by the observer [47,48]. In contrast, structural colours often appear very metallic and angularly dependent as they result from constructive interference of multiple reflected light beams. In many biomaterials, both pigmental and structural colours are used to create synergetic effects [22,49,50].

Unlike pigmental colours which usually fade quickly after the organisms' deaths, structural colours can be preserved for years [51,52]. Moreover, structural colours can create patterns and angle-dependent colouration (iridescence) without using different materials [53]. The architectures responsible for producing structural colours are defined as photonic crystals [54]. Photonic crystals are usually made up of periodically arranged dielectric materials [53,55]. The periodic structures generate a specific energy band and forbid specific electromagnetic waves to propagate inside the structures. The forbidden light with a specific range of wavelength is then reflected out of the structures giving rise to the object colouration [56].

Structural colours can be observed in our everyday life, examples are the blue colour of the sky, the white of clouds, the rainbow colouration in soap bubbles and oil trails [57]. Vibrant structural colours are also commonly found in organisms across taxa from bacteria colonies [58], vertebrates [59–61], insects [62–65] and to plants [48,66]. The study of structural colours has a long history and the earliest record can be traced back to the 17th century in 'Micrographia' and 'Opticks' written by Hooke and Newton on their

observations of feathers of peacocks and soap bubbles [57,67]. In 1859 Darwin established the concept of natural selection, where he proposed that the structural colours have been believed optimized results for species over the millions of years of evolution [68]. In the 19th century, when the theories of the electromagnetic wave were established [69], the fundamental physics behind structural colours such as reflection, refraction, interference and diffraction started to be understood [53,70,71]. Since then varieties of photonic crystals in nature and their colour production mechanisms have been widely explored [19,48,72–76]. Their structures can vary in dimensions, geometries, or level of order resulting in diverse visual effects [77–79].

Some optical devices and engineering materials have been inspired by these designs also utilized structural designs to produce colours and adjust the optical properties. Examples can be found in light-emitting diodes [80], optical fibres [81], laser [82], and cosmetics [19].

1.2.1 Structural colours from one-dimensional photonic structures

One-dimensional photonic crystals are one of the commonly seen photonic structures in nature. Such structures are often developed in the epidermis of plants, insects or animals. These structures are defined as one-dimensional because the periodic modulation of the refractive index is only in one direction.

The periodicity in one dimension gives rise to the metallic and angle-dependent nature of reflection colours in some organisms [22,83]. The range of iridescent colours can be narrow spanning only two to three colours [48,84], or can be broad covering the entire visible light wavelengths [22,83,85,86]. Colour production mechanisms of such one-dimensional photonic crystals include diffraction gratings or multilayers (Figure 1.1). While colours generated from diffraction gratings or multilayers are based on different

physics, they both can generate light in a broad range of spectra and with iridescent effects.

A diffraction grating is formed by nano-scaled periodic arrays on a surface. Because the phase of a wave is a function of its frequency (wavelength), the ordered slits disperse the incident white light into constituent wavelengths (as illustrated in Figure 1.1A). Variations of diffraction grating iridescent colours can be explained by different reflection spectral orders, from zero-order (pure specular reflectance) to high-order. In nature, colours generated from diffraction gratings are commonly seen in several species (examples are given in Figure 1.1C). Iridescence results from diffraction gratings can be seen in the long rows of cells in striated muscle or scales of snakes (*Xenopeltis unicolor*). Some flower petals such as *Hibiscus trionum* can also generate colours by a diffraction grating, but the iridescence is less visible to humans eyes [87,88]. Diffraction gratings are also commonly seen on the exoskeleton of arthropods such as the specialized scales of peacock spiders (*Maratus robinsoni*). [85], or many beetles in the *Aglyptinus tumerus* in scarabdae families [22].

Multilayers structures are generally composed of a stack of alternating materials with a different refractive index as schematically depicted in Figure 1.1B. When light propagating inside such structures is reflected at each interface, such reflections can interfere either constructively or destructively depending on their phase difference.

Variations of one-dimensional multilayers so as the diversities of produced visual colours are found in different species (Figure 1.1D). For example, by adjusting the arrangement and thickness of layers, species can create reflection light of wavelengths in a range of narrow bandwidths (narrowband) or broad bandwidths (broadband). The narrowband multilayer structures are formed by stacks of layers with high and low

refractive index, and each layer and stack has approximately the same thicknesses arranged periodically [89,90]. Interactions of incident light and narrowband multilayers lead to a limited range of wavelengths being reflected, so a specific colour is generated. Such narrowband multilayers are the most commonly found structures in beetle elytra [19,72,75,91] and an example of the metallic and iridescent green in *Chrysochroa fulminans* beetles is produced *via* this multilayer structure (see Figure 1.1D). These structures are formed during the development of insect integument that epidermal cells secrete layers of cuticles with different refractive indices.

Broadband multilayers, on the other hand, produce a wide range of reflection wavelengths and generate metallic gold or silver colours. In such structures, the thickness of the alternating layers is varied with the stacks. Three different representative models of broadband multi-layered structures are found in nature (Figure 1.1D): a chirped stack model in the elytra of *Chrysina aurigans* and *Chrysina limbate* [92,93], a chaotic structure model in the scales of silvery fish [94], and a combination model in the scales of herring fish [95].

The chirped stack comprising of gradient decreased thickness of layers are found in elytra of beetles of *Anoplognathus parvulus*, *Aspidomorpha tecta* [50], *Plusiotis resplendens* [96], *Chrysina aurigans, Chrysina limbata* scarab [92] and are responsible for gold and silver appearance of their elytra. The chaotic model consisting of randomly sized layers of high and low refractive index is found in the skin of the hairtail and the ribbon fish [89,94] and is responsible for the vivid silver colour. The combination model combines two narrowband multilayer stacks with each grouped stack reflects certain ranges of wavelengths. The combination of two stacks then gives rise to an overall broad range reflection of wavelengths. Such designs were proposed to benefit herring

for camouflage functions because the on-axis reflection colours make them invisible when swimming with a broad tilt angle (30-140^{o}) [95,97].

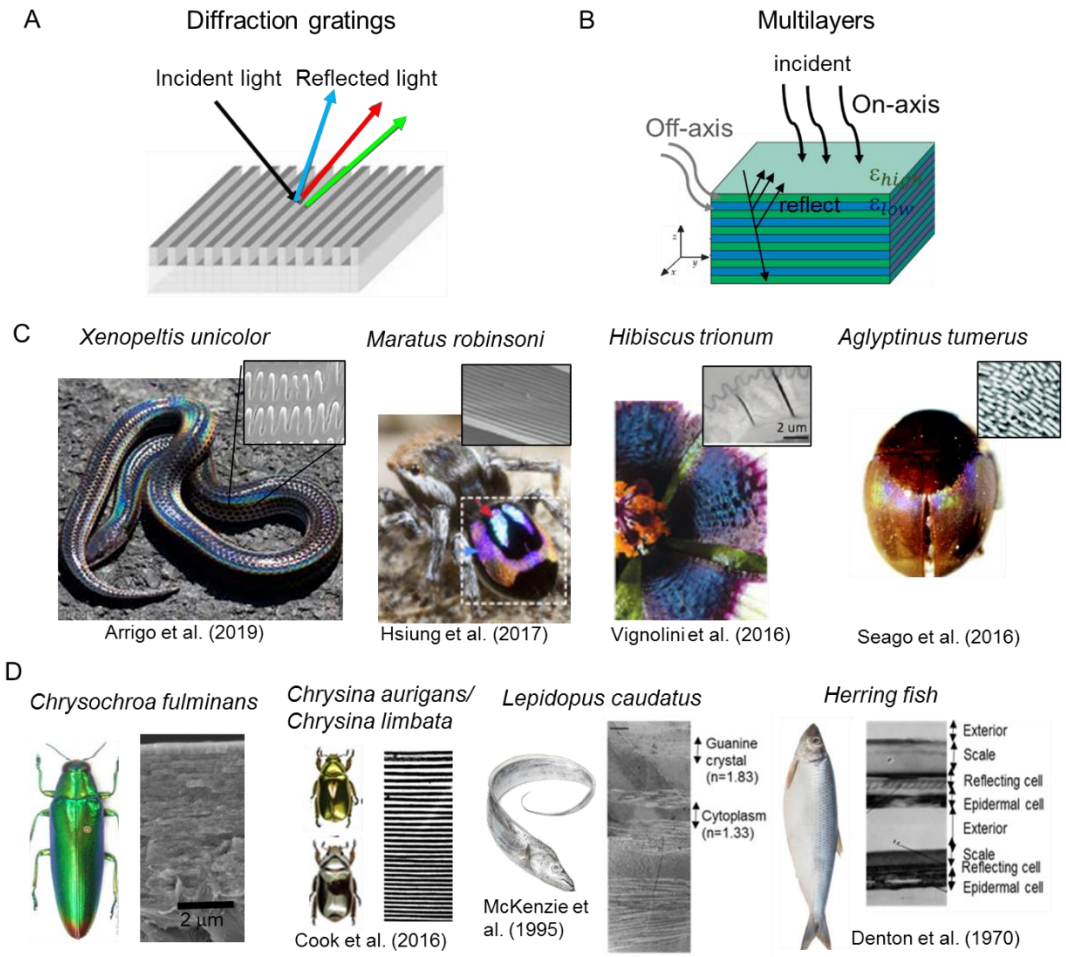

Figure 1.1 One-dimensional photonic crystals and the produced structural colours in nature. (A) Diffraction gratings are periodic arrays found on (C) the epidermal cells of snakes [98], spiders [85], flower petals [99], and scarab beetles [22]. (B) Multilayers are laminae with altered dielectric medium with high refractive index (ε_{high}) or low refractive index (ε_{low}). Narrowband multilayers are commonly seen in (D) the elytra of beetles such as *C. fulminans*. Broadband multilayers usually produce golden or silvery colours are found based on one of the three models: the chirped model in elytra of *C. aurigans* and *C. limbata* [92,93]. The chaotic model in the scales of ribbonfish [94]. The combination model (quarter-wave model) in the skin of herring fish [95].

1.2.2 Structural colours from three-dimensional photonic structures

Three-dimensional photonic structures are responsible for the structural colours of several natural tissues. In three-dimensional structures, the periodicity spans all three dimensions. Such structures are highly ordered in space and can reflect different colours in different directions of observation. Naturally occurring three-dimensional photonic crystals are commonly found in the scales of butterflies [38,100,101], beetles [62,63], in the feathers of some birds [102], and in algae [103]. Interestingly, most studied species have cubic based crystals which are formed by many biopolymeric units repeated equally along three dimensions in space. Some representative cases are shown in Figure 1.2. More discussions on diamond structured [62,63] or opal structured networks in beetles' scales are included in Chapter 5 and Chapter 6 [104].

As for one-dimensional periodic structures, three-dimensional ones reflect different colourations in the function of the angles of observations. However, such iridescence can be reduced, that is, the angle-independent and single coloured appearance can be obtained with polycrystalline structures of the photonic crystals. As an example, the green colour of the scales of *C. rubi* is angle-independent. Such non-iridescent colours are produced by gyroid photonic crystal structures organised in domains with different orientations to the neighbouring domains (see Figure 1.2). A similar non-iridescent colour producing mechanism is found in the scales of *P. sarcitis* for which the yellow colour is generated by polycrystalline diamond photonic crystals [62]. Gyroid and diamond structures are both formed with continuous phases of cuticular proteins and air. How nature forms these structures is not yet well understood, but these minimal surfaces of the two geometries imply possible self-assembling processes by phases separation [45,62,105,106]. Opal structures are commonly found in the scales of longhorn

beetles in Cerambycidae family. Different from the gyroid and diamond photonic crystals, these opal structures are formed with non-continuous phases of close-packed cuticular nanoparticles and air [104,107]. Detailed structure parameters of studied photonic crystals of beetles in this family are organized in Appendix Table S2.

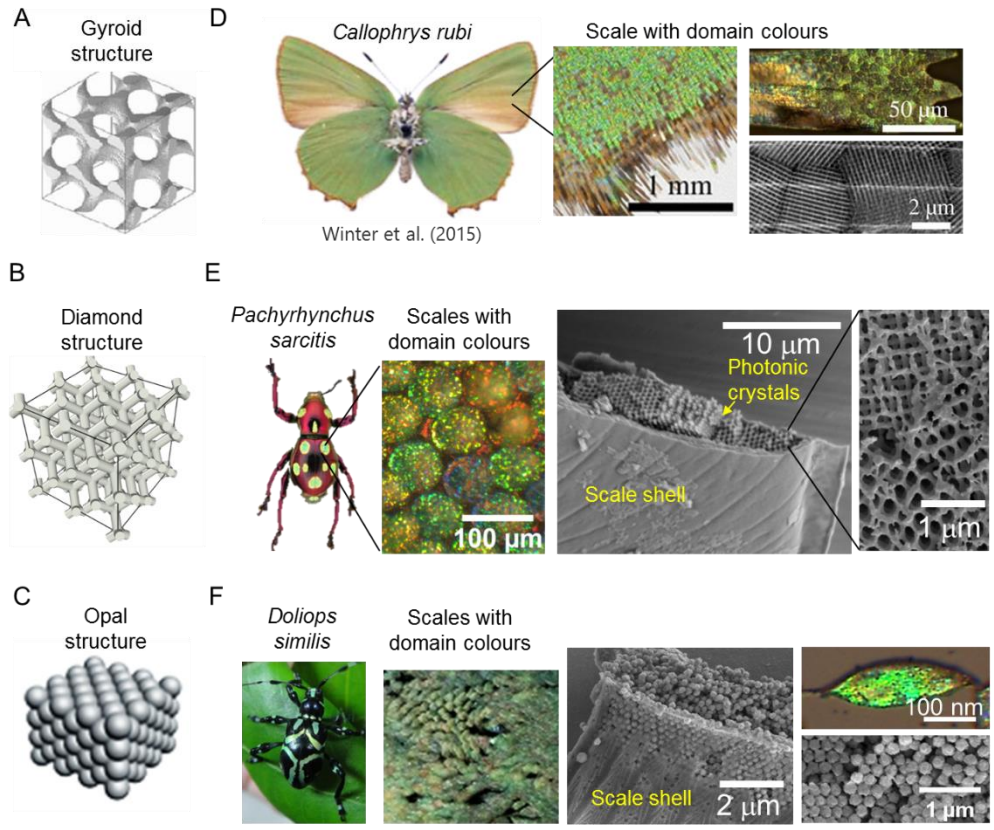

Figure 1.2 Three-dimensional photonic crystals in nature. (A) Single gyroid structures in (D) the scales on the wings of the butterfly *Callophrys rubi.* Domain structures are found in each scale covered by ridges [101]. Images are adapted from the publication of Winter et al. with the author's permission. (B) The diamond structures in (E) the scales of *Pachyrhynchus sarcitis*. Domain structures with differently oriented crystals are wrapped in each plate-like scale (this study). (C) The opal structures are found in (F) the needle-like scales of *Doliops similis*. The structure is composed of many spherical particles (this study).

1.3 Mechanical behaviours

In the year of 1999, Ashby introduced the idea of material property charts by plotting two selected mechanical properties (such as mechanical strength, toughness, Young's modulus, density, etc.) of different classes of materials (engineering metals, polymers, ceramics, composites and biological materials) on the same chart. Materials in the same class are drawn in one cluster. The charts are helpful to identify material groups and suggest materials to resist particular modes of mechanical loading [108,109]. Biomaterials generally have lower density and greater property variations than the engineering materials that the stiffness of biopolymers can span from 0.01 to 100 GPa while the stiffness of engineering polymers is up to 10 GPa.

In addition to low density, biological materials also show unique relationships of fracture toughness and stiffness. Engineering materials show a banana curve on the toughness and stiffness relations due to the rule of mixing [110], which means there is always a trade-off between toughness and stiffness when making engineering composites [111]. In contrast, biological materials do not follow the rule of mixing and show no trade-off of mechanical properties. This is because highly mixed phases of skeletal polymers and mineralized matrices are found at almost every hierarchy level in biological materials, so biomaterials are always composite materials from nano- to macro-scales. Such high integration on the hierarchical structures allows them to possess high toughness without sacrificing stiffness.

For example, the secondary plant cell walls are composed of cellulose, hemicellulose, embedded into wrapped in a lignified matrix [109,112]. The insect cuticle contains chitin in a protein matrix. Such mixing phases show the extrinsic toughening mechanisms to stop the crack grows in the materials by deflecting cracks at complicated interfaces

[26,109,113,114]. Biopolymers can also toughen biological materials intrinsically by strong chemical bonds between different components and interfaces. Such strong connections between different phases and links with different hierarchy levels make biological materials hard to be broken [115–117].

These intrinsic and extrinsic mechanisms are successfully integrated to shield crack growth. It is thus the hierarchically structural designs that give rise to the striking mechanical performances of biological materials including the low density, widely spanned mechanical properties, and breaking constraints of the rule of mixing

1.3.1 Plywood structure

The plywood structure is commonly found in the skeletal extracellular tissues of animals and plants. It generally describes a fibrous composite with highly aligned fibres. For example, scales of *Pagrus major* fish [118] are composed of closely packed layers of collagen fibres with every adjacent laminate oriented 90° to each other. Such fibre arrangements enhance the plasticity of the scales. Another example is observed in the scales of *Arapaima gigas* fish. The scales are composed of a mineralized external layer with non-mineralized internal proteins arranged with adjacent laminates twisting with an angle of 75° [119]. Some other examples are found in reptilians. Reptilians develop leathery eggshells which are made up mainly of proteins with low mineral contents. In the case of turtle eggshells, such proteins consist of keratin biopolymers organised in a plywood structure with 90° rotation. Similar components are found in the snake eggshells, but the keratin fibres are randomly oriented. The plywood structured keratin proteins make the turtle eggshells much stiffer but brittle than the snake eggshells [120] (Figure 1.3).

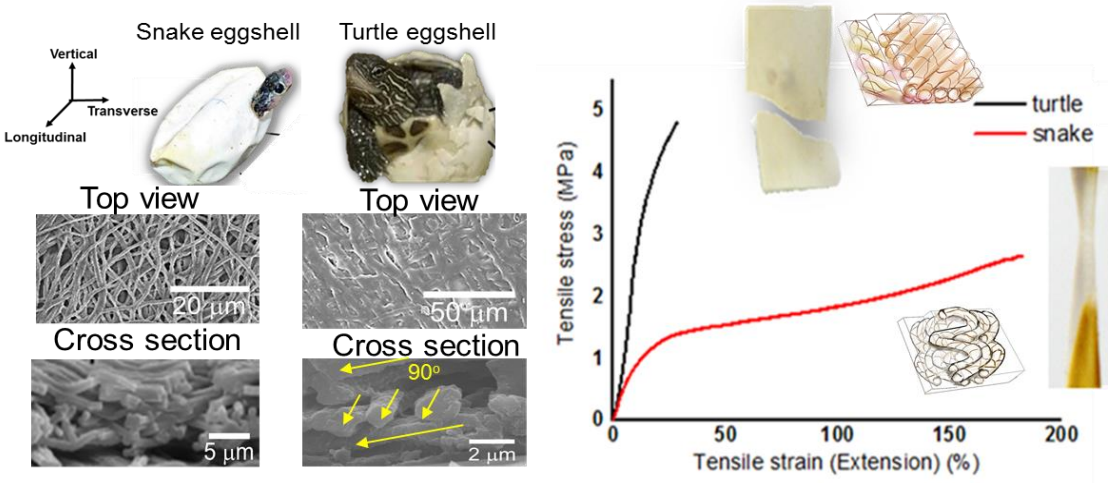

Figure 1.3 Oriented keratin fibres in the snake eggshells and the turtle eggshells. As shown in the top and the cross-sectional view of SEM images, keratin fibres are randomly oriented in the snake eggshells but are with plywood stacking with the angle of 90° in the turtle eggshells. From the tensile testing curves of the two types of leathery eggshells, the plywood arrangement of keratin fibres greatly enhanced the stiffness of turtle eggshells but lower the extensibility [120].

1.4 Helicoidal structure

Helicoidal structures are twisted plywood structures, where laminate fibres planes twist at a fixed and small-angle (~ 7- 20 degrees) [121–123]. Such structures have been widely found in plants, arthropods, invertebrates, and vertebrates [25,123–125]. The extraordinarily high impact strength and high toughness displayed by helicoidally structured materials are well-known. As an example, the helicoidally arranged chitin fibres in the shell of crustaceans give them a toughness three orders of magnitude higher than the unstructured ones [126]. Therefore, the helicoidal structures have been a commonly used strategy for making fibre reinforced engineering composites [122,127].

Helicoidal architecture can also exhibit special optical responses of circularly polarized colourations when the size of the helicoid is comparable with the light wavelength [128]. In fact, analogous to other multi-layered structures, the reflected colour of helicoidal architectures is determined by the periodicity of its structure. In the helicoidal structure,

each laminated fibre rotates gradually along an axis and shows the periodicity. The periodicity is defined as the pitch length, *p*, which is a distance of laminate with a rotating angle of 180°. With the measured pitch length of the helicoidal structure, the reflected wavelength can be calculated analogously to Bragg's law (see equation (2.21), development and verification of such analogy was done by Oseen [129] and de Vries [128]. Readers can follow detail mathematical derivation in [128–130].). In this thesis, I will use the convention that the handedness of the reflected light is defined the same as the spatial chirality of the helicoidal structure, so left-handed polarized light is reflected from structures with left-handed chirality (Figure 1.4). Depending on the chirality of the helicoidal structure, either left-handed or right-handed circularly polarised light is possibly generated.

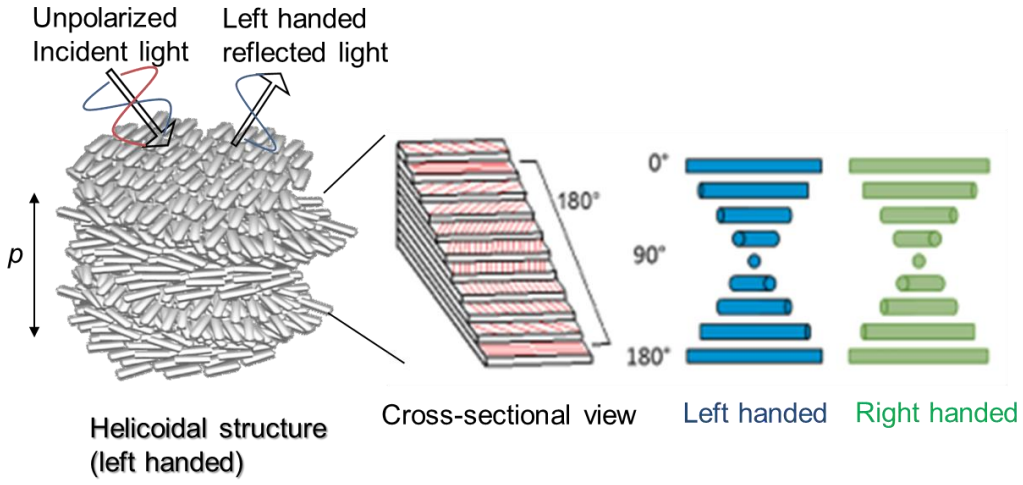

Figure 1.4 Laminated fibres twist at small angles and form a helicoidal structure with left-handedness. The reflection light is circularly polarised with left-handedness. The cross-sectional view of a helicoidal structure shows the periodicity formed by gradually twisted fibrous laminates with total angle of 180°. The periodicity is defined by the pitch length (*p*). Reflected wavelength is determined by the pitch length. Depending on the twisting directions of fibres, the helicoids can be either left-handed or right-handed.

Circularly polarised structural colouration is not commonly seen in nature [70,131–133]. These characteristics have been found only in certain systems such as animals in Stomatopod [132,133], beetles in Scarabaeidae family [134], and some fruits and ferns [21,66] (Figure 1.5). Figure 1.5A shows the representative examples of organisms with narrowband multi-layered structures displaying polarised colours. In *Chrysina boucardi* beetles, the birefringent chitin layers deposit helically in the elytra and make the elytra as circular polarisers which share optical analogy to a cholesteric liquid crystal with narrowband multilayers [22,135]. When unpolarized sunlight impinges on the elytra, left-handed polarised green is reflected. Similar left-handed polarised colours have been observed in other scarabs in rutelinae, melolonthinae, scarabaeinae and cetoniinae subfamilies. Those scarabs appear with a dark brown colour under the right-handed polarised filter which blocks out the left-handed green reflectance [70,131,134,136,137].

Cellulose fibres orient helicoidally in the cell walls of the fruits of *Pollia hasskarlii* and form a narrowband multi-layered structure. The cell walls, therefore, reflect intense colour under a left-handed polarized filter, but with no reflection under a right-handed polarized filter [21]. The *Plusiotis* species in the ruteline family also show circularly polarized light (Figure 1.5B, C). *Plusiotis optima* has a broadband multilayer structure reflecting intense silvery (reflectivity of 0.5) light under a left-handed polarized filter. However, the beetle shows a completely black exoskeleton (reflectivity of 0) under a right-handed polarized filter [136].

As discussed above, it can be observed that left-handed helicoidal structures seem to dominate in living organisms. Few exceptions are found in *Plusiotis resplendens* scarabs (Figure 1.5B) and *Pollia condensata* fruits (Figure 1.5D). *Plusiotis resplendens* scarabs have a broadband multilayer structure exhibiting shiningly gold under a left-

handed filter and intensely green under a right-handed filter [70,131]. This is due to two groups of helicoidal stacks with opposite chirality exist in the exoskeletons of *P. resplendens*. Both handed structures produce intense reflection colours with reflectivity of 0.32–0.35. The left-handed helicoids form a smaller pitch length producing green colouration with the reflection peak at 560 nm while the right-handed helicoids have a larger pitch give rise to orange colour with a reflection peak at 575–624 nm.

Pollia condensata fruits (Figure 1.5D) have both left-handed and right-handed epicarpal cells. Each cell only has one chirality in the cell wall, so the two types of cells take the role in producing colours under left or right polarized light respectively [66].

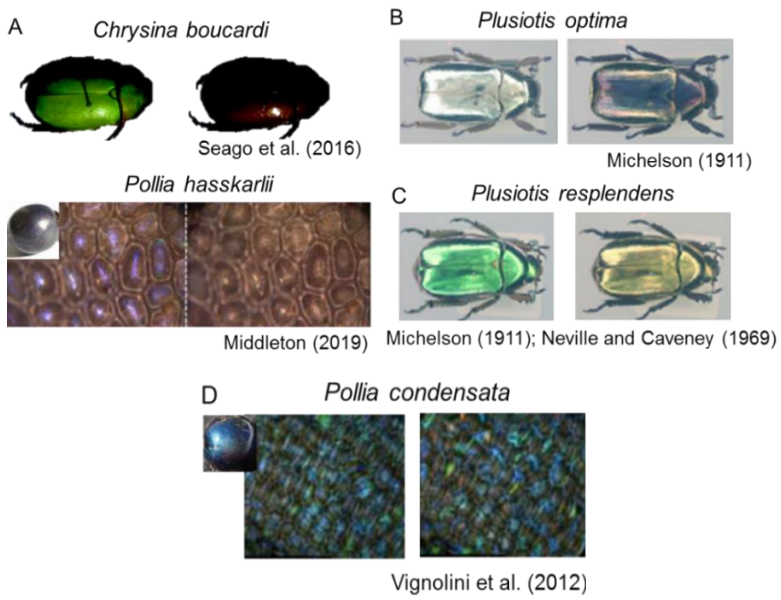

Figure 1.5 Circularly polarized reflectors in living organisms. (A) *Chrysina boucardi* [22,135] and *Pollia hasskarlii* fruits [21] have narrowband multilayers showing left-handed colouration. (B) *Plusiotis optima* having broadband multilayered structures displaying intense silver colours under a left-handed polarized filter while turning black under a right-handed filter [136]. (C) *Plusiotis resplendens* having broadband multilayered structures show intense but different colours under left and right polarized filters [70,131]. (D) *Pollia condensata* having left-handed or right-handed epicarpal cells show different visual appearances under left and right polarized filters [66].

Chapter 2.
Theoretical background

This chapter begins with the fundamental concepts of light-matter interactions. The theory of electromagnetic waves propagation in the inhomogeneous system is introduced and followed by a more detailed exaptation of the underlying physical principled describing structural colourations in the thin-film, one- and three-dimensional photonic crystals, polarised light.

I later introduced the fundamental concepts and relevant parameters used to characterise the mechanical properties of materials such as the stiffness for quantifying the elasticity, and the hardness for quantifying the resistance to contact stresses of a material. The contact mechanics involved in the nanoindentation technique, and the methodologies to derive the mechanical parameters from indentation tests were introduced. Finally, the constitution law for describing the elastic deformation (small strain) of fibre-reinforced composites were introduced.

2.1 Light-matter interactions

Interactions of light and solid-state materials can be classified into some general phenomena: reflection, scattering, absorption, refraction, and transmission. As illustrated in Figure 2.1, when light impinges on the top surface of a medium, some of the light is reflected back at the specular direction with a symmetric polar angle while the rest transmitted or diffracted through the medium. Light can be attenuated in intensity while propagating in the medium either *via* absorption or scattering. This mechanism is repeated at every interface.

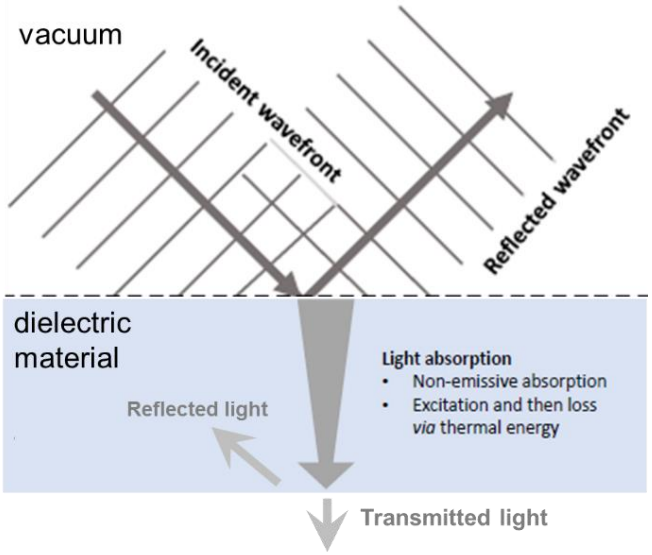

Figure 2.1 Four fundamental light-matter interactions: reflection, absorption, scattering, and transmission.

Absorbance (A), reflectance (R), and transmittance (T) are usually defined as quantifying the intensity of different light-matter interactions at a macroscopic level. The parameters are generally defined as the energy of light after interactions divided by the energy of incident light. For example, the absorbance can be evaluated through Lambert-Beer's law:

$$I = I_0 e^{-\alpha z} \tag{2.1}$$

$$A = -\log\left(\frac{I}{I_0}\right) = 0.434\alpha z \tag{2.2}$$

Where $I_0$is the energy of incident light, α is the absorption coefficient of the medium.

The energy of propagating light (I) decays with the propagating distance (z) in the medium. The absorption coefficient α is a function of the frequency of the light $\alpha(\omega)$, so the medium may selectively absorb a certain wavelength but not others. Scattering can be considered as an analogous term to absorbance by additionally considering the numbers of scattering units (N) and the scattering mean cross-section (σ):

$$I = I_0 e^{-N\sigma z} \tag{2.3}$$

The scattering cross-section is a function of the wavelength (frequency) of the light. For an elastic scattering of light by particles much smaller than the wavelengths of the radiation, the relationship of the scattering mean cross-section and the radiation wavelengths $\sigma(\lambda)$ can be described as Rayleigh scattering law:

$$\sigma(\lambda) \propto \frac{1}{\lambda^4}. \tag{2.4}$$

To quantify the reflection (R) and transmission (T) occurring at the interfaces of two media, we consider a beam of light incidents on a surface with an incident angle θ_i and an illuminated area of A as shown in Figure 2.2. Let I_i, I_r, and I_t be the flux densities of the incident, reflected, and transmitted light beams. $A\cos\theta_i$, $A\cos\theta_r$, and $A\cos\theta_t$ are the cross-sectional areas of the incident, reflected, and transmitted beams, respectively. Accordingly, the power of incident light is $I_i A\cos\theta_i$, similarly, the power of the reflected beam and the transmitted beam is $I_r A\cos\theta_r$ and $I_t A\cos\theta_t$, respectively.

According to the definition, parameters for quantifying different light interactions are likewise defined by dividing the intensity of light after interactions by the intensity of incident, the reflectance (R) and transmittance (T) by definitions can therefore be written as:

$$R = \frac{I_r A \cos\theta_r}{I_i A \cos\theta_i} = \frac{I_r}{I_i} \tag{2.5}$$

$$T = \frac{I_t A \cos\theta_t}{I_i A \cos\theta_i} = \frac{I_t \cos\theta_t}{I_i \cos\theta_i} \tag{2.6}$$

When light transports through different media, it changes the velocity of propagation. The relative velocity of light in different media is presented as a refractive index (n) which is the ratio of the speed of light propagating in a vacuum (**c**) to the phase velocity (**v**) or group velocity ($\mathbf{v}_g$) of light in a medium $n = \frac{\boldsymbol{c}}{\boldsymbol{v}}$. The refractive index determines the amount of light that is reflected at the interface (Fresnel's equations), or how much the path is bent when light enters into a medium (refraction). This phenomenon is described by Snell's law of refraction, and in the case of Figure 2.2, Snell's law can be presented as:

$$n_i \sin\theta_i = n_t \sin\theta_t \tag{2.7}$$

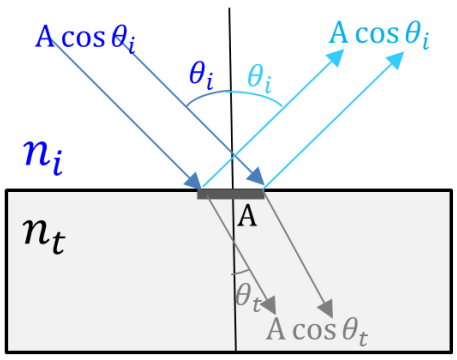

Figure 2.2 Reflection and transmission of incident light from the medium i with refractive index n_i to the medium t with refractive index n_t

Fresnel's equations calculate the reflectance and transmittance with known refractive indices of media and the angle of the light incidents on the interface. Therefore, for a light beam impinges on any linear, isotropic, homogeneous, non-magnetic media with the electric field perpendicular to the incident surface, the reflectance R and the transmittance T can be calculated as followed:

$$R = \left(\frac{E_r}{E_i}\right)^2 = \left(\frac{n_i \cos\theta_i - n_t \cos\theta_t}{n_i \cos\theta_i + n_t \cos\theta_t}\right)^2 \quad (2.8)$$

$$T = \left(\frac{E_t}{E_i}\right)^2 = \left(\frac{2n_i \cos\theta_i}{n_i \cos\theta_i + n_t \cos\theta_t}\right)^2 \quad (2.9)$$

E_i, E_r, E_t is the amplitude of the incident, reflected, and transmitted light.

The transmittance (T) can be calculated as equation (2.10) that considering the transmitted light is the rest light beam after light being reflected on the top (R_1) and the bottom surfaces (R_2) of a medium and attenuated in the medium:

$$T = (1 - R_1)e^{-\alpha z}(1 - R_2) \quad (2.10)$$

The absorption and refraction of a dielectric medium can be described by a single coefficient called the complex refractive index $\tilde{n}$ which is composed of the refractive index n as the real part and extinction coefficient κ as the imaginary part ($\tilde{n} = n + i\kappa$).

2.2 Polarised light

More in general, light is an electromagnetic wave and the description of light propagation require a vectorial approach. The superpositions of the two linearly polarised light waves (***Es***, ***Ep***) travelling along the same direction with the same frequency will result in a linear, circular or elliptical polarisation light depending on the phase difference of the source waves (Figure 2.3).

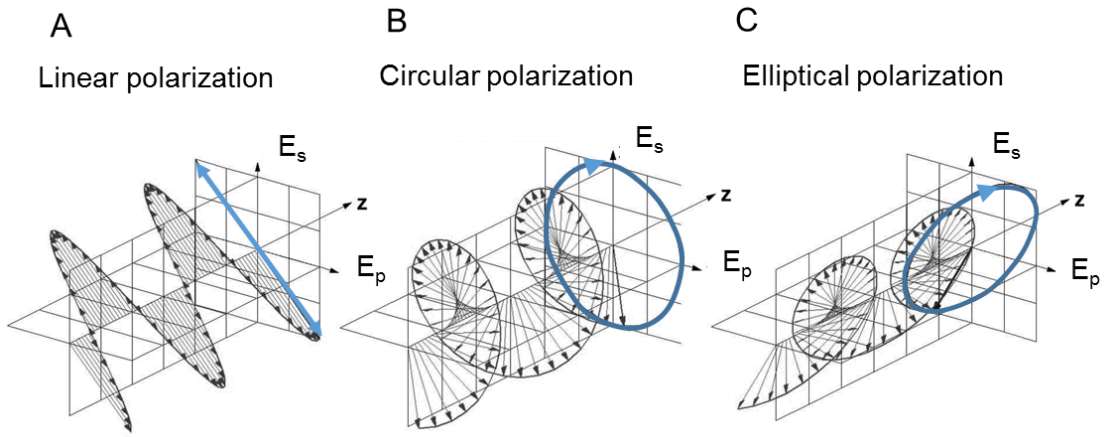

Figure 2.3 Three polarization states (A) linear, (B) right circular, and (C) elliptical polarization. Images are adapted from *Optical Properties of Solid* [138].

Natural light sources generally consist of a large number of randomly oriented atomic emitters, so they are considered unpolarised. Each excited atom radiates a polarised wave, and the changes of polarisation take place so rapidly that the resultant polarisation states are indiscernible.

If the natural light impinges on a polariser, polarised light may be generated. Polarisers are associated with light propagating in an asymmetric process such as selecting a particular polarisation state and discarding all the others. This asymmetry can come in one of the four fundamental physical mechanisms: reflection; dichroism; birefringence (double refraction); scattering.

2.3 Thin-film interference

When two or more waves propagate in the same space, the net amplitude at each point is the sum of the amplitudes of the individual waves. Consider two waves $\mathbf{E_1}, \mathbf{E_2}$ with the same amplitude of E_0 and frequency ω travel along the direction $\mathbf{k_1}$ and $\mathbf{k_2}$ in the same space as illustrated in Figure 2.4, the two waves can be expressed in a waveform:

$\mathbf{E_1}(\mathbf{r},\mathbf{t}) = E_0\cos(\mathbf{k_1 r} - \omega t + \delta_1)$ and $\mathbf{E_2}(\mathbf{r},\mathbf{t}) = E_0\cos(\mathbf{k_2 r} - \omega t + \delta_2)$. The net response is simply summing up the two waves because we only consider linear wave functions here. Therefore, the electric field intensity $\mathbf{E}$, at a point in space, arising from the separate fields $\mathbf{E_1}, \mathbf{E_2}$ of is given by: $\mathbf{E} = \mathbf{E_1} + \mathbf{E_2}$. The intensity of the net electric field is:

$$I = \mathbf{E}^2$$

$$= (\mathbf{E_1} + \mathbf{E_2}) \cdot (\mathbf{E_1} + \mathbf{E_2})$$

$$= \mathbf{E_1}^2 + \mathbf{E_2}^2 + \mathbf{2E_1} \cdot \mathbf{E_2} \qquad (2.11)$$

provided that $I_1 = \mathbf{E_1}^2$, $I_2 = \mathbf{E_2}^2$, and $I_{12} = \mathbf{2E_1} \cdot \mathbf{E_2} = 2\sqrt{I_1 I_2}\cos\phi$, equation (2.11) can be expressed as:

$$I = I_1 + I_2 + 2\sqrt{I_1 I_2}\cos\phi$$

$$\phi = \mathbf{k_1 r} - \mathbf{k_2 r} + \delta_1 - \delta_2 \qquad (2.12)$$

ϕ is the phase difference arising from a combined path length and initial phase angle of the two waves. From (2.12), we observe that the amplitude of reflected light is the sum of multiple beams which is decided by the amplitude of each beam and the phase difference of them.

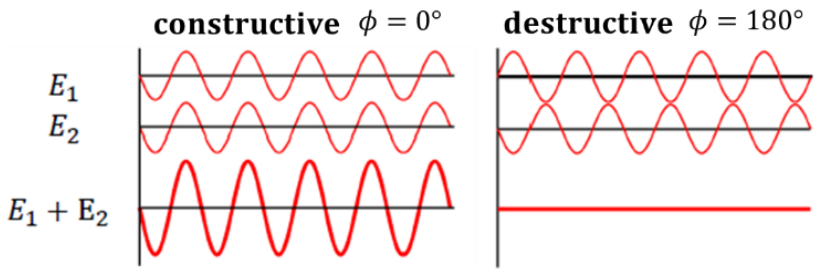

Figure 2.4 The interference of two waves. If the two waves are in phase, constructive interference is created resulting in a wave of greater amplitude. If the two waves are out of phase (180°), they create destructive interference.

If $\phi = 0^o$, the two beams are in phase (as the left panel in Figure 2.4), the combined light is relatively strong with the maximum intensity resulting in a constructive interference:

$$I_{max} = I_1 + I_2 + 2\sqrt{I_1 I_2} = 4I \quad (\text{if } I_1 = I_2 = I) \tag{2.13}$$

If the reflected beams have an opposite phase, that $\phi = 180^o$ (as the right panel in Figure 2.4), the resulting beam is attenuated with minimum intensity and forming a destructive interference:

$$I_{min} = I_1 + I_2 - 2\sqrt{I_1 I_2} = 0 \quad (\text{if } I_1 = I_2 = I) \tag{2.14}$$

The phase difference of the reflected light results from the different optical path length differences (OPD) of the multiple beams. The phase difference can be generally expressed as:

$$\phi = \boldsymbol{k} * OPD \pm \delta_{source} \tag{2.15}$$

Where $\boldsymbol{k}$ is the wavevector that $\boldsymbol{k} = \frac{2\pi}{\lambda}$

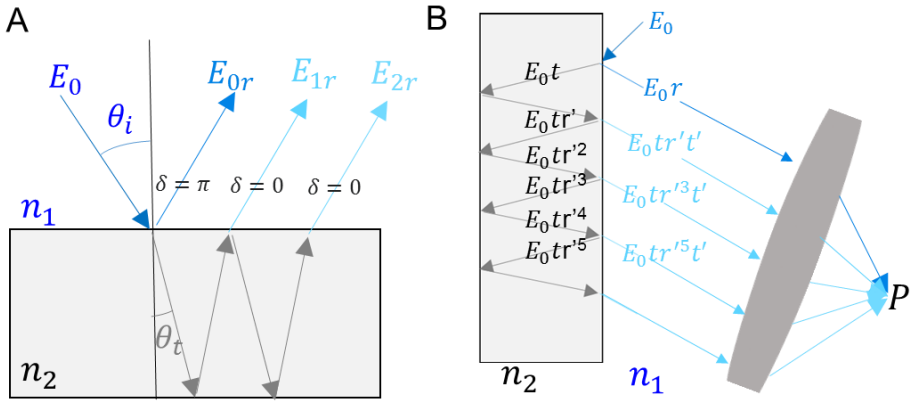

Figure 2.5 Thin film reflection and the net wave at point P by considering (A) two beams interference ($n_2 > n_1$) and (B) multiple beams interferences.

Light interference can occur in the optical system of the thin-film reflection (Figure

2.5). Consider two beams interference in Figure 2.5A that a light propagating through the medium 1 with lower refractive index n_1 enters in a thin film with higher refractive index n_2. The first reflection light E_{0r} from top surface of the film is out-of-phase by 180^o ($\delta_{source} = \pi$) of the incident beam E_0 due to traversing from the medium with a low refractive index to a higher refractive index. The second reflection light from the bottom surface E_{1r} generates a phase difference to E_0 due to OPD which can be calculated as:

$$OPD = 2n_2\, d\cos(\theta_2) \tag{2.16}$$

Inserting the $\delta_{source} = \pi$ of E_{0r} and OPD of E_{1r} into (2.15), the net wave at point P has the phase shift $\phi = k * OPD + \delta_{source}$. The conditions for interference can be quantitatively described as the following two equations:

$$\phi = m\lambda \quad \text{constructive interference}$$

$$\phi = (m - \tfrac{1}{2})\lambda \quad \text{destructive interference} \tag{2.17}$$

where m is so-called retardation meaning the numbers of phase difference ϕ

A similar approach can be applied to the case of interference between multiply reflected beams. At each interface, the decrease of the reflected beam at interfaces can be calculated by the reflection coefficient r' and transmission coefficient t and t'at the top and bottom surface, respectively (Figure 2.5B). If $n_2 > n_1$, the first reflection beam generates a phase shift of the source $\delta_{source} = \pi$ and reduces the amplitude by r' that $E_{0r} = r'E_0$ while the second, third, fourth, and successive waves will all be in phase. If the OPD of beams reflected from the bottom surface is always $m\lambda$, the net wave at point P is:

$$E_p = E_0 r' - \left(E_0 t r' t' + E_0 t r'^3 t' + E_0 t r'^5 t' + \cdots\right) = E_0 r' \left[1 - \frac{tt'}{\left(1-r'^2\right)}\right] \qquad (2.18)$$

In contrast, if the OPD of beams reflected from the bottom surface is always $m\lambda/2$, the net wave at point P is:

$$E_p = E_0 r' + \left(E_0 t r' t' - E_0 t r'^3 t' + E_0 t r'^5 t' - \cdots\right) = E_0 r' \left[1 + \frac{tt'}{\left(1+r'^2\right)}\right] \qquad (2.19)$$

For OPD other than the two extreme cases, the net wave is:

$$\begin{aligned} E_p = {} & E_0 r' + \left(E_0 t r' t' e^{-i\delta} + E_0 t r'^3 t' e^{-i2\delta} + \cdots + E_0 t r'^{(2N-3)} t' e^{-i(N-1)\delta}\right) \\ = {} & E_0 r' \left[1 + \frac{tt' e^{-i\delta}}{\left(1-r'^2 e^{-i\delta}\right)}\right] \end{aligned} \qquad (2.20)$$

From the two extreme cases (2.18) and (2.19), we observe the net wave is less intense than the incident beam if OPD matches $m\lambda$ while more intense if OPD matches $m\lambda/2$. General interference of multiple light beams can be expressed as equation (2.20). These three interference cases can also be illustrated on a phasor diagram as in Figure 2.6:

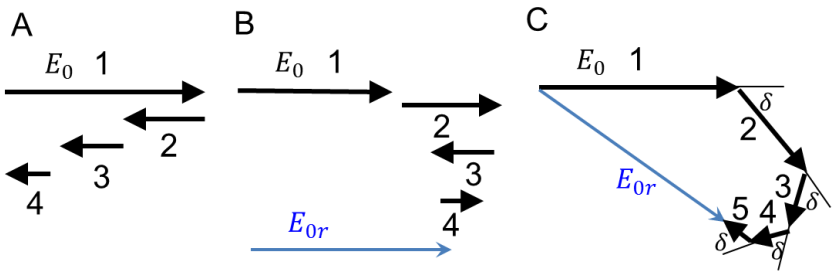

Figure 2.6 Phasor diagrams of multiple beams interference for (A) $OPD = m\lambda$ (B) $OPD = m\lambda/2$ (C) $k \cdot OPD = \delta$.

To sum up, the reflection peak and amplitude of the net wave are related to the wavelength of the incident light beam (λ) and the thickness (d) of the film. If the total phase shift is an integer multiple (m) of λ, then the reflected beams constructively interfere. In contrast, if the total phase shift is an integer multiplying to the half-

wavelength $\lambda/2$, the reflected beams destructively interfere. Different colours can be observed at a different angle of view and a different angle of illumination, or different positions in space (Figure 2.7). The different OPD results from either different angles of reflection (e.g. soap bubbles) or different thicknesses of the thin film (e.g. Newton's ring). The integer multiple (m) refers to retardations that can often be seen as the colour sequences generated through reflection.

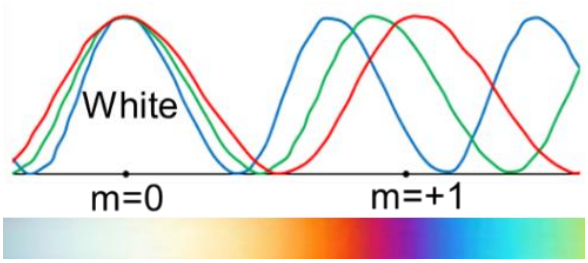

Figure 2.7 Colour sequences due to the retardation (m) of incoherent light source (white light). The orders refer to retardation.

It should be noted that interference will not happen if the path length of different light beams is too long. For example, the coherence length of sunlight is approximately one wavelength, and thus, two waves interfere only if their difference in optical paths is less than a few wavelengths.

2.4 Wave propagation in photonic crystals

This section focuses on the quantum physics of electrons in a solid. The basic optical properties of crystalline dielectrics and the concept of energy band structures are introduced. First, mathematic models and properties of crystal structures and the corresponding reciprocal lattices at k-space are derived. Second, basic notions of the electron theory of solids along with the realm of quantum confinement phenomena in low-dimensional systems are considered. Finally, the theory extends to the phenomena

in a periodically confined system which is the case of the light propagating in a material with a periodic dielectric property. Photonic crystal theory is presented through the analysis of field distributions in periodic photonic systems. This mathematical analysis is presented alongside physical electromagnetic principles which collectively, fully describe the origin of photonic band-gap properties.

2.4.1 Reciprocal lattice and Brillouin zone

The reciprocal lattice concept is fundamental in analytic studies of periodic structures, the reciprocal lattice represents the Fourier transform of a Bravais lattice. The Fourier transform of Bragg's diffraction from a crystal in real space (Figure 2.8A) to k-space (Figure 2.8B) reveals that the reciprocal vectors are the momentum difference between the incoming and the diffracted light. Assuming the incident beam with wavevector $\boldsymbol{k}$ is diffracted from the crystal plane with the plane distance of d which means it fits Bragg's law that:

$$2\,d\cos(\theta) = m\lambda \tag{2.21}$$

We plot the incident wavevector $\boldsymbol{k}$ and the diffracted wavevector $\boldsymbol{k}'$ at k-space as shown in Figure 2.8B and define a vector $\boldsymbol{G} = \boldsymbol{k}' - \boldsymbol{k}$:

$$\boldsymbol{k}' - \boldsymbol{k} = 2\boldsymbol{k}_{|} = 2\frac{2\pi}{\lambda}\cos(\theta) \tag{2.22}$$

By inserting (2.21) into (2.22), we derive the vector **G** when diffraction occurs:

$$\boldsymbol{G} = \frac{2\pi m}{d} \tag{2.23}$$

From equation (2.23), we find out Bragg's diffraction occurs when the reciprocal vector is an integer multiple of reciprocal lattice constant.

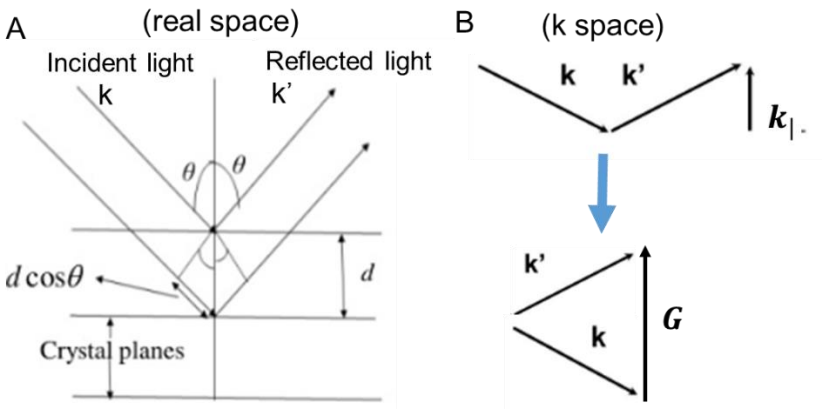

Figure 2.8 Bragg's diffraction from a crystal plane with lattice distance d at (A) real space and at (B) k-space.

The Brillouin zone is defined as the set of points in the k-space that can be reached from the origin without crossing any Bragg plane (wave diffraction will not happen). Therefore, those waves completely characterized in a single Brillouin zone refers to the allowed wave states that can exist and propagate in a periodic medium [138,139].

We can derive the Brillouin zone from the reciprocal lattice of photonic crystals and further reduce it to an irreducible Brillouin zone based on the crystal symmetry. Examples of deriving irreducible Brillouin zone from two-dimensional square lattice and three-dimensional FCC lattice are shown in Figure 2.9. Taking the square lattice as an example (Figure 2.9A), we Fourier transform the two primitive axes a_1, a_2 to k-space and the reciprocal lattice is still a square lattice with inverse lattice constant to the real space that $|b_1| = |b_2| = \frac{2\pi}{a}$. The connection of every point in k-space to the origin fits Bragg's diffraction law (shown as red lines in Figure 2.9A). By drawing a perpendicular bisector of the line joining the origin and another reciprocal lattice point (blue lines in Figure 2.9A), all blue lines form a small enclosed area at the centre (drawn in yellow). This enclosed region is defined as the first Brillouin zone which highlights the volume that is closer to the original point than to any other lattice point. By doing

so inside the yellow area (first Brillouin zone), no single vector can reach any Bragg plane. The irreducible Brillouin zone is the smallest unit for repeating in space to represent all reciprocal vectors. This irreducible unit can be constructed based on the symmetry of the lattice (as the red triangle circled by the high symmetry directions Γ-M-X).

Similar methods can be applied to different Bravais lattices such as the FCC lattice in Figure 2.9B. The primitive reciprocal lattice of FCC forms a BCC coordinate (blue spots in k-space). By drawing a plane (red lines) at every middle of the connecting line, the planes form an enclosed space which is the first Brillouin zone. The highly symmetrical planes and vectors of an FCC crystal are Γ- X-W-K- Γ- L-U-W-L-K|U-X, and they form a truncated octahedron as marked in Figure 2.9B.

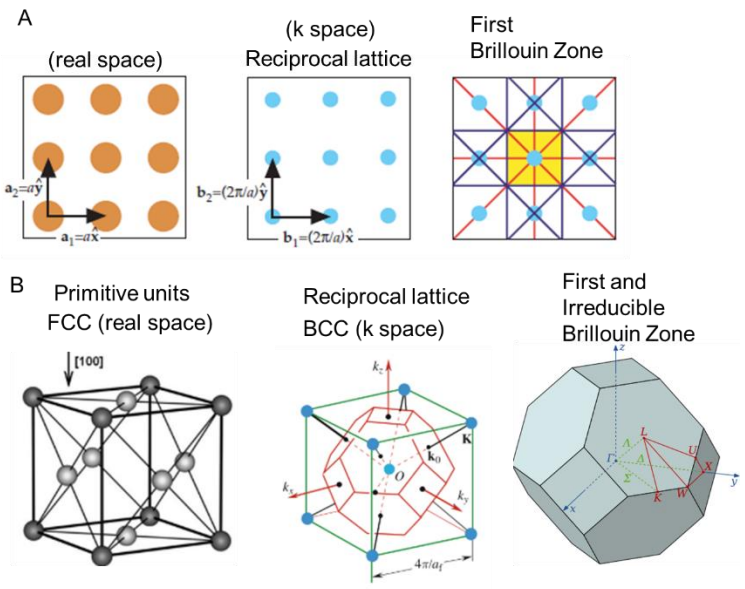

Figure 2.9 The reciprocal lattices (dots) and corresponding first Brillouin zones of (A) a square lattice and (B) an FCC lattice. The truncated octahedron is labelled for high symmetry lines and points. Images are adapted from *Photonic Crystals: Molding the Flow of Light* [139].

2.4.2 Bloch wave

Assume light propagates through a material with periodic refractive index in the same dimension k. By inserting the periodic potential $U(\boldsymbol{r}) = U\,(\boldsymbol{r} + \boldsymbol{T})$ into three-dimensional Schrödinger wave equation, the following two equations (2.24) and (2.25) have to be satisfied:

$$-\frac{\hbar^2}{2m}\nabla^2\psi(\boldsymbol{r}) + U(\boldsymbol{r})\psi(\boldsymbol{r}) = E\psi(\boldsymbol{r}) \tag{2.24}$$

$$-\frac{\hbar^2}{2m}\nabla^2\psi(\boldsymbol{r}+\boldsymbol{T}) + U(\boldsymbol{r})\psi(\boldsymbol{r}+\boldsymbol{T}) = E\psi(\boldsymbol{r}+\boldsymbol{T}) \tag{2.25}$$

The wave states under periodic confinement $\psi(\boldsymbol{r})$ and $\psi(\boldsymbol{r}+\boldsymbol{T})$ must satisfy the same second-order differential equation. This means either $\psi(\boldsymbol{r})$ is periodic. The solution of equation (2.24) with a periodic potential takes the Bloch waveform:

$$\boldsymbol{\psi}(\boldsymbol{r}) = e^{i\boldsymbol{k_n}\cdot\boldsymbol{r}}u_{\boldsymbol{k}}(\boldsymbol{r}) \tag{2.26}$$

where $u_k(r)$ is periodic with the same periodicity of the crystal lattice.

The Bloch wave is the energy eigenstate for an electron in a crystal, and it takes the waveform describing a plane wave $e^{ik_n\cdot r}$modulated by a periodic potential $U(\boldsymbol{r})$. The "k" subscript means the function $u_k(\boldsymbol{r})$ is different for different wavenumbers, i.e. different crystal orientations. The waveform shows that the allowed states of the electron in the crystal is determined by $\boldsymbol{\psi}(\boldsymbol{r})$ which is a function of both k_r and $u_k(\boldsymbol{r})$, that is, one $\boldsymbol{\psi}(\boldsymbol{r})$ can be decomposed into many different sets of k_n and $u_i(\boldsymbol{r})$.

The same set of Bloch state $\boldsymbol{\psi}(\boldsymbol{r})$ can be written using (**k** + **K**), where **K** is $\boldsymbol{k_1} - \boldsymbol{k_2}$ and can be any reciprocal lattice vector. Periodicity of $u_k(r)$ in the Bloch function and of the phase coefficient in the plane wave $e^{ik_n\cdot r}$ with respect to k_n with period 2π gives rise to an important property that wavenumbers differing in integer number of K =

$2n\pi/a$ appear to be equivalent. This dispersion of energy and wavevectors represents that waves differing by a reciprocal lattice vector possess equivalent energy state and crystal momentum. For each band, we can define a function $\omega_n(k)$, which is the dispersion relation for electrons in that band. The dispersion curve of allowed energy levels in the crystal changes smoothly with k, but forms discontinuities only at points $k_n = \frac{n\pi}{a}$ (solid sinusoidal curves in Figure 2.10A). Figure 2.10A also presents the dispersion relation of a free electron (dashed curve) which follows the relation: $\omega_n(k) = \frac{\hbar k^2}{2m}$, thus the dispersion curve is continuous for every wavevector. These continuities of energy refer to all possible allowed momentums in the lattice that is the definition of the Brillouin zone. All possible Bloch states can be described without redundancy by defining in the first Brillouin zone every Bloch state has a unique k. Therefore, we can plot the dispersion relation in the first Brillouin zone (Figure 2.10B for free electrons; Figure 2.10C for Bloch waves) which is equivalent to the energy diagram in the extended zone in Figure 2.10A.

From Figure 2.10C at those discontinuous k_n points $\frac{\partial\omega}{\partial k} = v_g = 0$ where waves cannot propagate so that forming standing waves. The coexistence of two energy levels at discontinuous k_n refers two standing waves can possibly coexist with different potential energies. This leads to the emergence of forbidden energy intervals for which no propagating wave exists.

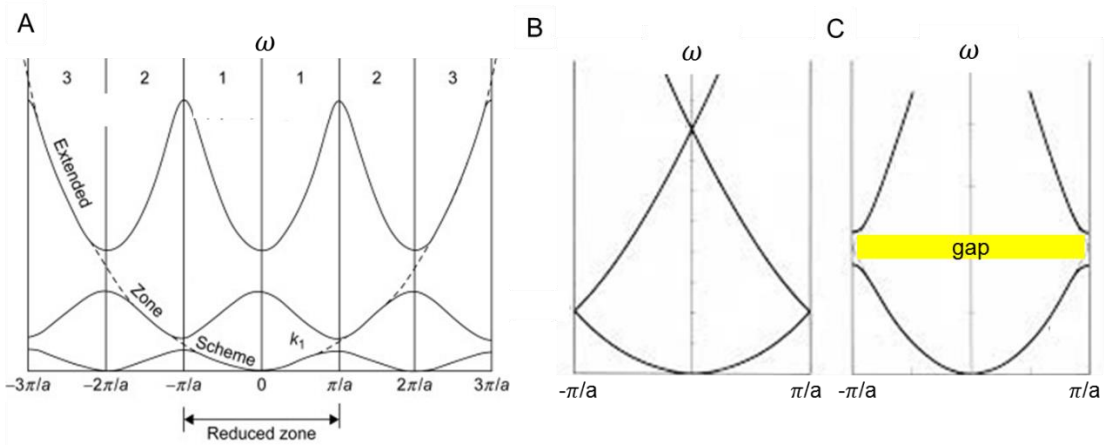

Figure 2.10 (A) Energy states of a free electron (dashed line) and an electron in a periodic media with a lattice constant a (solid lines). (B) Energy diagram of free electron and (C) Energy diagram of electrons confined in a crystal plotted in a reduced zone scheme (first Brillouin zone). Images are adapted from *Photonic Crystals: Molding the Flow of Light* [139].

2.4.3 One-dimensional photonic crystal

The concept of thin-film interference developed in the previous section can be extended to multilayers by calculating the reflection and transmission at each interface using the transfer matrices method [92,140] or numerical method [19].

We have shown examples of narrowband multilayers in different living organisms in section 1.2.1. For the former, the structure is usually constructed by periodic layers with just a few types of dielectric media with a uniform thickness of each layer, therefore only light with certain frequencies can be reflected and specific colours can be generated. The corresponding one-dimensional photonic crystal model is illustrated in Figure 2.11A, where the multilayer consists of infinitely extended stacks of alternating layers made from two dielectric materials with thicknesses a, b for materials with dielectric constants $\varepsilon_1, \varepsilon_2$, respectively. We define the unit cell length $p = a + b$ and

the dielectric constant of such multilayers can be written as $\varepsilon(x) = \varepsilon_1$ for $mp - \frac{a}{2} \leq x < mp + \frac{a}{2}$, and $\varepsilon(x) = \varepsilon_2$ for $\left(m + \frac{1}{2}\right)p - \frac{b}{2} \leq x < \left(m + \frac{1}{2}\right)p + \frac{b}{2}$ where m is positive integers. We use Fourier-expansion to express the infinite periodicity of the electron field and the inverse dielectric function in Bloch waveforms:

$$E(x) = \sum_{t=-\infty}^{\infty} \mathrm{E}_t \, e^{-i\frac{2\pi x}{p}t} \tag{2.27}$$

$$\frac{1}{\varepsilon(x)} = \sum_{s=-\infty}^{\infty} \varphi_s \, e^{-i\frac{2\pi x}{p}s} \tag{2.28}$$

where E_t and φ_s are the Fourier coefficients of the field $E(x)$ and the admittance $\frac{1}{\varepsilon(x)}$, respectively. Inserting the Fourier expansions in the wave equation (2.24), we derive the eigenequation:

$$\sum_{t=-\infty}^{\infty} \left(\frac{2\pi t}{p} + \mathrm{k}_x\right)^2 \varphi_{s-t} \mathrm{E}_t = \left(\frac{\omega}{c}\right)^2 \mathrm{E}_s \tag{2.29}$$

By defining an operator $\boldsymbol{O}_{s,t}$ which is a $2\mathrm{S}_{max} + 1$ by $2\mathrm{t}_{max} + 1$ matrix with every element in the matrix as $\left(\frac{2\pi t}{p} + \mathrm{k}_x\right)^2 \varphi_{s-t}$, we can express (2.29) as below:

$$\mathbf{O}_{s,t} \mathrm{E}_t = \left(\frac{\omega}{c}\right)^2 \mathrm{E}_s \tag{2.30}$$

Equation (2.30) reveals that this is an eigenvalue problem. The Fourier coefficients φ_{s-t} in the element of $\mathbf{O}_{s,t}$ can be found by using the inverse Fourier transform:

$$\varphi_{s-t} = \frac{1}{\varepsilon_2} \cdot \delta_{s-t} + \left(\frac{1}{\varepsilon_2} - \frac{1}{\varepsilon_1}\right) \cdot sinc\left(\frac{\pi(s-t)d_1}{p}\right) \tag{2.31}$$

By computation the matrix $\mathbf{O}_{s,t}$ its eigenvectors E_t and the corresponding eigenvalues $\left(\frac{\omega}{c}\right)^2$ can be derived which give the band diagram.

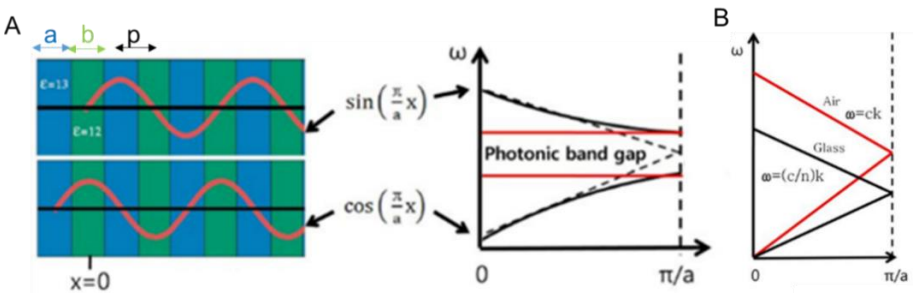

Figure 2.11 Band diagrams and field distributions of light propagating in (A) a 1D photonic crystal composed of two dielectric materials, or in (B) a homogeneous medium of air (black line) or glass (red line). A photonic bandgap is created in a 1D photonic crystal, but not in homogeneous media. The slope of the dispersion curve is the group velocity of the light. The slope decreases in the medium with a higher refractive index. Images are adapted from *Photonic Structures Inspired by Nature* with the author's permission [141].

Light propagates within the structure as a standing wave. The range of wavelengths not allowed to propagate in the structure is termed as the 'photonic band gap'. Comparing Figure 2.11A and B, we observe that when light propagating in a periodic structure, allowed modes are formed above the maximum and below the minimum frequency of the photonic bandgap. Light with wavelengths in the prohibited region (i.e. frequencies in the range of bandgap) cannot propagate in the structure, and it is therefore reflected from the crystal system to generate a coloured appearance (structural colour).

For these structural colours, the factors that open the bandgap are especially of interest. The width of the photonic bandgap ($\Delta\omega$) varies with factors such as lattice structures, the contrast of refractive indices and polarisation of the incident light. The extent of a photonic bandgap can be characterized by its frequency width. The gap–mid-gap ratio ($\frac{\Delta\omega}{\omega_m}$) is a useful characterization independent of the scale of the crystal. For this reason, the parameters of a band diagram are usually presented in dimensionless units such as frequency $\frac{\omega a}{2\pi c}$ and wave vector $\frac{ka}{2\pi}$.

The gap size of periodic systems can be deduced from well-developed perturbation theory for linear Hermitian eigenproblems. For detailed derivation, readers are referred to textbooks on quantum mechanics such as Sakurai (1994) [142]. By applying the perturbation procedure to the wave equation, we obtain a simple formula for the frequency shift $\Delta\omega$ that results from a small perturbation $\Delta\varepsilon$ of the dielectric function:

$$\Delta\omega = -\frac{\omega}{2}\frac{\int d^3\boldsymbol{r}\,\Delta\varepsilon(\boldsymbol{r})|\boldsymbol{E}(\boldsymbol{r})|^2}{\int d^3\boldsymbol{r}\,\varepsilon(\boldsymbol{r})|\boldsymbol{E}(\boldsymbol{r})|^2} + O(\Delta\varepsilon^2) \tag{2.32}$$

Equation (2.32) applies to general photonic crystals such as two- or three-dimensional crystals under the condition of small variations of dielectric media. It is worthwhile, however, to point out a few useful analytical results that are only possible for the special case of one-dimensional problems. For example, for a multilayer with either the dielectric contrast is weak ($\frac{\Delta\varepsilon}{\varepsilon} \ll 1$) or the thickness difference is small ($a \approx b$), then the equation (2.32) can be simplified:

$$\frac{\Delta\omega}{\omega_m} \approx \frac{\Delta\varepsilon}{\varepsilon} \cdot \frac{\sin(\pi d/a)}{\pi} \tag{2.33}$$

Although (2.33) is applied to the specific case, some useful properties can be summarized that (1) periodic dielectric media is required for open the gap (i.e. $d/a \neq 1$), (2) gap size is proportional to refractive index contrast ($\Delta\varepsilon$). Therefore, a photonic crystal with a higher refractive index contrast can generate a larger bandgap.

2.4.4 High-dimensional photonic crystals

For 2D and 3D photonic crystal structures, there may be many different directions or orientations within the structure that have associated periodicities [143]. The photonic bandgap may occur in each of the multiple directions of the structure that have a periodic nature. These periodic directions are dictated by the symmetry of the photonic

crystal, in particular the points of high-symmetry inherent in the geometry which we demonstrated in Figure 2.9 of the irreducible Brillouin zone. The photonic band-gap along each direction of high symmetry can be represented in the band diagram. In these directions, effective periodic geometric planes give rise to photonic bandgaps.

3D photonic crystals possess periodicity in three dimensions. Many lattices and theoretical investigations have been reported for close-packed dielectric spheres, as well as their inverted lattices. Analysis of various 3D lattices revealed the features of band-gap formation for the same lattice structure (simple cubic, face-centred cubic, and body-centred cubic lattices were examined). The structures comprising a continuous topology of high-ε and a small volume fraction of about 0.2–0.3 of the dielectric in the air appear to be more advantageous for producing large gaps. Several 3D crystals possess a complete band-gap: a diamond lattice of air holes, a Yablonovite structure, a woodpile stack of orthogonal dielectric columns, an inverse opal, and a stack of alternating two-dimensional crystals of rods and holes. Among the variety of cubic lattices, the diamond lattice features the widest complete band-gap (Figure 2.12). The diamond structure is a type of face-centred cubic lattice, so it shares the same high symmetry lines and points of the FCC system (see Figure 2.9). For the diamond lattice consisting of close-packed dielectric spherical particles, the band-gap was found to open for all directions when the refractive index contrast $n_{diel}/n_{air} > 2$.

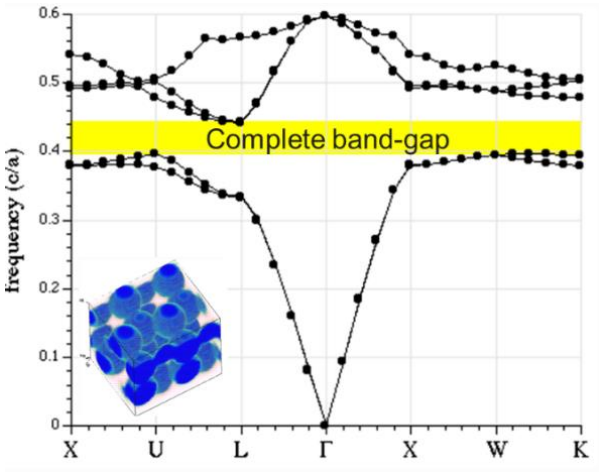

Figure 2.12 The photonic band diagram of a diamond structure made of dielectric spheres (ε =11.56; radius: lattice constant= 0.25) in air. The complete band-gap is shaded with yellow colour. This image is adapted from the open-source software *MIT Photonic Bands* (https://mpb.readthedocs.io/en/latest/).

2.5 Mechanical properties of structural materials

2.5.1 Elasticity

The deformation of a material is fundamentally related to the applied stress and strain. There are six components of stress (three normal stresses and three shear stresses) and six components of strain at any point in a material (Figure 2.13A). In structural analysis, the constitutive equation the describes the connection between applied stress to strain for a material for linear elasticity is:

$$\boldsymbol{\sigma}_{ij} = \boldsymbol{C}_{ijkl}\varepsilon_{kl} \tag{2.34}$$

C_{ijkl} is the fourth-order elasticity tensor that contains the material properties and is in general composed of 21 independent parameters. However, in the case of isotropic linear elasticity, only two independent parameters remain, so the elasticity tensor is reduced as:

$$\boldsymbol{C}_{ijkl} = \lambda\delta_{ij}\delta_{kl} + \mu(\delta_{ik}\delta_{jl} + \delta_{il}\delta_{jk}) \tag{2.35}$$

The material coefficients λ and μ are known as the Lamé parameters. Using this equation, the stress-strain relationship is:

$$\boldsymbol{\sigma}_{ij} = \lambda\varepsilon_{kk}\delta_{ij} + 2\mu\boldsymbol{\varepsilon}_{ij} \tag{2.36}$$

If an isotropic material is under uniaxial stress, the stress tensor $\boldsymbol{\sigma}$ is reduced to:

$$\boldsymbol{\sigma} = E\boldsymbol{\epsilon} \tag{2.37}$$

Where E is Young's modulus and $\boldsymbol{\epsilon}$ is the strain.

Figure 2.13B shows when a uniaxial tensile strain is applied to material along ϵ_{22} direction, it contracts perpendicularly on ϵ_{11}direction. This behaviour can be described by the Poisson's ratio v:

$$v = -\frac{\epsilon_{22}}{\epsilon_{11}} \tag{2.38}$$

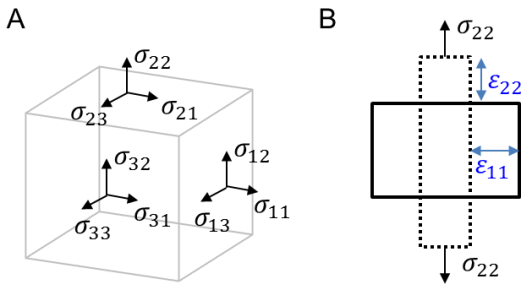

Figure 2.13 Stress and strain tensors for describing elastic deformation. (A) Components of stress tensors in three dimensions. (B) Two-dimensional elastic deformation of an element under uniaxial stress. The solid square is the element before deformation, and the dashed rectangle is the element under uniaxial stress. The element contracts perpendicularly on ϵ_{11}direction, which can be described by Poisson's ratio.

For isotropic materials, the Poisson's ratio is possible between -1 to 0.5, and most materials have the Poisson's ratio between 0.3 and 0.5. A perfectly incompressible material under elastic deformation is with Poisson's ratio of 0.5. Rubber has a Poisson's

ratio of about 0.5. Most rigid polymers exhibit Poisson's ratio of about 0.3 before yield, and 0.5 for post-yield deformation. Tissues are assumed with the Poisson's ratio about 0.3 to 0.5, and studies show the estimation error of the Poisson's ratio of different tissues is small ~3% [144].

Young's modulus (E) and Poisson's ratio (ν) are two invariants to describe all possible stress and strain relationships of any linearly elastic material. Many other elastic constants such as the shear modulus G or the bulk modulus K are developed to feature material properties in different conditions while they can all be described by E and ν and relate to the Lamé parameters of materials. The relationships of the elastic parameters and Lamé parameters are shown in Table 2.1. Materials with Poisson's ratio of about 0.5 are incompressible and the bulk modulus approaches infinity.

Table 2.1 Relationships of elastic constants with Young's modulus E, Poisson's ratio ν and with the Lamé parameters λ and μ of materials.

	E, ν	λ, μ	K, G
E, ν		$E = \frac{\mu}{\lambda+\mu}(2\mu+3\lambda)$ $\nu = \frac{\lambda}{2(\lambda+\mu)}$	$E = \frac{9KG}{3K+G}$ $\nu = \frac{3K-2G}{6K+2G}$
λ, μ	$\lambda = \frac{\nu E}{(1+\nu)(1-2\nu)}$ $\mu = \frac{E}{2(1+\nu)}$		$\lambda = K - \frac{2}{3}G$ $\mu = G$
K, G	$K = \frac{E}{3(1-2\nu)}$ $G = \frac{E}{2(1+\nu)}$	$K = \lambda + \frac{2}{3}\mu$ $G = \mu$	

The stress can be derived from the strain-energy function W that $\sigma = \frac{\partial W}{\partial \varepsilon}$. The strain-energy is a function of strain and the elasticity tensor:

$$W = \frac{1}{2}\boldsymbol{\varepsilon}:\boldsymbol{C}:\boldsymbol{\varepsilon} \tag{2.39}$$

And for isotropic materials, the strain energy function is:

$$W = \frac{1}{2}\lambda(tr\boldsymbol{\varepsilon})^2 + \mu\boldsymbol{\varepsilon}:\boldsymbol{\varepsilon} \tag{2.40}$$

The Cauchy stress vector $\boldsymbol{\sigma}$ is therefore given as:

$$\boldsymbol{\sigma} = \lambda(tr\boldsymbol{\varepsilon})I + 2\mu\boldsymbol{\varepsilon} \tag{2.41}$$

where $\boldsymbol{I}$ is the square of the material stretch gradient $\boldsymbol{F} = \frac{\partial \boldsymbol{\varphi}}{\partial \boldsymbol{X}}$

2.5.2 Contact mechanics

Indentation tests using atomic force microscopes (AFM), nano-indenters or micro-indenters become popular methods for extracting local mechanical properties of biological materials. The small ratio of testing volume benefits the measurements of local properties of heterogeneous materials at different hierarchy levels. These techniques have been applied to nano-mechanics and nano-imaging. This local property is essentially important to be characterized by the heterogeneity of natural materials. Through characterizations at different length scales, the conformation and integrity of structures in biological materials can be understood.

In AFM, the tip slightly contacts or taps on the sample surface, or in a noncontact mode away from the surface while maintaining the potential force with surface atoms. AFM is therefore used for characterizing surface properties including mechanical responses or surface imaging. On the other hand, in indentation testing, a probe is pressed into a

material under load-control or displacement-control, and the load and displacement are monitored during the contact cycle. In this mode, the tip detects the mechanical responses from the whole testing volume which is usually ten times larger than the indentation depth.

Unlike compression or tension tests, the load-displacement relationships measured during indentation tests cannot be directly related to stress-strain relationships because the deformation experienced by the material is not uniform. However, there are a variety of numerical models that can be fitted to the load-displacement data in different indentation designs to extract relevant material properties [145,146]. Although the indentation method is more complicated to analyse then compression or tension results, it is used frequently throughout studies on biological materials because of the least requirement for sample size and geometry.

Oliver and Pharr in 1992 published a mechanism for the deconvolution of reduced modulus E_R and hardness H of an elastic-plastic half-space based on the indentation load-displacement curve [145]. The reduced modulus E_R represents the elastic deformation that occurs in both sample and indenter tip. The elastic modulus indicates the stiffness of the testing materials before any permanent deformation. Hardness is a measurement of the maximum strength the testing material can bear with the applied load. For metals or ceramics which are nearly pure elastic or pure plastic materials, the elastic modulus and hardness are two independent parameters that reflect the local resistance to reversible and irreversible deformation, respectively.

Due to the hierarchical and heterogeneous organizations, the mechanical responses of biomaterials vary with different length scales depending on observations. Nanoindentation is therefore an ideal technique to measure the local properties and map

the heterogeneity of biomaterials [147]. However, biological materials do not behave as typical elastic-plastic models which arises challenges in interpreting the nanoindentation data with the Oliver-Pharr method. It is difficult to separate each mechanical parameter. The elastic modulus is still a good indication of the resistance to reversible deformations in biological materials, whereas the hardness from an instrumented nanoindentation test is actually a measure of the total resistance to deformations, regardless the deformation is elastic, plastic, viscous, fracture, and more possibly a combination of the above [147–149]. Labonte et al. comparing a wide range of nanoindentation data of biomaterials found a linear relationship between elastic moduli and hardness of biomaterials. They reported the hardness is a hybrid property dependent on the elastic modulus because of the competitive quasi-plasticity and brittle fractures in biomaterials [149].

2.5.3 Sharp indentation

Most commonly used indenters are sharp indenter tips—either a cone (Cube-corner tip) or a three-sided pyramid (Berkovich tip) with a tip front radius of 50–100 nm. The sharp indentation introduces large plastic deformation in the materials at every indentation depth, and benefit from a deep indentation test (few μm) into materials.

Oliver-Pharr method is always applied to analyse the unloading curve by assuming the material performs purely elastic deformation when unloading. The Belehradek power-law function was used to fit the unloading force-displacement data and the full elastic solution for conical indentation is:

$$P = \frac{\pi \tan \psi}{2r^2} \frac{E}{1-\nu^2} h^2 \tag{2.52}$$

where P is the applied load, h is the indent depth, for a conical indenter with included half-angle ψ (65.27 º for Berkovich tip) and γ = π/2.

Typically, the testing volume is ten times larger than the indent depth, so for sharp tips, the indent depth is usually larger than 100 nm. That is, the testing materials have to be thicker than 100 nm. A sharp indentation on pure elastic, pure plastic and elastic-plastic materials generates different stress-strain responses and indentation patterns.

The sharp tips cause immediate plastic deformation in the samples, the elastic-plastic deformation can occur during the whole indentation profile. The large strains in the material below the point result in a near-immediate onset of plasticity and a dominantly plastic overall response. The functional for elastic-plastic deformation under conical or pyramidal loading is still with a similar form of equation (2.52) that $P \propto h^2$.

The deconvolution of elastic and plastic deformations in the Oliver-Pharr method is based on the assumption that the unloading response is purely elastic such that the reduced modulus E_R of the contact can be related to the unloading stiffness S:

$$\frac{1}{E_R} = \frac{1-v_{sample}^2}{E_{sample}} + \frac{1-v_{indenter}^2}{E_{indenter}} \tag{2.53}$$

$$S = \frac{dP}{dh}|_{P_{max}} \tag{2.54}$$

$$E_R = \beta(1 - v_{sample}^2)\frac{S\sqrt{\pi}}{2\sqrt{A_c}} \tag{2.55}$$

$$H = \frac{P_{max}}{A_c} \tag{2.56}$$

where v_i: the Poisson's ratio of indenter or sample; E_i: the elastic modulus for each body; β: a dimensionless parameter that varies with indenter shape (1.0226<β<1.085) [145], 1.034 was used for the Berkovich tip; A_c: the contact area at contact depth h_c

The contact area (A_c) in equation (2.55) and (2.56) is the projected area calculated from the contact displacement (h_c) *via* a calibration function. The contact area takes the read:

$$A_c = \pi \tan^2 \psi \, h_c^2 + 4R\pi h_c + 4R^2 \pi \cot^2 \psi \tag{2.57}$$

R is the effective tip radius from the harmonic average of spherical and conical shape; ψ is the cone angle. Equation (2.57) does not work at small indentation depths as the pyramid tip cannot be made perfectly sharp. In practice, the tip is approximated as a sphere at shallow contact depth, it is usually a numerical solution derived from a series indent depth calibration with a specific tip. The relationship between the contact depth and the contact area is often taken as a summed polynomial of the form:

$$A_c = C_0 h_c^2 + \sum_{k=1} C_k \sqrt{h_c}^{k-1} \tag{2.58}$$

in which the coefficients C_i are determined by calibration. The contact depth (h_c) is a function of the geometry of the tip, the unloading stiffness, and the indent depth which can be calculated through this half-experimental equation:

$$h_c = h_{max} - \varepsilon \frac{P_{max}}{S} \tag{2.59}$$

ε is the geometry factor of the tip (for Berkovich tip $\varepsilon = 0.75$). The calibration is always performed before any indentation testing on samples. By indenting on a standard sample with known E_R such as a fused silica (E_R = 69.6 GPa), from equation (2.55) A_c can be derived by fitting the S at different indent depths, and h_c can be calculated by equation (2.59). The polynomial equation (2.58) is built in the commercial indentation instruments which are later used to calculate H_A and E_R of targeted materials.

2.5.4 Spherical indentation

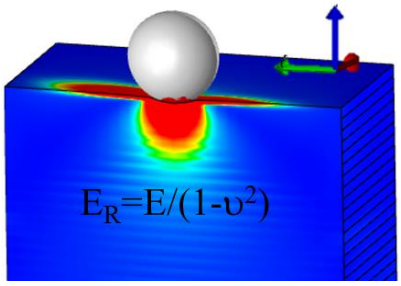

Figure 2.14 Schematic diagram of spherical indentation of a bulk half-space showing the non-uniform stress distribution in the layered material.

The spherical indentation is suitable for probing the elastic properties and the elastic-to-plastic transition of materials with a shallow indentation depth. To extract the essential material parameters such as reduced modulus E_R from the non-uniform stress-strain distribution (Figure 2.14), the most well-known analytical model is the elastic Hertz solution [146]. According to the Hertz solution, if the modulus of the indenter tip is much greater than the modulus of the material, the indenter load and displacement are related as such:

$$P = \frac{4E_R h\sqrt{Rh}}{3} \tag{2.60}$$

where R is the radius of the spherical tip [146] and E_R is related to the Young's modulus:

$$E_R = \frac{E}{1-\nu_{sample}^2} \tag{2.61}$$

From the diagram Figure 2.14, we can observe the size of the stress and strain fields is a function of the contact radius between the sphere and half-space a [150]:

$$a = \sqrt{Rh} \tag{2.62}$$

The magnitude of the stress and strain is a function of the ratio of contact radius to the indenter radius and the sample reduced modulus E_R. The magnitude of stress and strain

gets progressively smaller as the distance from the contact region increases [151] proposed that a representative indentation strain:

$$\varepsilon \approx \frac{0.2a}{R} \tag{2.63}$$

Experimental [151,152] and computational studies [153] proved this representative strain works well on the estimation of the strain field of materials with shallow indents.

The Hertz model provides a simple algebraic form for calculation which are however based on many assumptions. As an example, the Hertz model assumes that contact between the indenter and half-space is frictionless with no adhesion. Solutions of spherical indentation with finite friction reveal that the total load needed to produce a contact radius of a given size can only be a maximum of 5% larger than that predicted by the Hertz solution [146]. The model uses a paraboloid to approximate the spherical contact which works better when the indentation strain is less than 0.05.

In real experimental conditions, these assumptions might be not fully satisfied and therefore the experimental observations might result in huge deviations from the model and cause an error in the interpretation of the results.

Chapter 3.

Experimental materials and methods

This chapter introduces the sample preparations, equipment set-up, techniques, and methodologies for characterizing and analysing optical properties, mechanical properties, and microstructures of biological samples. I introduced the techniques of optical microscopy, optical spectroscopy, nanoindentation, scanning electron microscopy, transmission electron microscopy, atomic force microscopy infrared. Numerical modelling and molecular simulation setup and analysis methods are presented. Finally, statistical analyses and data extraction methods are given here. Later chapters include short experimental sections and outline additional techniques and specific setups.

3.1 Optical property characterisations

3.1.1 Optical microscopy

A customised microscope was used for the micro-spectroscopy in the following chapters. The microscope was configured for Koehler illumination which is a process that provides optimum contrast and resolution by the well-aligned light path and uniform illumination over the field of view. Figure 3.1 illustrates the setup. All the components were aligned on the optical axis of the microscope objective. For reflection measurements, the microscope was illuminated with a halogen lamp (Hal 100), passing through the numerical aperture. All optical images were captured by the CCD (Thorlabs DCC3240C or IDS UI-3580LE-C-HQ). The CCD was accessed by Thor-Cam/ uEye Cockpit user interface software.

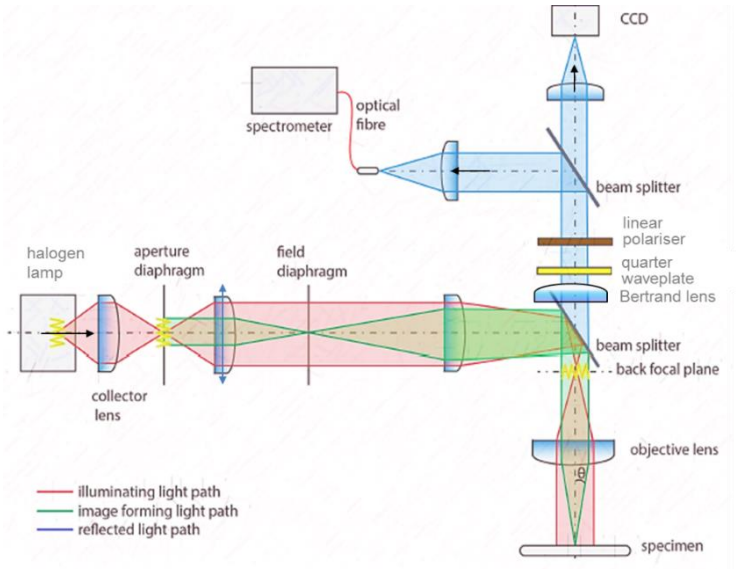

Figure 3.1 Schematic of the customized microscope with a Koehler illumination set-up. This diagram shows a reflected bright field configuration. The illuminating light path (red), the image forming light path (green) and the reflected light path (blue) are illustrated. This image is adapted from *Cellulose photonics: designing functionality and optical appearance of natural materials* [154] with the author's permission.

In Koehler illumination the lamp and the specimen were in inverse focal planes, avoiding the overlaying of the image of the lamp and the image of the specimen. The red, green, and blue lines in Figure 3.1 indicate the light path of illuminating light rays, the image-forming light path, and reflected light rays. The black arrows indicate the direction of light propagation. Light propagates from the halogen lamp down onto the specimen, is reflected and passes through to the spectrometer and CCD camera. The objective lenses used were Zeiss EC Epiplan Apochromat for 5x, 20x, 50x, 100x magnification, having numerical apertures (NA) of 0.13, 0.6, 0.95, 0.95 respectively, or alternatively super long working distance objective lenses of Nikon, T Plan SLWD for 20x, 50x magnification with NA of 0.3, 0.45 and a working distance of 30 mm, 13.5 mm, respectively. In the case of bright field measurements, the numerical aperture was narrow down by closing up the aperture diaphragm to allow the light path of only approximately $\pm 5^{o}$ angular variation from the optical axis.

3.1.2 Darkfield microscopy

In Darkfield microscopy, it is possible to illuminate the sample for shallow direction (at a large angle of incidence), while the light scattered by the sample is collected in the NA cone of the objective. In this configuration, the numerical and field of view diaphragms were both maximally dilated unless otherwise stated. In the cases in our study, the incident light was at about 37^{o} for collecting off-axis light scattered from structures. In the case of darkfield measurement, the aperture diaphragm was opened up to allow the detection of scattering signals.

3.1.3 Spectroscopy

Spectra were recorded by coupling the microscope and a spectrometer (Avantes AvaSpec-HS2048) with the optical fibre (Avantes 50, 200, 600 um internal diameter)

as the set-up illustrated in Figure 3.1. Customised MATLAB code was used for visualizing live images of detected spectra, recording background signals, and subtracting spectra with background and normalising with respect to full intensity reflection from a silver mirror (Thorlabs, PF10-03-P01 25.4 mm) or a white standard diffuser (Labsphere USRS-99-010). The integration time was chosen to ensure a high enough intensity of spectra can be recorded. The data are smoothed using a moving average filter of 30 points to reduce noises and speckles. The Gaussian fit was applied to analyse the wavelength peaks, full width at half maximum (FWHM), and intensity.

3.1.4 Polarisation imaging

The microscope was coupled with a quarter-wave retardation plate followed by a linear polarizer in the reflected light path. This setup enables only left or only right circularly polarised light to be transmitted to the CCD, so it allows us to analyse the optical response of chiral samples. The relative direction of the quarter-wave plate (Thorlabs 25 mm) with respect to the linear polarizer is controlled by motorised controllers (Thorlabs, TDC001) actioned by an APT controller configured using a customised MATLAB interface. If an unpolarized natural light impinges on an ideal linear polarizer, only ***Ep*** will be transmitted because it has an orientation parallel to the transmission axis of the polarizer. This polarized light will then pass through a second ideal linear polarizer (analyser) whose transmission axis is with a rotating angle of θ to the first polarizer. Suppose the amplitude of the electric field transmitted by the first polarizer is E_{01}, the intensity of the light reaching the detector can be calculated through Malus's Law:

$$I(\theta) = \frac{c\varepsilon_0}{2} {E_{01}}^2 \cos^2\theta = I(0)\cos^2\theta$$

3.2 Electron microscopy

3.2.1 EM sample preparations

Ambient dried samples were taken through graded ethanol and LR White resin series prior to embedding. Samples were immersed in 100% LR White hard resin (Agar Scientific, UK) for 24 hours and then hardened by heating at 60 °C overnight. After resin embedding, the embedded blocks were transversely cut with a 35° diamond knife (Diatom, USA) equipped on an ultramicrotome Leica EM UC6 (Leica Microsystems, Germany). Microtome slices with a thickness of 100-300 nm were produced. The surface of the embedded block was polished while microtoming with the sharp diamond knife, and the roughness is less than 300 nm. The blocks were used for SEM imaging.

3.2.2 Scanning Electron Microscopy (SEM)

The SEM (Tescan MIRA3 FEG-SEM) was used for anatomical investigation. Before imaging, the sample was mounted on a metal SEM sample stub by a double-sided carbon tape or conductive copper tape. The stub and the mounted samples were then plasma coated with a 10 nm thick Pt layer to make the specimen conductive and avoid electron charging. The sample was imaged in a low vacuum chamber at 3-5 kV and an in-beam secondary electron detector is used for imaging.

3.2.3 Transmission Electron Microscopy (TEM)

Samples were firstly fixed in 3% phosphate-buffered glutaraldehyde followed by 1% osmium tetroxide for enhancing the image contrast of different components. Thin microtome sections were with the thickness of 100 nm and transferred onto Cu grids (Agar Scientific Ltd, Stansted, U.K.) and stained (uranyl acetate and lead citrate) followed by 10 nm carbon coating and 1 minute plasma cleaning before being imaged

in TEM (Hitachi H-7650 / AMT XR41 digital camera or AMT 2k x 2k digital camera). The TEM was operated at 80 kV.

3.3 Optical simulations

Modelling the interactions of light with optical structures enables us to configure the states of electric fields propagating in the probed photonic system. Analyses of the configuration of the electric field also enable us to calculate its transmission/reflection response, band diagrams, and spectra. The theoretical modelling performed and presented in this thesis includes the MIT Photonic-Bands package (MPB, http://ab-initio.mit.edu/mpb) which is a freely available software for computing definite-frequency eigenstates of Maxwell's equations in periodic dielectric structures. In addition, Finite-Difference Time-Domain (FDTD) calculation using the commercially available software Lumerical (Lumerical Solutions Ltd.) for which modelling processes were performed in the time domain and provided numerical results.

3.3.1 MIT Photonic-Bands package

MIT Photonic-Bands package (MPB, http://ab-initio.mit.edu/mpb) is an open-source program designed to solve Maxwell's equations for plane waves propagating in photonic crystals [155,156]. It computes definite-frequency eigenstates (harmonic modes) of Maxwell's equations in periodic dielectric structures.

Because MPB does a direct computation of the specific eigenstates and eigenvalues of Maxwell's equations which are advantageous in calculating band structures and eigenstates. It uses iterative methods, that is, the operator is only applied to individual vectors and is never itself computed explicitly which are practical for calculating the huge size of the matrix. There are many advantages to calculate in the frequency domain,

for example, it can calculate all possible states and the error in the frequency decays exponentially with the number of iterations. Moreover, the time needed to calculate in frequency-domain is always less than in time-domain. A typical disadvantage of frequency-domain methods is that all eigenstates lower than the targeted ones have to be computed.

In this thesis, MPB modelling was used in conjunction with experimentally measured optical spectra and geometric analyses in order to identify the origins of the intense colours produced from photonic crystal structures. A series of calculations are made to resolve the band structures associated with a series of 3D photonic crystal lattices with varied lattice constants and filling fractions.

3.3.2 Finite-Difference Time-Domain simulation

Finite-difference time-domain (FDTD) is a numerical calculation for modelling electrodynamics. This numerical analysis provides approximate solutions to the associated system of Maxwell's differential equations [157]. Finite time-domain refers that FDTD is based on a time-domain eigensolver (discretise simulation time into constant time steps) [158], so the solutions can cover a wide frequency range with a single simulation run (depend on the simulation software, typically for micron-sized samples with incident light wavelengths < 1 μm) [159].

A finite difference method indicates a grid-based differential numerical modelling method. It involves subdividing the probed model geometry into many finite elements (mesh). The shape and numbers of elements can be adjusted based on the shape of the model or simulation dimensions. For example, here I used Lumerical, a commercial software, to generate square grids in two-dimensional simulations and cube grids in three-dimensional simulations (Figure 3.2). Time-dependent Maxwell's equations in

the partial differential forms are discretized using central-difference approximations to space (each grid size) and time (every time step) partial derivatives. The electric field vector components (TM) in a volume of space are solved at a given instant in time, and the magnetic field vector components (TE) in the same spatial volume are solved at the next instant in time. This process iterates until the steady-state of the electromagnetic field is achieved.

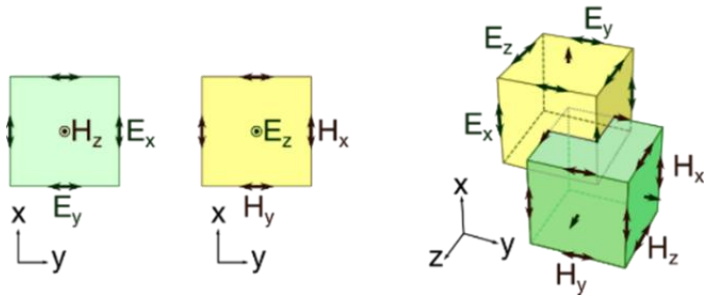

Figure 3.2 Illustration of a standard cartesian cell used for FDTD (Yee grid in 3D space, images cited from *Numerical solution of initial boundary value problems involving Maxwell's equations in isotropic media* [157]). In 3D space, the electric field components (E_x, E_y, E_z) form the edges of the cube, and the magnetic field components (H_x, H_y, H_z) form the normal to the faces of the cube. An electromagnetic wave interaction structure is mapped into the space lattice by assigning permittivity to each electric field component, and permeability to each magnetic field component.

The FDTD method can compute transmission/ reflection spectra, field patterns, resonant modes, frequencies in dielectric structures, and so on. Since operating in the time domain, FDTD is intuitive for users to set up simulation conditions and interpret the results. Also, versatile light sources such as a broadband pulse (e.g. a Gaussian pulse) with customized numerical aperture can be used, and both linear and nonlinear dielectric and magnetic materials can be modelled.

To resolve the open-region (edges and planes of the models), the perfectly matched layer (PML) formulation is one of the commonly used grid truncation techniques [160–

[162]. PML is an artificial absorbing region to absorb evanescent waves at boundaries. It is designed to artificially reduce undesired numerical reflection back from the open boundaries. This type of boundary is normally placed at a distance greater than away from the structure in order to ensure no near-field interference occurs. With the case of periodic, ordered photonic crystal structures, it is possible to construct a small unit cell of the structure and set up periodic boundary conditions at the repeated dimensions.

The grid spatial discretization directly links to the precision of the distribution of permittivity and permeability in space so that solutions of electromagnetic fields in space. That is, grids must be sufficiently fine to describe smallest the smallest geometrical feature of the model and resolve the smallest electromagnetic wavelength which results in very large computational memory and long solution times.

In this thesis, FDTD calculation was used to discuss how the domain sizes, filling fraction, and the curvature of connections of lattice sites affect the optical properties.

3.4 Nanoindentation

Nanoindentation-based studies are useful to examine local variations in mechanical behaviours. Even though the indentation depth is within a few nanometres, the indentation testing volumes are in micrometres in three dimensions. The testing volume differs with testing materials and can be relatively large when probing porous, plastic, and composite materials which are prone to compaction, cracking and chipping.

The instrumented nanoindenter can be equipped with a standard Berkovich tip. Commercial nanoindenters can be operated in a force control mode, a displacement control mode, or an indentation control mode. The Berkovich tip is a four-sided pyramid with a tip angle of 142.3^{o} and a half angle of 65.27 ^{o} which causes a very flat

indentation profile. This design enables the Berkovich tip to measure bulk materials and films greater than 100 nanometres thick. This design effectively decreases permanent densification and severe cracking.

3.5 Atomic force microscopy-based infrared spectroscopy

Atomic force microscopy-based infrared spectroscopy (AFM-IR) is a surface analysis technique that allows collecting IR spectra from a sample with high spatial resolution. An IR laser (1024-1800 cm^{-1}) illuminates the sample and an AFM tip locally detect the thermal expansion resulting from absorption of the infrared radiation.

Local IR spectra were recorded in contact mode on the sample surface using an Anasys NanoIR2 instrument equipped with a MIRcat Laser system (Daylight Solutions) containing four quantum cascade lasers (QCLs). The AFM cantilever-tip assemblies used were gold-coated with a 30 nm tip radius, spring constant 0.07–0.4 nm–1 and resonant frequency 13 ± 4 kHz (Anasys Instruments). IR analysis was done in resonant-enhanced mode (using an 8% duty cycle) with mapping tracking the contact resonance with a phase-locked loop. Laser scanning wavenumbers were set in the spectral range of 1450–1800 cm^{-1}. AFM-IR spectra were recorded under a reduced-humidity (dry N2) environment to minimize the IR noise from water vapour. The resulting background-subtracted spectra are smoothed using a second-order Savitzky–Golay algorithm. Spectra at each featured region in one sample was detected across at least twenty different locations. The averaged detected voltage of signals can differ by spectra, we normalized every curve based on the peak value at 1650 cm^{-1}. The presented spectra and analysis are from representative samples.

Chapter 4
The origin of chirality reversal in fruits of *Pollia condensata*

Naturally occurring helicoids in structurally coloured plants composed of cellulose mainly display left-handedness. Interestingly, the only reported exception is the cell wall of *Pollia condensata* fruit that cellulose helicoids with both left- and right-handednesses are observed in *Pollia condensata* fruit. The fruit has epicarpal cells with left- and right-handed helicoids in neighbouring cells within the same tissues. It is therefore interesting to investigate how the chirality is transferred from molecules to microstructures and the molecular origin of chiral asymmetry. In this chapter, we simultaneously analysed the optical and mechanical responses performed by cells with different handedness and pitch lengths. Results show cells with different handedness of the helicoidal cell walls have different mechanical performances and distribute differently on the epicarp. This discovery indicates handedness inversion might result from the compositional differences and relate to the development of plants.

The contents of this chapter have been submitted to *PNAS* and the paper is currently in progress. I acknowledge Dr. Rox Middleton for anatomizing fruits and measuring optical properties, Dr. Tom Gregory and Dr. Paula J. Rudall for preparing samples for TEM imaging.

4.1 Introduction

Helicoidal architectures are widespread in nature. This occurs every adjacent layer of cellulose microfibrils twisting with a small angle either in a counter-clockwise direction (left-handedness) or a clockwise direction (right-handedness). Several species adopt this structure to produce brilliant colourations [163–166] such as cellulose helicoids in plant tissues from ferns [163,164], to monocots [66,167,168], and eudicots [169] as well as the chitinous helicoids in the exocuticle of insects [25,170,171].

Scientists have been fantasizing about the biological functions of such structural colours on those different tissues of plants and insects for years. The biological significance of helicoidal architectures in plants is mainly suggested on enhancing the mechanical properties of cell walls. The robust cell walls might support the cell growth [24,25,34,125,172,173] or protect soft tissues inward the epicarp [25,124,174]. While the circularly polarized light generated by such structures is unique in nature, the functions of such optical properties in plants are unknown. First, as far as our understanding no terrestrial animals can detect circularly polarised light [175–177]. Second, cellulose helicoids in plant tissues are possible to generate reflecting light from ultraviolet to the infrared region of spectra [25,27,178,179], and why plants create such diverse structural colourations of different tissues remain unknown.

On the other hand, helicoidal structures are relatively rare in the animal kingdom comparing to the plant kingdom. Such structures are only found in wing veins of the damselflies [180], in elytra of some scarab beetles in the Rutelinae, Scarabaeinae and Cetoniinae subfamilies [136], and in exoskeletons of crustaceans such as crabs and stomatopods [126,133]. Again, due to the lack of evidence on terrestrial animals' vision for

sensing circularly polarised light, why some specific scarab beetles developed such helicoidal structures is unknown. In contrast, the circularly polarized light serves as a potentially covert communication channel for the stomatopod crustacean [132,133]. The designs of large pitches, as well as the helicoidal structures of crustaceans' exoskeleton, serve as mate signalling for the intended species while crypsis for the predators [133,181]. Crustaceans generate red-shifted or infrared signals from their helicoidally structured exoskeletons due to the large pitches at the micrometre length scale. This makes them transparent to most arthropods due to the lack of photoreceptors for red-shifted colours [124,126,132,174]. Gagnon et al. through behaviour studies demonstrate that circularly polarized body patterns of mantis shrimps make them conspicuous to each other while transparent to potential predators [133].

The morphogenesis of helicoidal structures in nature is complicated and is very specific to different biological tissues. Several mechanisms have been proposed for forming the oriented microfibrils in helicoidal cell walls, via biological control [29,30], physical forces [24,31], and the use of hemicellulose to guide the cellulose orientation [32–35]. Pioneering work by Reyes et al. [36] has suggested the importance of hemicellulose in driving helicoidal architectures of cellulose in quince mucilage.

Although constraints have been found on models of cell wall growth [168], the factors responsible for the control of handedness are under debate. One of the hypotheses is that the chirality of the helicoids has the same chirality as the composed biopolymers [127,182–187]. This assumption arises because in nature helicoidal structures with left-handed chirality seem to predominate across taxa [21,25,31,187,188], also most polysaccharides biopolymers were found with chirality of left-handedness. However, there is no evidence showing how the chirality transfers from molecular length-scale to

micrometre length-scale, and how certain handedness of the helicoidal structures is formed.

The fruit of *Pollia condensata* is the only exception in plants that left- and right-handed helicoidal architectures are observed in the neighbouring cells of the same tissue [66]. I tried to understand how reversal chirality is regulated in the helicoidal plant cell walls of *P. condensata*. Being inspired by pioneer studies, I hypothesized the opposite orientations of cellulose microfibrils in *P. condensata* are possibly controlled by growth force or regulated by hemicellulose. The former should show no difference in mechanical responses in terms of handedness. The latter, however, can result from (i) different densities of hemicellulose in the helicoids with opposite handedness, or (ii) different interaction forces between hemicellulose and cellulose microfibrils. Both (i) and (ii) will show differences in local mechanical responses. The identification of the polysaccharides in the cell wall on a single cell level of *P. condensata* is impossible because cells with opposite handedness are not possible to be manually separated and extracted one cell by one cell from the epicarp of the fruits. I decided to apply nanoindentation tests, which can detect local mechanical responses of every individual cell without separating them from the epicarp.

4.2 Materials and methods

4.2.1 Sample preparation for nanoindentation

P. condensata fruits were grown in the Optics lab in the Department of Chemistry. Mature and fresh *P. condensata* fruits were collected and fractured into small fragments (<1x1 mm^2) before indentation tests. The freshly broken fragments were then carefully

fixed on a magnetic disk with only the inner membrane of epicarp superglued on the magnetic disk. Once the outer surface of the epicarp was covered by the superglue due to the diffusion of the liquid, the sample was disposed. After fixing the fragment on a magnetic disk and drying of superglues, the thick cuticle (~3.5 μm) on the outermost layer of *P.condensata* was firstly scraped off by sandpapers followed by surface polishing with a 0.3 μm optical paper before indentation. The removal of the cuticle was carried out and inspected under a stereomicroscope (Leica M205 A). The surface roughness was examined using a fast 3D scanning stereo-microscope (Keyence VR 3100). This enabled us to directly indent on cellulose cell walls and reduce the effects of surface roughness on the nanoindentation results.

4.2.2 Nanoindentation and continuous stiffness measurement

The nanoindenter (Nano Indenter SA2, MTS Nano Instruments, Oak Ridge, TN, USA) equipped with a standard Berkovich tip was operated in displacement control mode. Samples were loaded at a constant loading rate of 30 nm/sec. The continuous stiffness measurement was applied by oscillating the indentation tip in 2 nm with a harmonic frequency of 35 Hz at every 100 nm displacement. Continuous force and displacement were recorded per nm and the Poisson's ratio of the testing materials was all assumed to be 0.3. These measured data were directly inputted into the built-in software in the nanoindenter using Oliver Pharr method to automatically calculate continuous stiffness. The maximum indentation depth was set up as 2 μm, and the maximum indentation force was set up as 22 mN. We averaged the stiffness measured at the indentation depth of the last 200 nm of the indentation depth (i.e. 0.8 – 1.0 μm for indentation depth about 1 μm and 1.8 –2.0 μm for indentation depth about 2 μm).

4.2.3 Optical microscopy and image analyses

Optical microscopy setups were done using a 20x magnification objective lens (NA=0.6). Spectra were detected *via* an optical fibre and a spectrometer. Detail setups were provided in Chapter 3. The measurements were conducted in a bright field configuration with small NA by restricting the opening of the aperture diaphragm of the microscope. This small NA leads to a line-shaped reflection colour along the top centre of each epicarpal cell (Figure 4.1B).

4.2.4 Coarse-grained molecular dynamic simulation

A coarse-grained cellulose microfibril model (CMF) was constructed as shown in Figure 4.10 which was a ball and stick model with every ball representing two D-glucose units linked by β (1→4)-glycosidic bonds. The coarse-grained parameters: bond lengths, bond parameters, and non-bond interactions were set up following the previous study [189] which are derived from the full-atomic simulation. Each cellulose chain is with 40 repeated D-glucose units (720 beads) resulting in 20 nm in length. Each CMF was constructed with cellulose Iβ crystalline composed of 36 cellulose chains as this is the most commonly occurring polymorphs in the higher plant cell wall [190,191]. The cross-section of each CMF is 3x3 nm^2.

The Molecular Dynamic (MD) package LAMMPS 2016 (http://lammps.sandia.gov) [192] was used. The CMF model structure was first equilibrated through energy minimization by using the Hessian-free truncated Newton algorithm followed by the microcanonical ensemble (NVE ensemble), in which the system is isolated from changes in moles (N), volume (V), and energy (E). In the NVE ensemble, I heated the system from 100 to 300 Kelvin (K) in 1 ns with the timestep of 1 fs. Following this, the system is run under

canonical ensemble (NVT ensemble) and isothermal–isobaric ensemble (NPT ensemble) at a temperature of 300 K and pressure of 1atm for 2 ns. In the ensembles, the amount of substance (N), pressure (P) and temperature (T) are conserved. The isothermal-isobaric ensemble corresponds most closely to laboratory conditions with a flask open to ambient temperature. Temperature and pressure were controlled by the Nosé-Hoover thermostat [193] and barostat [194].

After equilibrating the structure at targeted temperature and pressure, each CMF was applied tensile force along the longitudinal or transverse direction at the strain rate of 1 $\times 10^{-7}$ fs $^{-1}$. Stress and strain were recorded at every 0.0005 strain, and Young's modulus of CMF along the two directions was calculated.

4.2.5 Indentation test simulation

Contact mechanical properties were calculated by modelling a spherical indenter with a radius of 20 nm probing in a 150x 150x 300 nm^3 cube. Models were generated in the open-source software GIBBON (https://www.gibboncode.org/)[195]. The cube was composed of layers of fibre reinforced models composed of cellulose microfibrils (CMF) and the hemicellulose matrix (HC matrix). The CMF/HC matrix (5 nm in thickness), models were constructed by piling up each layer with certain small twisting angles (3.9 º-7.5º), I constructed the helicoidal models of CMF/HC layers with a pitch length of 120-230 nm. The HC matrix (Young's modulus: 10 GPa, Poisson's ratio:0.3) was calculated based on isotropic elasticity constitution models. The deformation of CMF (longitudinal Young's modulus: 150 GPa) was assumed nearly incompressible in the transverse direction and deformed exponentially with the deformation strain along the longitudinal direction).

Finite element calculations were conducted in the open-source software FEBio 2.8 (https://febio.org/) [196]. The indenter was modelled as an analytical rigid surface which was with triangulated meshes (3-node elements) with nearly geodesic triangle distributions. The cube contains hexahedral elements. Contact between the indenter and the surface of the cube was assumed to be frictionless and was modelled using a sticky contact formulation. The maximum indentation depth was 20 nm (the same as the indenter radius). Stress and displacement were recorded every 1 nm. The reduced modulus was calculated based on Hertz's law at the indentation depth of 2 nm, corresponding to an indentation strain of 0.05.

4.3 Results

4.3.1 Spatial and spectral distribution of cells

Pollia condensata is well known for its intense blue appearance (Figure 4.1A) created by the helicoidal structures of the cellulose cell walls [66]. The co-existence of left-handed cells and right-handed cells leads to different reflection colours of the *Pollia* fruit under two opposite circularly polarized filters. Both handed cells in *P. condensata* are possible to create entire ranges of visible light spectrum from blue to red colours (Figure 4.1B). Detail optical properties and underlying physics have been thoroughly discussed in our previous studies [21,66].

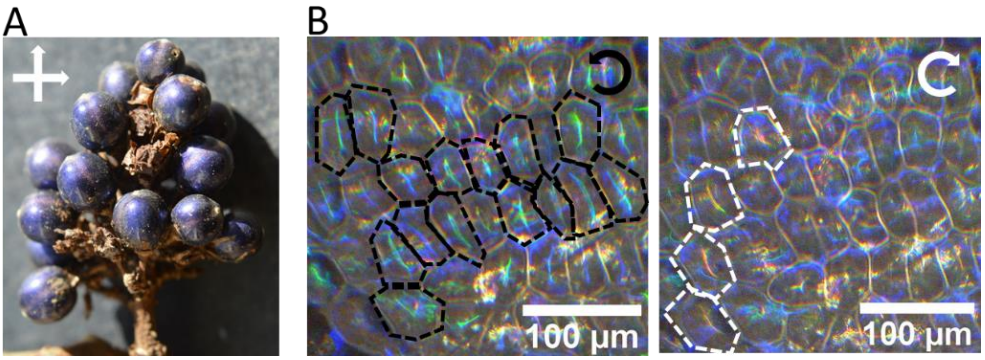

Figure 4.1 (A) The photo of *P. condensata* under unpolarized white light. Each fruit is with an ovoid shape with a diameter of 4-5 mm. (B) Circular polarisation microscopic images of the epicarp of a fruit. The two images are at the same location but are imaged under a left- or right-handed filter. Left-handed cells are framed with black dashed lines and right-handed cells are framed with white dashed lines. Cells have irregular six-sided shapes, and different colour stripes were produced by cellulose cell walls with the same chirality as the reflected light. Images are reproduced from [21]

Pollia condensata fruit is comprised of a hard, dry epicarp (outermost layer) packed with 18 tightly-packed seeds (see the anatomy in Figure 4.2A). In most *P. condensata* fruits the epicarp is with six stripes connecting the apex and calyx. The previous study reported that the coloured stripes visible on the fruits are compose of cells reflecting prevalently at larger reflective wavelengths [21], so these stripes appear purple and whitish than the rest of the fruit which is mainly blue, see positions (1) and (3) in Figure 4.2A. Three stripes are associated with the internal septa of the fruit, dividing the fruit into three locules. The other three stripes are equidistant and correspond to the dorsal capillary trace or the external vascular bundle which forms thickened tissues on the inside of the epicarp. Moreover, the cells in these stripes show a higher proportion of right-handedness (Figure 4.2C).

Dr. Middleton in our group has taken polarisation resolved spectra from more than 1000 individual cells found in four *P. condensata* fruits [21], and the results are summarized in the violin plots in Figure 4.2B. The reflection wavelengths of both handednesses of

cells confirmed that the reflection peaks in the spectra recorded from right-handed cells are on average red-shifted with respect to left-handed ones. In addition, by systematically sampling the reflection spectra and chirality of cells at white septum stripes (labelled (1)), blue inter-septum stripes (labelled (2)), and purple septum stripes (labelled (3)), the histograms in Figure 4.2C indicate the distribution of left and right-handed cells is patchy. Left-handed cells are far more numerous in the blue inter-septum area (locules) which cover the majority of the epicarp giving the overall blue visual appearance of the fruit. Right-handed cells are more abundant in the stripes. While there are differences in the abundance of two handednesses of cells at different positions on the epicarp, I observed that on average light reflected from right-handed cells are always of longer wavelengths.

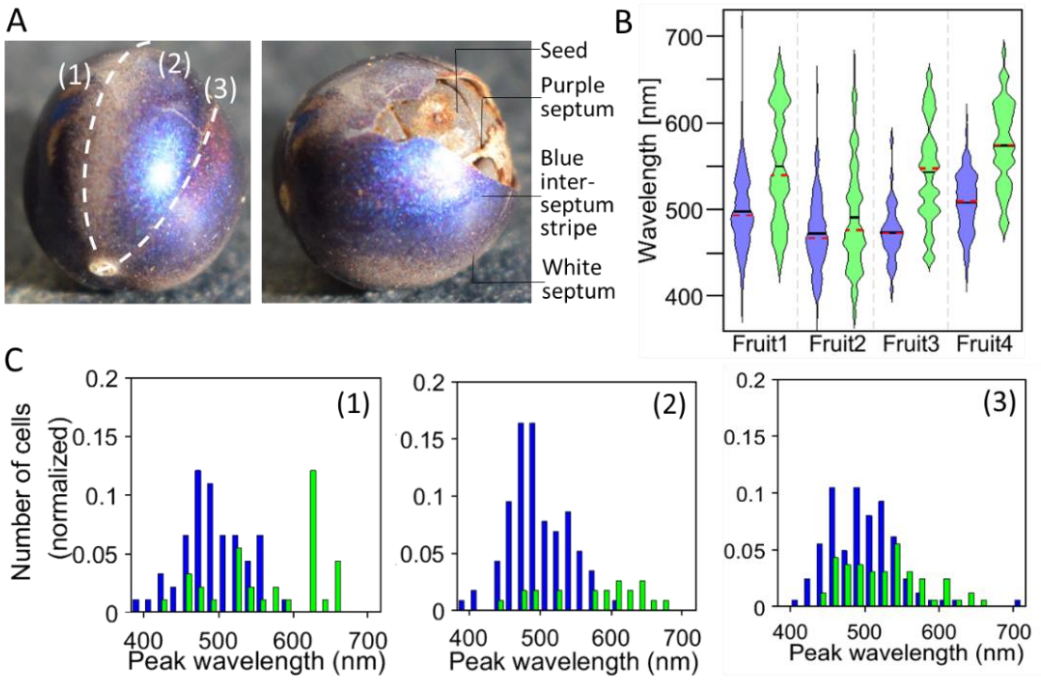

Figure 4.2 The distribution of differently coloured left and right-handed cells on the epicarp of *Pollia condensata* fruits reproduced from [21]. (A) Patchiness of the epicarp and the anatomy of the fruit reveals different regions and corresponding inner tissues: (1) a white septum stripe, (2) a blue inter-septum area, and (3) a purple septum stripe. (B) Distributions of the reflected wavelengths of left-handed

(blue violin body) and right-handed (green violin body) in four *P. condensata* fruits. The width of the violin corresponds to the number of cells with that peak wavelength. The red and black lines are the mean value and median value of each dataset. (C) The normalized number of left (blue bars) and right-handed cells (green bars) with corresponding reflected wavelength at the three different locations as marked in (A).

4.3.2 Hierarchical structures of the fruits epicarp

Previous studies have shown the unique hierarchically structural designs in the cell walls of the fruits of *Pollia condensata* [21,66]. These designs differ by cells that the reversal arcs and varied pitch lengths were found which perfectly explains different optical and mechanical responses produced by different cells. Here, we briefly describe the characterizations of structures reported in the previous studies [21] for relating to the optical and mechanical responses which are discussed in the following sections.

SEM images of the broken epicarp in cross-section are shown in Figure 4.3. The epicarp is composed of a thick cuticle at the outermost layer (3- 4 μm). 4-5 layers of structurally coloured cells are above 3-4 layers of pigmented cells, and thin layers of soft brown cells are on the internal surface of the epicarp (Figure 4.3A). Layered structures within the cell wall can be clearly seen in Figure 4.3B, and at a closer look at the broken faces, Bouligand arcs can be observed (Figure 4.3C). These arcs are characteristic of helicoidal architectures, and as shown in TEM images in Figure 4.4, opposite orientations are observed on six different cells indicate that the helicoids are of inverted chirality in different cells. Every individual cell possesses either left or right-handedness. The fact that in the same biological tissue neighbouring cells produce helicoids twisting in similar conformation, but opposite directions imply that minor differences of compositions in the cell wall may play a significant role in handedness.

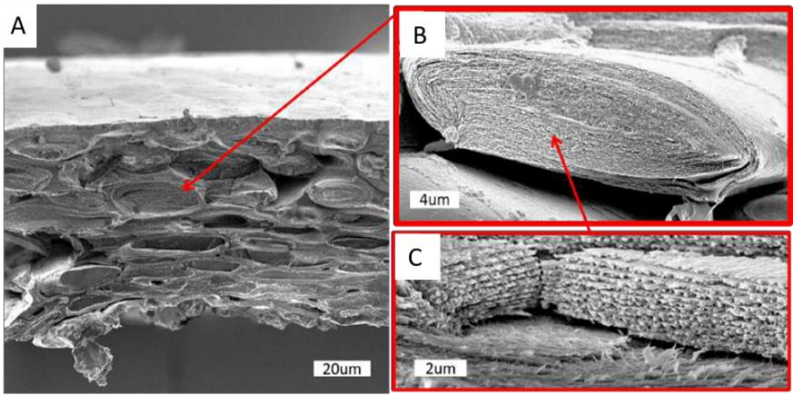

Figure 4.3 (A) A SEM cross-sectional image of the outer epicarp cells. Layers of the external cuticle, structurally coloured cells, and pigmented cells are visible from outer to inner. (B) A structurally coloured cell shows thick cell walls. (C) The high magnification image of the cell walls shows the helicoidal arcs. Images are adapted from [21] with the author's permission.

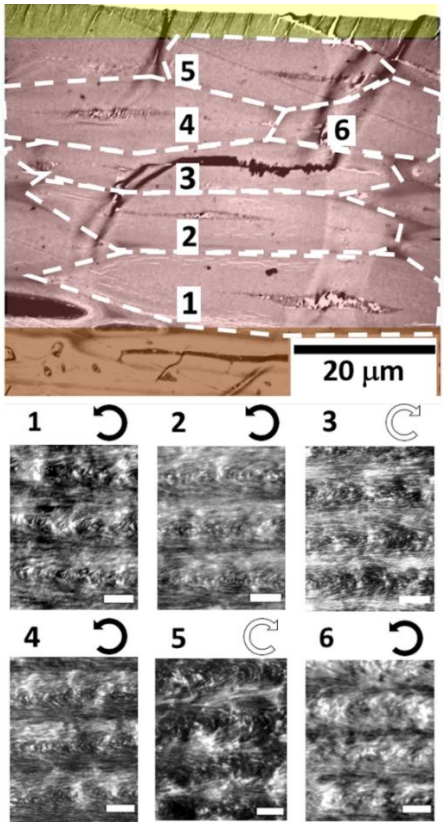

Figure 4.4 TEM images of the endocarp cross-section of fruit of *P. condensata* and enlarged images of the cell walls of six individual cells. Different regions are shaded with different colours: cuticle (yellow), structurally coloured cells (red) and pigmented cells (brown). Note that only one handedness can be found in each cell with no mixture of handedness. Varied pitch lengths are observed in cells which explain the wide reflected spectra from both cell types. Scalebar: 500 nm.

4.3.3 Development of cuticle removal techniques

The thick cuticle layer (3- 5 μm) can hugely affect the nanoindentation results and it is not possible to accurately indent the mechanical properties of the cells by first penetrating the cuticle. To directly measure the mechanical responses of the cellulose cell wall, the thick cuticle on the outermost layer was therefore removed to expose the cell wall before every nanoindentation test.

Different treatments were tested to optimise the removal of the cuticle without compromising the integrity of the other tissues of the fruit. Figure 4.5 shows the cross-sectional SEM images of fruits after chemical treatments (Soxhlet extraction with Toluene or Chloroform) and physical methods (polish with sandpapers). Continuous chemical treatments for one month can only remove the cuticle of about 1 μm, and obvious changes in the visual colour of the treated fruits are observed. These indicate the removal of the outer cuticle by chemical treatments is not efficient, and that the structural integrity is damaged by chemicals.

Physical methods are relatively efficient to remove the outer cuticle layer and avoid damaging the internal structure. Although physical treatments cannot remove the outer cuticle uniformly, and in some instances remove part of the cell wall, neither of these two consequences is expected to affect the nanoindentation results with an indentation depth of 1-2 μm. Therefore, I applied the physical treatments to remove the cuticle and polish the surface of every fruit before nanoindentation tests.

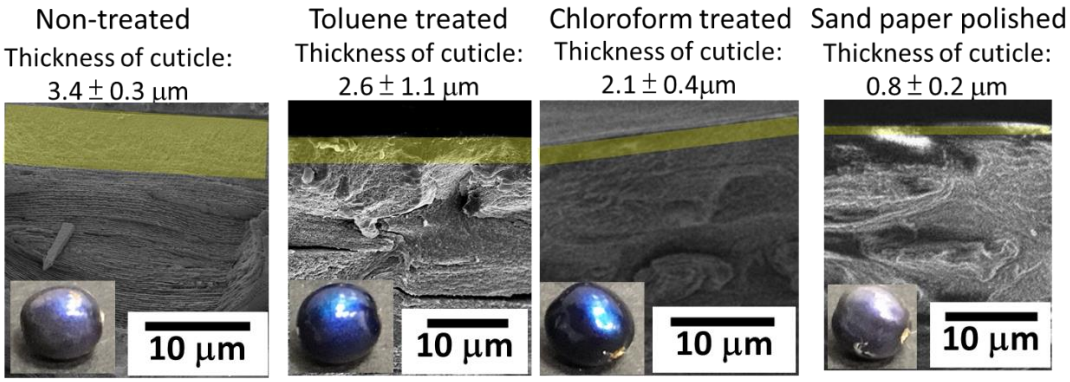

Figure 4.5 Treatments and the effects on the structures of the *P. condensata* fruits. Photos of non-treated and chemically treated fruits reveal the changes of visual colour from purple to blue after treatment. The SEM cross-sectional image of non-treated *P. condensata* fruits shows a thick waxy cuticle with a thickness of 3.4 ± 0.3 μm covering the outermost layer of the epicarp. Chemical treatments with Toluene or Chloroform for one month can remove some cuticles (~1 μm). Physical treatments with sandpapers are more effectively to remove the thick cuticle layer.

As illustrated in Figure 4.6A, the cells after cuticle removal were further polished with fine-grained optical papers to confirm the surface is sufficiently smooth (<300 nm) to (i) be imaged with the optical microscope, (ii) measure the spectral response of the cells and finally (iii) undergo cell wall nanoindentation with the negligible effect of surface roughness.

4.3.4 Mechanical properties and chirality

An indentation was conducted by using a Berkovich tip probing the top surface at the centre of each cell (as the indent mark at the centre of the six-sided cell as in the top SEM image in Figure 4.6A). The central location was chosen corresponding to the region where the reflected colour was visible, indicating that the normal to the surface was closely aligned with the optical axis.

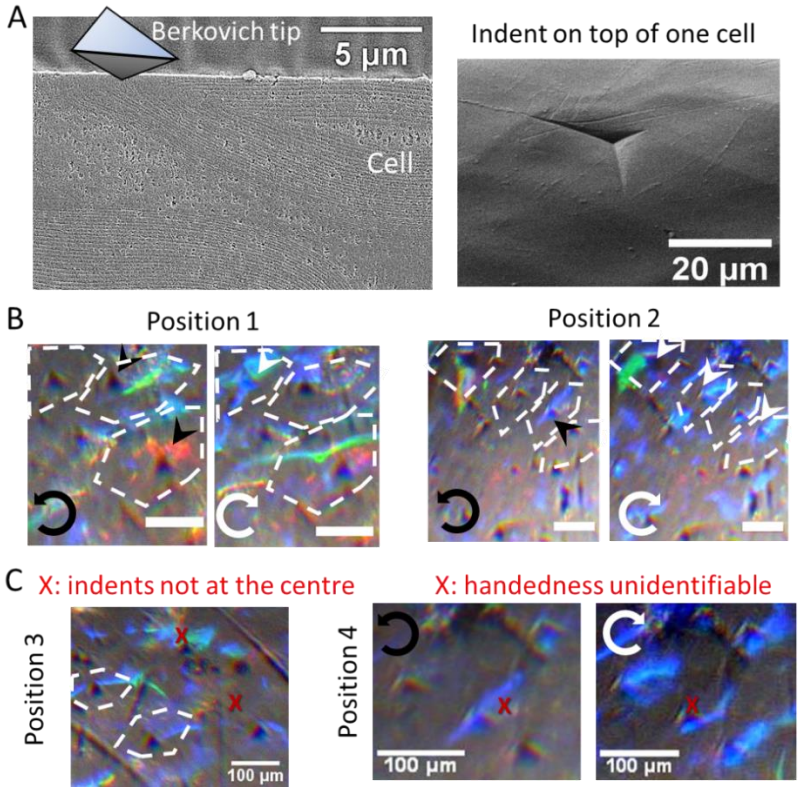

Figure 4.6 Nanoindentation on cells with different colours and handedness. (A) Illustration of the indentation with a Berkovich tip on cells after removing the outer cuticle. The top-view SEM image shows an ideal indent at the centre of each cell without crossing any edge. (B) Representative images of the same position under left- and right-handed polarized filters after polishing and indentation tests demonstrate how each indent is related to a specific colour and handedness (Left-handed cells: black arrowheads; Right-handed cells: white arrowheads.). Each cell is framed with white dashed lines along the cell wall. Scale bar: 20 µm. (C) Abandoned indentation data (red cross) for indents on cell edges and with unidentified handedness.

Indentation left a mark on the cell wall that is visible both on the SEM and optical images, see Figure 4.6B,C. Based on post optical image analyses, indents were classified by handedness and colour with the left and right-handed polarisation filters as shown in the four enlarged images (two positions under either left or right-handed polarisation filter) in Figure 4.6B. Indentations on cell edges where the helicoids were not normal to the surface or on cells for which the handedness was unidentifiable were excluded from the analyses (marked as the red cross in Figure 4.6C).

The continuous elastic modulus and hardness of each cell were measured to an indentation depth of 1-2 μm. In Figure 4.7 I observed that after removing the cuticle layer on the surface of *P. condensate*, the nanoindentation tested moduli are higher than the untreated ones at the same indentation depth because it directly probes into the cell walls. The E and H of each cell are the mean values of the last indent depth of 200 nm (e.g. of indentation depth of 0.8- 1 μm for a total indentation depth of 1 μm). The average modulus of untreated epicarpal cells is 3.43 ± 0.71 GPa which is much lower than those physically removed cuticle at 10.82 ± 2.34 GPa. Likewise, the hardness of cells after removing the cuticle is 0.95 ± 0.19 GPa which is twice those without any treatment at 0.45 ± 0.05 GPa. The increase in E and H of left or right-handedness cells after removing the cuticle layer right-handed are listed in

Table 4.1, respectively. 224 of 320 indentations from five different *Pollia* fruits were successfully related to the colouration and handedness of the helicoidal structure. Comparisons of mechanical properties of two handedness cross the five fruits are shown in Figure 4.8.

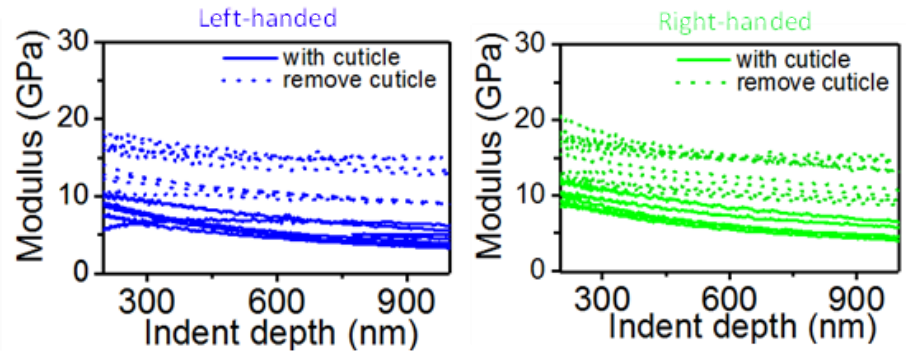

Figure 4.7 Modulus detected continuously at different indentation depths from the outer surface of the epicarp. The mean moduli of untreated *Pollia* fruits (average value at depth of 2 μm) is much lower than the cuticle removed samples (average value at depth of 1 μm). Data of depths smaller than 200 nm are not shown because the uncertainty of values at low indentation depths

Table 4.1 Mean values of E and H of the left-handed and right-handed cells in the untreated and cuticle removed samples.

	Modulus (GPa)		**Hardness (GPa)**	
	untreated *Pollia*	removed cuticle	untreated *Pollia*	removed cuticle
Left-handed	2.80 ± 1.18	11.45 ± 3.38	0.37± 0.08	0.97± 0.29
Right-handed	4.05 ± 0.80	10.19 ± 3.24	0.53 ± 0.06	0.92 ± 0.24

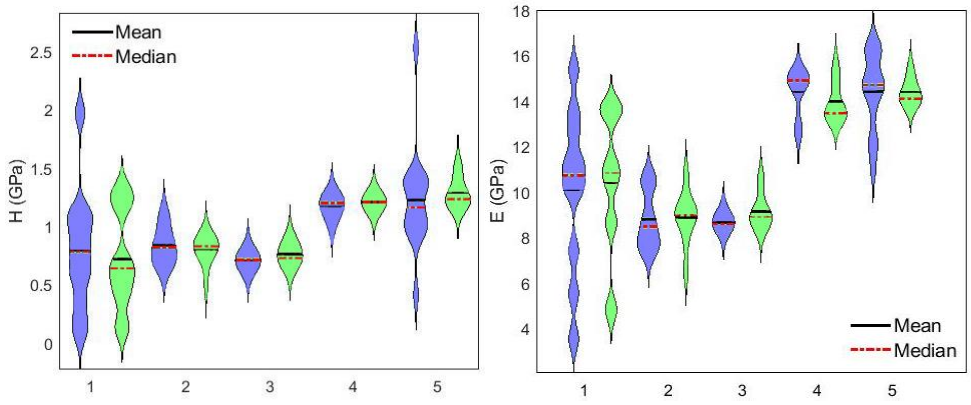

Figure 4.8 E and H of left-handed (blue) and right-handed cells (green) in 5 *Pollia* fruits.

To investigate the generality and individual difference of mechanical properties of *P. condensata*, I indented several areas at different positions on each fruit and recorded the E and H of every cell (including both handednesses). The stiffness and hardness at many randomly chosen areas on each fruit were recorded and plotted as violin histograms. Each violin body (labelled along the x-axis) corresponds to an individual fruit specimen. The width of the 'violin' for each point on the y-axis corresponds to the frequency of cells found at each E or H. Mechanical properties such as the mean values and spread of E and H are significantly different between fruits, while similar for left-handed and right-handed cells in the same fruit.

Figure 4.9 shows the nanoindentation measurements of E and H for each cell handedness according to four colour classifications. Helicoidal structures reflecting longer wavelength have larger pitch and tend to have higher E regardless of handedness, meaning that they deform less under the same stress. Moreover, it seems that left-handed helicoids have higher E than right-handed ones at shorter wavelengths, see Figure 4.9 and two-sample t-test analyses in Table 4.4.

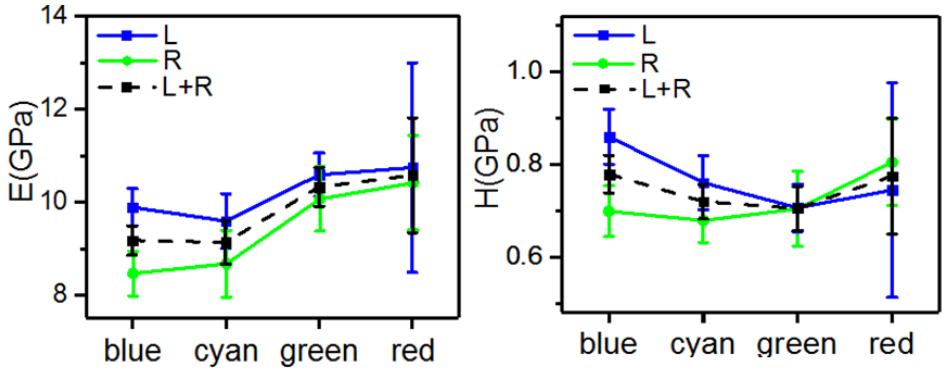

Figure 4.9 Statistics of indentation detected reduced modulus E and hardness H, from successfully mapped 224 data from 5 fruits. On average (the black dashed line) red-shifted cells have higher E. A similar trend is shown by both chiralities although left-handed cells are stiffer than the same coloured right-handed cells. H of differently coloured cells is constant at 0.7- 0.8 GPa. Left- and right-handed cells show an inverse trend of H with lengthening pitch: longer pitch left-handed cells have lower H, but longer pitch right-handed cells have higher H.

Similarly, hardness (H) of cells is higher for left-handed helicoids than right-handed ones at shorter wavelengths, while the average value of H remains constant, within the error, with longer wavelength colour (cells with longer pitch). The larger error for the value of E and H in longer pitch (red-shifted) left-handed cells is due to lower sample numbers as red cells are predominantly right-handed (numbers of cells in each group are listed in Table 4.2), however, they seem not to contradict to the trends. Statistical analyses including the Shapiro-Wilk test (Table 4.2), One-way ANOVA (Table 4.3), and

two-sample t-test (Table 4.4) were conducted to interpret the relationship between the stiffness (valued by elastic moduli) of differently coloured or handed cells.

The Shapiro-Wilk test is a test of normality that assesses whether a sample is likely to originate from a normal distribution. Verifying normality of distribution is a requirement for running statistical tests such as Student's t-test and ANOVA. In this test, the null hypothesis states that the sample comes from a normally distributed population. The standard of the null hypothesis is set at 0.05. If a p-value is well over 0.05, the null hypothesis is not rejected. Such means that the sample is very likely to be normally distributed. If a p-value of a sample is less than 0.05, it means the null hypothesis is rejected. Such rejection means either (1) the sample does not follow the normal distribution, or (2) the sample size is too small. Table 4.2 shows cells from blue to green with any handedness are all normally distributed. The red cells with either left-handed or right-handed reject the Shapiro-Wilk test which means these two samples should not be imported into later statistical tests.

Table 4.2 Normality of cells of different colours and handedness by Shapiro Wilk test with the *p-value* standard of 0.05. The lack of red cells datasets makes their indentation results not statistically comparable to other coloured cells.

Left-handed cells					
Cell color	**Samples (#)**	**E (GPa)**	**Statistic**	***p-value***	**Decision at level 0.05**
Blue	45	9.89± 2.68	0.98668	0.87822	Normal distribution
Cyan	31	9.59± 3.29	0.96862	0.48189	Normal distribution
Green	43	10.59± 3.03	0.9651	0.21232	Normal distribution
Red	5	10.74± 5.03	0.84636	0.18327	-
Right-handed cells					
Cell color	**Sample (#)**	**E (GPa)**	**Statistic**	***p-value***	**Decision at level 0.05**
Blue	43	8.47± 3.19	0.96772	0.26337	Normal distribution
Cyan	18	8.68± 3.05	0.96255	0.6516	Normal distribution
Green	26	10.07± 3.52	0.94973	0.22849	Normal distribution
Red	13	10.41± 3.67	0.86636	0.04677	Not normal distribution

The one-way ANOVA is run to verify if any group of the cells possesses different moduli comparing to the other groups with different colours or handedness. (Noted: data of red cells are excluded due to non-normality distribution). The outputs presented in Table 4.3 shows *F-value* (2.52352) and *p-value* (0.05859) of differently coloured cells. At the significance level of *p-value* of 0.05, the population means of blue, cyan, green, or red cells are not significantly different. On the other hand, *F-value* (4.31915) and *p-value* (0.03886) of differently handed cells means at the significance level of *p-value* of 0.05, the population means of left-handed or right-handed cells are significantly different. From one-way ANOVA tests, I found the handedness of cells is actually the main effect of a factor, but the test results do not tell which group is actually a factor. Next, I conducted the two-sample t-tests on the samples with the same colour but opposite handedness. Two-sample t-tests in Table 4.4 reveals significant differences in the stiffness of cells with left or right-handedness in particularly the blue cells.

Table 4.3 The one-way ANOVA tests of the differently coloured cells, or the differently handed cells.

Colour of cells					
	DF	Sum of Squares	Mean Square	*F-value*	*p-value*
Colour	3	76.97684	25.65895	2.52352	0.05859
Residuals	220	2236.9421	10.16792		
Handedness of cells					
	DF	Sum of Squares	Mean Square	*F-value*	*p-value*
Colour	1	43.06729	43.06729	4.31915	0.03886
Residuals	217	2163.76101	9.97125		

Table 4.4 Two-sample t-test of the same coloured left-handed and right-handed cells. Blue coloured cells show the significantly different modulus (E) of left and right-handedness with the *p-value* standard of 0.05.

	Left blue vs Right blue	**Left cyan *vs* Right cyan**	**Left green *vs* Right green**
p-value of E (GPa)	0.025 (significant difference)	0.331	0.531

The helicoidal structures and mechanical responses relationships are diverse due to various fibre phases and combinations with matrix phases in the structures. Many studies have shown helicoidal structures effectively enhance the material toughness [122,127,197]. It was proposed that the complicated interfaces in the helicoidal composite can redirect the crack growth direction to stop cracks directly penetrating through the materials and thus increasing the toughness. However, how the helicoidal structure affects stiffness lacks discussion [197,198].

Only a few computational works have been done to predict the stiffness of cellulose composites. These pioneering works suggest the mechanical properties of the cellulose composites are greatly enhanced by a higher density of cellulose microfibrils (CMFs) and lignin, and the stiffness is sensitive to the interaction forces between cellulose microfibrils (CMFs) and hemicellulose (HCs) [33,127,199,200].

To investigate the effects of twisting angle and density of CMF and HC on the stiffness of the helicoids, I started with coarse-grained molecular dynamic simulation to derive reasonable CMF geometry and mechanical responses for extracting the modulus of the CMF. Each CMF is cellulose Iβ crystalline with diamond symmetry composed of 6 cellulose chains (Figure 4.10A). Through tensile deformation simulation along the longitudinal direction (Figure 4.10B) and transverse direction (Figure 4.10C), I derived the longitudinal modulus of 150 GPa and transverse modulus of 35 GPa of each CMF which match the reported data from the experiment [184,186,191,201] or full atomic simulation [189]. The displacement of each CMF model is very small indicating it is incompressible.

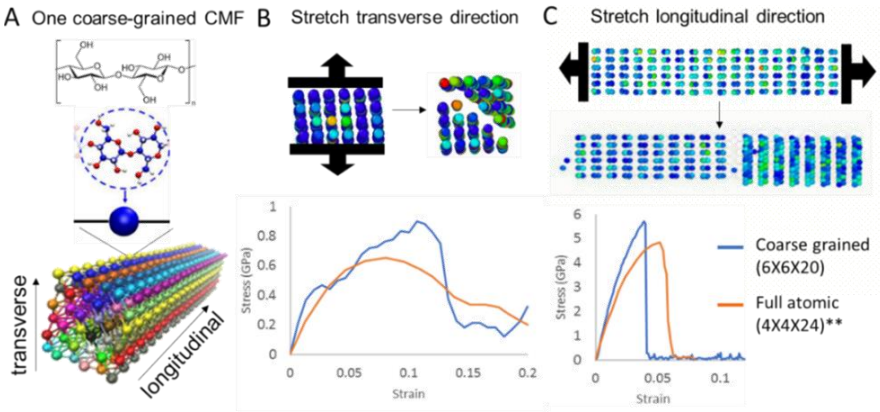

Figure 4.10 (A) A coarse-grained cellulose microfibril (CMF) model with each ball represents two D-glucose units linked by β (1→4)-glycosidic bonds. One CMF was stretched along (B) transverse direction and (C) longitudinal direction, and the stress and strain were recorded until the fibre breaks for calculating the directional stiffness and yield strain.

Although the reflection colours of helicoidal structures can be approximated by the Bragg's law, the experimentally characterized spectra from the helicoidal biomaterials can deviate from such estimations a lot because of (1) the refractive index and the birefringence of the microfibrils (2) the repeats of pitches and the thickness of the helicoidal layers. Therefore, in this previous work in our group, Dr. Middleton constructed real-sized cellulose helicoidal models and calculated the reflection spectra from such models with the Finite-Difference Time-Domain simulations (FDTD). By numerical calculation, she found the reflection wavelengths (λ) and pitch lengths (*P*) in cellulose helicoids follow this linear relationship: $\lambda = 3.03*P + 8.74$ [21]. By inserting the statistical data of cellulose helicoids in the cell walls of *P. condensate* (presented in Figure 4.2B) into this equation, we derived the average and range of the pitch lengths of left-handed cells and right-handed cells, respectively. For example, the reflection wavelengths of the left-handed cell have an average of λ_{Left}= 495.8 nm and are in the full range of $\Delta\lambda_{Left}$= 370.8- 618.1 nm which corresponds to an average pitch length of P_{Left} = 160.7 nm and of the pitch length full range of ΔP_{Left} = 119.5- 201.1 nm. The

average reflection wavelengths of right-handed cells are of λ_{right}= 551.4 nm in the full range of $\Delta\lambda_{right}$= 418.1- 683.3 nm which corresponds to an averaged pitch length of P_{right} = 179.1 nm and the full range ΔP_{right} = 135.1- 222.6 nm.

Using the finite element analysis (FEA) I computed a spherical indentation of composites composed of helicoidally arranged cellulose microfibrils (CMF) in a hemicellulose matrix to understand how the following factors contribute to the stiffness of helicoids: (i) the volumetric filling fraction of CMF in the composite model with the hemicellulose matrix (HC matrix), (ii) the diameter of the CMF, and (iii) the twisting angles of the CMF layers. I constructed finite element models of helicoids with CMF diameter from 3-6 nm and with CMFs in a hemicellulose matrix with a filling fraction of 0.1, 0.2, or 0.3.

The FEA model is schematized in Figure 4. 11. In these models, a larger twisting angle between the CMF layers results in a smaller pitch when the fibril diameter and the filling fraction are constant.

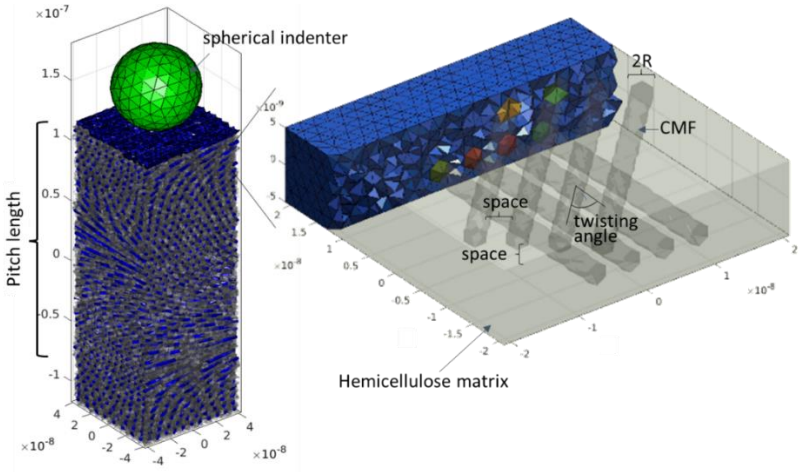

Figure 4. 11 Illustration of the finite element model (FEM) of the indentation test on a helicoidal cellulose microfibril (CMF)/ hemicellulose matrix composite. Each CMF has a radius R and defined space to its neighbouring fibril. The adjacent CMF layer has the same spacing and is rotated by a defined twisting angle. The arrangement corresponds to a filling fraction of 0.1,0.2, or 0.3 and pitch lengths from 120-220 nm.

In each geometry condition, I calculated the stiffness of CMF helicoids with different pitch lengths from 120-220 nm. The calculated results shown in Figure 4. 12 indicate the stiffness of the cell walls and their microfibril orientations are not strongly correlated.

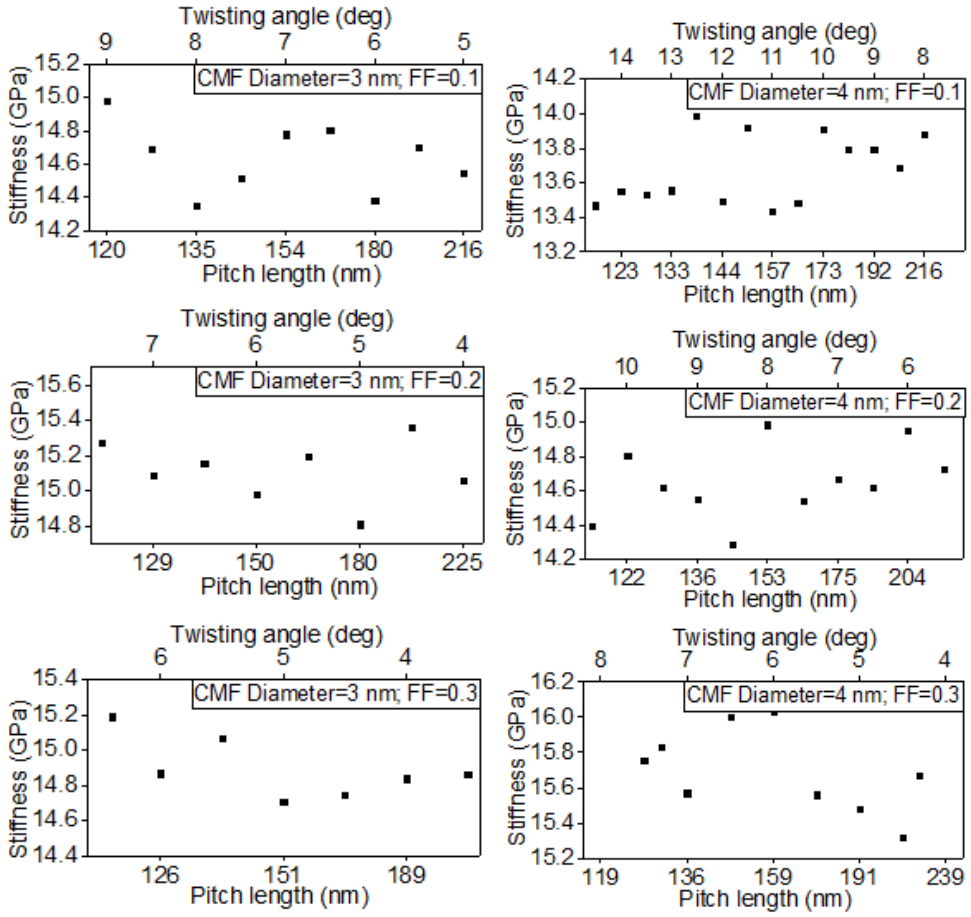

Figure 4. 12 Correlations between stiffness and twisting angles of helicoidal layers (i.e. fibre orientations). The pitch length of each model is a function of the diameter of each cellulose microfibril (CMF diameter), the filling fraction, and the twisting angle of fibres. Each graph demonstrates the relationship of stiffness with twisting angles of fibres with specific diameter.

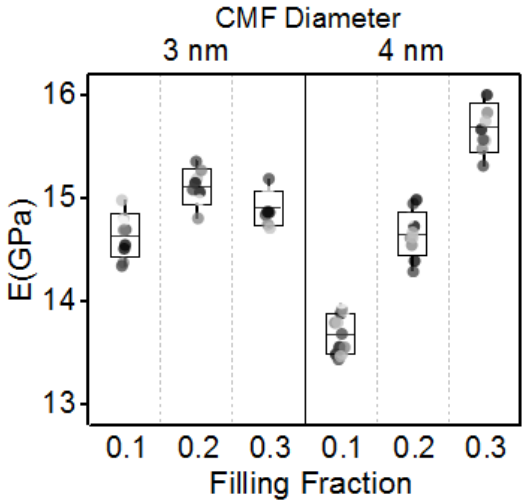

Figure 4. 13 Computationally calculated stiffness of models with CMF diameter of 3 nm or 4 nm with varied filling fraction of 0.1, 0.2, or 0.3, respectively, and pitch lengths from 120 to 220 nm (represented by spots with different greyness: the darker spots indicate models with larger pitch lengths). The maximum and minimum values of stiffness in each condition were labelled on the graph.

Figure 4. 13 organized the calculation data from different models, and I found there is no correlation between pitch length and stiffness. In contrast, the average stiffness of the cell wall varies strongly with CMF diameter and the filling fraction of CMFs in the composite. These results indicate a strong correlation between the stiffness of the cell walls and their composition, but not a correlation between the stiffness and the orientation of CMFs in the helicoid.

4.4 Discussion

Epicarpal cells of *Pollia condensata* are very interesting biological systems in plants that the neighbouring cells can produce helicoids twisted in opposite directions and with different pitch lengths. I also found left- and right-handed cells have many differences in the distribution and properties: (i) the occurrence of right-handed cells is relatively lower than left-handed ones; (ii) right-handed cells are mainly located on

locular division lines; (iii) colours reflected from right-handed cells are statistically red-shifted compared to those from left-handed cells. This work furthermore showed (iv) right-handed cells have average lower elastic moduli compared to left-handed cells of the same colour and (v) redder cells (that is, cells with larger pitch) have higher elastic modulus, and (vi) cross-scaled simulations suggest the twisting of cellulose fibrils and the density of hemicellulose might result in the different stiffness of cells with different pitch lengths and handednesses. These findings of the spatial, spectral, and mechanical differences of cells with different colours or handednesses suggest that compositions of cell walls may play a significant role in forming the helicoidal structures and developing reversal handednesses.

It is important to remember that different colouration corresponds to helicoidal structure with a different pitch length, specifically that cell walls reflecting red colouration have longer pitch than those reflecting blue. The pitch length can be increased in different ways: for example by increasing the average distance between cellulose microfibrils cores, either by (1) decreasing the twisting angle between the average orientation of the microfibrils, or (2) increasing the diameter of the cellulose microfibrils, or by (3) different filling fractions of cellulose microfibrils, or obviously (4) a combination of all the three factors. To better address which hypothesis is more plausible, it is important to first discuss composition and assembly of the secondary cell wall.

As in many other secondary cell walls, the cell wall of *P. condensata* is mainly composed of three components: cellulose, hemicellulose and lignin. Preliminary analysis of sugar compositions of the cell wall in our group indicated that hemicellulose in *P. condensata* belongs to the family of xylans (Dr. Steiner et al. in preparation). As the lignification occurs only after cell wall deposition, we speculate that the lignin does

not play a significant role and therefore we idealize the cell wall as a composite of cellulose microfibers within a hemicellulose matrix. My computation results reveal hypothesis (1) is the least possible cause of higher stiffness of redder cells.

Hypothesis (2) is less plausible from the biological aspects. It is difficult to imagine that in the same tissues, the fruit developed different sizes of cellulose fibrils. Thus, from biological and mechanical aspects, hypothesis (3) seems the main reason resulting in the higher stiffness of redder cells. For example, based on my current simulation results, the redder cells might have a higher filling fraction of CMF than the bluer cells.

On the other hand, for the case of identical compositions, left-handed and right-handed helicoids theoretically should show the same mechanical responses. However, I observed higher mechanical strength in left-handed cells for a given pitch. I speculated that the hypothesis (3) compositional difference such as the density of cellulose and hemicellulose is still the most probable factor resulting in the mechanically different responses of left- and right-handed cells. Such different interactions between the cellulose nanofibrils with hemicellulose also possible lead to chirality inversion during cell wall deposition. This hypothesis seems more probable than a difference in the way the morphological properties of the cellulose (i.e. size and crystallinity) or how it is deposited, which would involve completely different trafficking of the cellulose synthase rosettes across the cell wall membrane.

Our hypothesis is also supported by the fact that right-handed cells are predominantly observed in correspondence to the vascularised and connective tissues of the whole fruit. Given the functional properties of these tissues, the occurrence of distinct groups of right-handed cells in these regions could indicate that their development is linked to that of the connective tissue. This may indicate the conditions under which the cells

differentiate, producing different amounts of types xylans responsible for the unusual right-handedness.

In conclusion, I have shown how nanoindentation on the surface of cell walls can be used to compare mechanical differences at the single cell level. We were also able to correlate these mechanical properties to the internal structure of the cell walls through optical analysis of the reflection from the cell walls. The higher average modulus in left-handed cells compared with the same colour of right-handed cell suggests a compositional difference in the cell walls. Given the extreme rarity of right-handed helicoids in natural fibrillar materials, this discovery indicates how cell wall composition might be able to regulate handedness in the cell wall architecture, shedding some light in the long-debated problem of the development of such structure in plants.

Chapter 5
Hereditary structural colours in *Pachyrhynchus sarcitis*

Pachyrhynchus sarcitis from two different islands have evolved yellow (male) and blue scales (female) by each tuning the lattice constant of photonic crystals within their scales. Their first generation surprisingly possesses a mixing colour of green which is independent of the sex of parents. Unexpectedly, the mixing colour is not from the crystal structure with an intermediate lattice constant but a different distribution of preferred crystal orientations with the lattice constant inherited from the red parent independently from their sex.

The content of this chapter has been published to *Adv Opt Mater 8:2000432*. I acknowledge Dr. Onelli for assisting the project at the beginning and helping on optical measurements and analyses. I thank to Dr. Ogawa for preparing samples for EM imaging and for imaging almost 100 samples. I acknowledge Dr. Tseng for breeding and hybridizing the weevils in Taiwan and keeping providing us the samples. Finally, I acknowledge all the co-authors on commenting this research and writing the manuscript.

5.1 Introduction

The Coleoptera is the largest order constituting 40% of described insects and is known for their evolutionary success on the visual diversity [202]. They have brilliant coloured appearances which have disclosed various photonic structures and optical effects [78]. Diverse photonic structures have been discovered in Coleoptera from the perfectly periodic in three-dimensions to disordered ones [203]. The mechanisms of how these three-dimensional photonic crystals produce vivid structural colours in a variety of beetles have recently been extensively studied [46,101,203–205]. These three-dimensional crystals comprise of a chitin-like matrix (refractive index= 1.55) in the air (refractive index= 1) result in a high refractive index contrast.

In the order Coleoptera, the Curculionidae is the largest of all families and their elytra are covered with scales with three-dimensional photonic crystal structure inside (see Figure 5.2). Their vivid colours are generated by bicontinuous cubic crystals with triply periodic networks (see Figure 5.4) [22,206,207].

The low refractive index contrast along with highly ordered diamond structures lead to a complete photonic band-gap [208,209] which opens up the range of colours can be reflected. The photonic crystal structures in the scales of many weevils in this family have been characterized by SEM [46,51,209–211] FIBSEM [205,210,212,213] and SAXS [22,51,206,207,209], the studied species and structural parameters are listed in Table S1. For example, Saranathan et. al. [206] used SAXS to characterize 140 scales of species in 85 genera and verified that most of the weevils in Curculionidae family have three-dimensional single diamond photonic crystal structures. They also found few weevils have disordered sponge structures, single gyroid structures, face-centred orthorhombic structures, or a mix of structures on the same scale. Recently, Seago, Oberprieler, and

Saranathan related the distribution of three-dimensional photonic crystals to the phylogenic tree of the Curculionidae family, and they deduced the structure evolution based on the SAXS detected results [207].

It should be noticed that the crystal structures obtained by SEM, however, are all reported as diamond-based structures. Other crystal structures are identified only by SAXS. The crystal structure and lattice parameters of some species are still controversial. For example, photonic crystals in scales of *Lamprocyphus augustus* were reported as diamond-symmetric structures by Bartl and colleagues through SEM-based images [205], but were reported as a mixture of single diamond and single gyroid crystals by Saranathan et al. through SAXS [206]. In 2018, *L. augustus* was again characterized as a single diamond structure but with a much smaller lattice constant than the value reported in previous research [213].

Pachyrhynchus weevils belong to the Curculionidae family. *Pachyrhynchus* are very popular for the vivid and colourful patterns decorated on their dark exoskeletons. As they are flightless, they are distributed exclusively on several islets of Southeast Asia and display high insular species diversity [4,214]. So far, their ecology is poorly understood, and their taxonomy is based only on the optical appearance [215–217]. Due to the difficulties in identifying species with similar appearances, there was an error in misidentification, and *Metapocyrtus* were erroneously reported as *Pachyrhynchus* weevils by Parker [211]. Some pioneering works reported incorrect crystal structures [204,218] and only recent studies [22,206,209] correctly analysed the morphology and the optical response of the weevils' scales. Along with the limits and artefacts on characterization techniques, photonic crystal structures and structural parameters of some *Pachyrhynchus* weevils will require a careful measurement with larger sample size on controlled samples. Only recent progress on DNA fingerprints analyses enabled to more

precisely identify species, and as a consequence, many new species were discovered and corrected from previous misidentification [219].

Regardless of the uncertainties resulting from mentioned issues, diverse colourations of *Pachyrhynchus* weevils are observed. Different colours are achieved with diamond photonic crystals by changing volume fractions [209,210], lattice constants [209,210,212], or crystal orientations [62,220]. While the optical properties of *Pachyrhynchus* weevils are extensively studied by several groups in the field, the understanding on how the structural colour phenotype is inherited by hybrid weevils, and more in general for insects, is still missing, as it is challenging to grow these species in captivity [221].

In this chapter, I optically and anatomically monitor the hereditary characteristics of the diamond photonic structure of *Pachyrhynchus sarcitis* (*P. sarcitis*) *via* a hybridization technique. In particular, I observe that, irrespectively of the sex of the parents, the first-generation cross blue-spotted and yellow-spotted *P. sarcitis* weevils inherits a green-spotted pattern. A careful spectroscopical and anatomical analysis of the weevils in the phylogeny reveals the hereditary characteristics of the photonic crystals within their scales in terms of lattice constant, orientation and domain size. Monitoring how structural colouration is inherited by offspring highlights the versatility of photonic structures to completely redesign the optical response of living organisms and therefore sheds light onto the evolution and development mechanisms of structural colouration in *Pachyrhynchus* weevils.

5.2 Materials and methods

5.2.1 Species Selections

Adults of *P. sarcitis* were collected from Babuyan (19°32’ 58”N, 121°54’ 40”E) and Lanyu (22°4’44.57”N, 121°33’15.25”E) Islands. These two populations have almost identical appearances, except colouration. Captive-breeding of Lanyu *P. sarcitis*, Babuyan *P. sarcitis* and hybrid *P. sarcitis* were conducted in the laboratory in National Taiwan University (Taipei, Taiwan).

5.2.2 Optical microscopy and image analysis

Optical microscopy with a 50X SLWD objective (Nickon, NA=0.4) was used, and reflection spectra were taken with an optical fibre (Thorlabs, FC-UV100-2-SR). Detailed setups were provided in Chapter 3. Spectra were normalized with a silver mirror (Thorlabs, PF10-03-P01). Scales were detached from the elytra and placed on a glass slide. Spectra of different domains on each scale were measured. Domain colour distribution was quantitatively analysed by image-based RGB analysis on many single scales in each weevil with ImageJ Software (http://rsb.info.nih.gov/ij/).

5.2.3 SEM sample preparation and image analysis

For the top view SEM images, scales were detached from the elytra and placed on a glass slide and plasma etched for 13 minutes to remove the outer shell of scales. The etched scales were transferred onto SEM stubs and coated with 10 nm Pt. The SEM (Tescan MIRA3 FEG-SEM) used to observe the top view was operated at 3 kV with a working distance of 5.2 mm and using an in-beam secondary electron detector.

For the cross-sectional imaging, the scales still attached to the elytra were directly embedded in Embed 812 resin (EMS, Hatfield, USA) and hardened overnight at 60 °C. After resin embedding, the scales were transversely cut with a 35° diamond knife

(Diatom, USA) equipped on an ultramicrotome Leica EM UC6 (Leica Microsystems, Germany). The newly made block face was further treated with 2% osmium tetroxide aqueous solution to enhance image contrast. The cross-sectional SEM observation was carried out with a field emission SEM (Quanta-FEG 250, Thermo Fisher Scientific Inc., U.S.A.) operated at 7 kV and using a concentric backscattering electron detector.

5.2.4 Finite-difference time-domain simulation (FDTD)

Three-dimensional diamond models were constructed in MATLAB. Finite-difference time-domain (FDTD) calculations were performed with the commercial software Lumerical. Different crystal orientations were oriented in the simulation box perpendicular to the direction of light incidence. I modelled reflection properties of the diamond structures composed of cuticular proteins and air spaces with experimentally determined refractive index n= 1.53 (measured *via* index matching oils Cargille series A). Diamond minimum surface equation: $f(\mathrm{X},\mathrm{Y},\mathrm{Z}) = \cos(\mathrm{Z})\sin(\mathrm{X}+\mathrm{Y}) + \sin(\mathrm{Z})\cos(\mathrm{X}-\mathrm{Y})$ where $X = {}^{2\pi x}/_{a}, Y = {}^{2\pi y}/_{a}, Z = {}^{2\pi z}/_{a}$ with a: the lattice constant; x, y, z: the coordinates was used for constructing models. Simulation models were constructed with experimentally measured domain sizes. To correlate the colour with the different orientations in the three weevils, the simulation boundary conditions were set to be periodical for x and y dimensions. The z-direction was set to be perfectly matched layer (PML) to take into account the measured limited thickness.

5.3 Results

5.3.1 Optical appearance and physiology

Figure 5.1 shows images of the optical appearance of the parent *P. sarcitis* weevils and their first filial generation, hybrid *P. sarcitis*. Adults of *P. sarcitis* populations are captured from two isolated locations, they have similar patterns on the exoskeletons, but the patterns are formed by differently coloured scales. *P. sarcitis* collected from Lanyu Island possess a blue-spotted pattern (abbreviated as LPS), and those captured from Babuyan Island possess a yellow-spotted pattern (abbreviated as BPS).

Hybrid *P. sarcitis* (abbreviated as HPS) weevils obtained from mating the two types of *P. sarcitis* by our collaborator Dr. Hui-Yun Tseng's lab in National Taiwan University. Readers interested in the breeding technique are referred to the paper [221]. Regardless of the sex of the parents, the hybrid always generates a mixing colour of its ancestors. Macroscopically, the LPS has blue and cyan scales (Figure 5.1A), BPS has predominantly green and yellow scales (Figure 5.1B), while their offspring HPS has green scales (Figure 5.1C). These three differently coloured *P. sarcitis* weevils have similar body sizes (length of the abdomen: 1.2 -1.5 cm; width of the abdomen: 1.0-1.2 cm; height of the abdomen: 0.8-1.0 cm) exhibit coloured patches, and each pit is covered with many plate-like scales with a similar radius of 36- 38 μm.

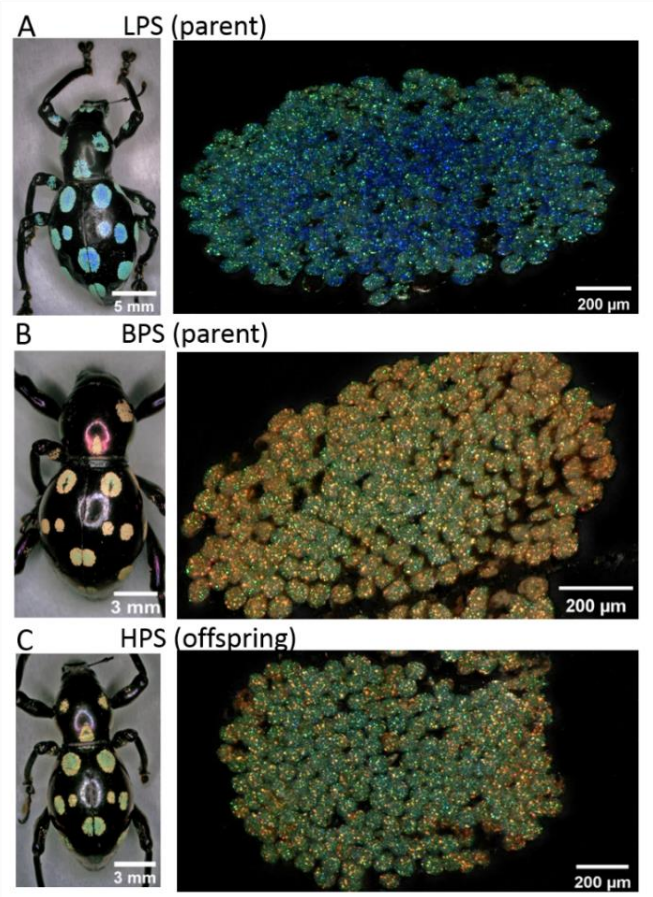

Figure 5.1 Three *Pachyrhynchus sarcitis* (*P. sarcitis*) used in this study and the enlarged image of a single pit of each weevil. (A) Lanyu *P. sarcitis*, (B) Babuyan *P. sarcitis* are captive species. (C) Hybrid *P. sarcitis* is the filial generation of LPS and BPS. For all three weevils, each pit is covered by many small scales.

5.3.2 Optical spectroscopy of domains in a single scale

In the epi-illumination microscope pictures reported in Figure 5.2A-C, I observed that for all three weevils, every scale shows differently coloured domains with colours spread the entire range of visible spectra. To quantitatively correlate how such domains cumulatively contribute to the overall optical appearance, we measured: (i) the reflection spectrum of every single domain in several areas for all three weevils (Figure 5.2D-F), and (ii) their abundance in every scale.

The reflectance spectrum of every differently coloured domain was measured in an area of few μm. Representative spectra of domains from blue (460 nm) to red (640 nm) have been observed in all three weevils. The full width at half maximum (FWHM) of the spectra can vary from 30 to 100 nm and are wider for red-shifted peaks. We noticed that the intensity of the peak varies in different weevils depending on the spectral region: as an example, cyan and green are the most intensely reflected colours in LPS. While in BPS, all the reflected colours have a comparable reflectance, and the HPS exhibits a higher reflectance of green and yellow.

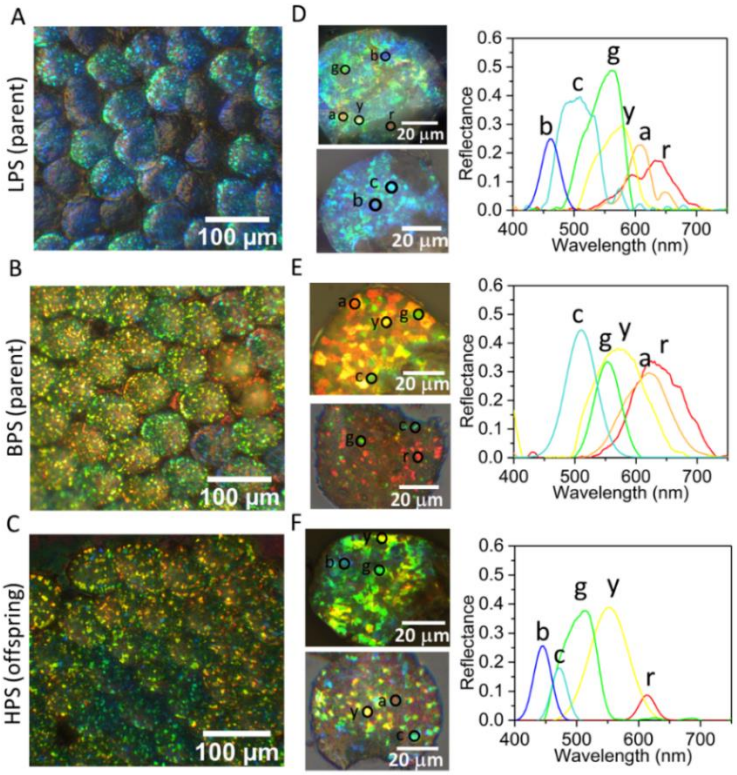

Figure 5.2 Differently coloured domains within scales and representative reflected spectra of each domain colour in three weevils. (A-C) Domains with different colours and brightness can be recognized in each scale of all three weevils. (D-F) Representative scales in three weevils, and the corresponding representative spectra from differently coloured domains in scales of LPS, BPS and HPS. Visual colour for each domain is labelled with b: blue, c: cyan, g: green, y: yellow, a: amber, r: red. Quantitative properties of spectra are listed in Table 5.1.

To complement possible selections of spots with the micro spectrometry study, I used ImageJ RGB analysis (http://rsb.info.nih.gov/ij/) to quantify the distribution of the coloured domains in each scale and in each weevil. The results are presented as the histograms in Figure 5.3.

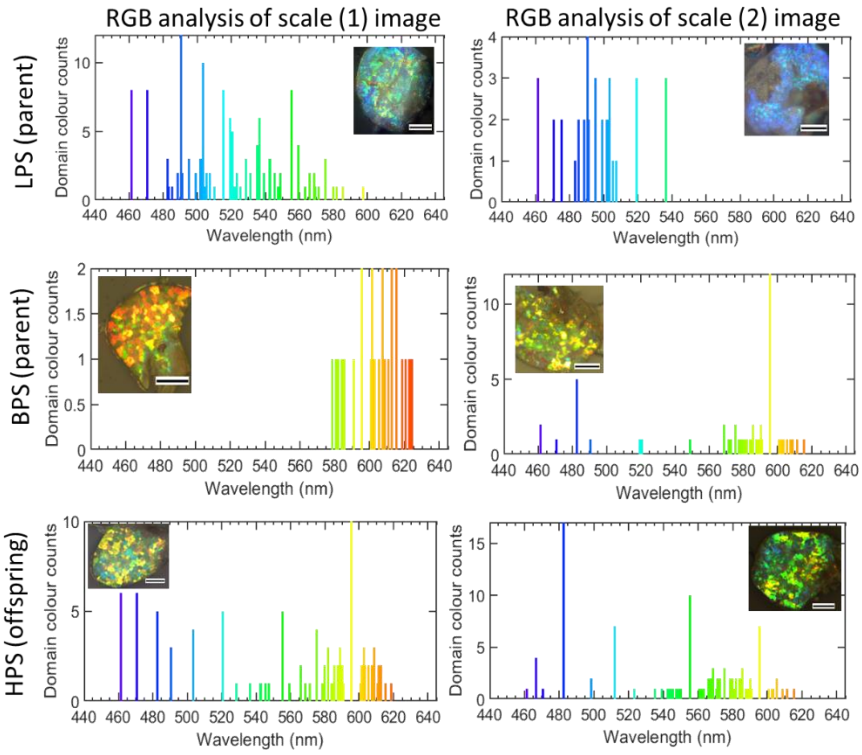

Figure 5.3 Overview of the measured histograms and scales of three weevils. The images of the individual scales and domain colour distribution in each scale are provided. The scale bars are 20 μm. The bin size in the histograms is 20 nm. Blue, yellow, and green is dominated colours in LPS, BPS, and HPS, respectively.

The imageJ RGB program calculates the RGB values of each pixel in an image. The colour counts shown in Figure 5.3 mean the numbers of pixels of such colour in the image. Images subjected to this RGB analyses are controlled with the resolution of 100 nm/ pixel. Sales were scraped off from the elytra and separated, so only one scale was placed on a glass and imaged for each RGB analysis. Therefore, the colour counts in

Figure 5.3 represent the area of specific colours in one scale. The histograms mean the distributions of certain colours in a scale.

LPS has the most (61.3%) blue to cyan coloured domains (~480- 520 nm), and 24.7% green coloured domains. BPS has 31.6% yellow domains (~600 nm) and 23.5 % amber coloured domains (>620 nm), which are the two dominated domain colours. HPS has more equally distributed domain colours that is 14.5 % blue (490 nm), 12% bright blue (507.5 nm), 12.9% blue-green (547.5 nm), 13.4% green (567.5 nm), 11.8% yellow (587.5 nm), and 13.4% amber (607.5 nm) domains. The spectra properties and the coverage of each differently coloured domain across scales are provided in Table 5.1

Table 5.1 Domain visual colours and spectrum properties: wavelength, full width at half maximum (FWHM), and reflectance. The colour coverage is a statistic result from the image-J RGB analysis with a bin size of 20 nm of the wavelength.

Species	Visual Colour	Wavelength (nm)	FWHM (nm)	Reflectance	Colour coverage (%)
Lanyu (LPS)	red	624.5	86.2	0.2	0
	orange	606.6	45.0	0.2	0.4
	yellow	565.1	69.7	0.3	2.6
	green	549.9	64.3	0.5	24.7
	cyan	505.1	66.3	0.4	41.0
	blue	461.7	35.9	0.3	31.3
Babuyan (BPS)	red	624.5	93.5	0.3	31.9
	orange	606.6	87.6	0.3	34.8
	yellow	565.1	94.5	0.4	13.4
	green	549.9	51.6	0.4	3.8
	cyan	505.1	58.2	0.4	16.1
Hybrid (HPS)	orange	613.8	30.6	0.1	21.0
	yellow	553.9	73.2	0.4	25.3
	green	507.6	67.2	0.4	32.3
	cyan	471.9	30.4	0.2	14.5
	blue	445.0	33.3	0.3	6.9

Importantly, both the reflectance of the domains and the distribution of differently coloured domains affect the visual appearance of three weevils. Those colours and domains with higher reflectance look visually brighter, which have a good match to the three weevils' optical appearances. For example, in LPS 86% domains are intensely reflected blue and green lead to the visually bright blue appearance of LPS. BPS has 57.1 % bright yellow and amber domains contribute to its yellow appearance. HPS has the most diverse colours and equally distributed coloured-domains. The relatively high reflectivity of green and yellow colours makes HPS have a green-yellow appearance.

5.3.3 Scanning electron microscopy and crystal parameters

Domains with multiple crystal orientations were observed from both top views (Figure 5.4) and cross-sectional views (Figure 5.4), indicating that crystals rotate in three dimensions in the interior of every scale for three weevils. The typical patterns of high-symmetric orientations in the diamond crystal: (100), (110), (111) have been observed in all three weevils (Figure 5.4B-D). As illustrated in Figure 5.4A I estimated the lattice constant a through SEM images of (111), while we measured the strut radius b from cross-sectional SEM images of (110) orientation, as the strut is perpendicular to the observation plane in this direction. The air pore radius R is calculated from the measured strut radius and lattice constant by the structural relation:

$$R = {}^{a}/_{2} - \sqrt{2}b$$

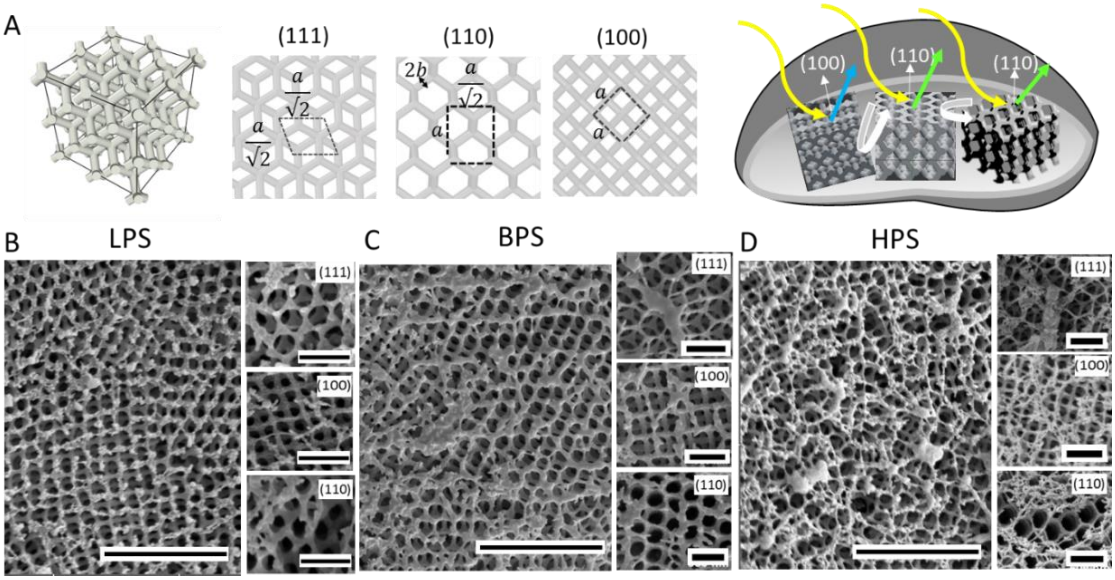

Figure 5.4 Three-dimensional photonic crystals with a single diamond lattice structure (Fd-3m) in three weevils and mapping domain orientations and reflected colour normal to the scale surfaces. (A) Illustrations of a single diamond lattice and its three characteristic orientations: (111), (100), (110). The lattice constant,a, can be calculated from the three characteristic orientations. Different crystal orientations observed in top-view SEM images in three weevils. Scale bars in overview images are 2 μm, and in (111), (100), (110) images are 500 nm.

Quantitative structural information was obtained by sampling over amounts of differently oriented domains within and between scales across different areas of the weevils. The measured average strut radius b, lattice constant a, pore radius R for three weevils are reported in Table 5.2.

Table 5.2 Measured strut radius and lattice constant from SEM images, and the calculated pore radius and the filling fraction of the three weevils. Filling fraction is calculated by dividing the volume of struts by the inner volume of the scale.

	LPS (parent)	BPS (parent)	HPS (offspring)
Strut radius, r (nm)	58.5± 6.5	57.4± 5.9	59.4± 6.2
Lattice constant, a (nm)	412.8± 5.4	438.5± 6.7	443.9± 5.4
Pore radius, R (calculated)	123.7± 9.6	138.1± 9.0	137.9± 9.2
Filling fraction	0.3± 0.1	0.3± 0.1	0.3± 0.1

These lattice parameters are averaged values of many differently oriented domains, the small deviations of both strut radii and lattice constants refer that these values do not differ with different orientations.

It is interesting to highlight that all three weevils have similar strut radii of 57-59 nm. The LPS weevils have the averaged lattice constant $a = 413 \pm 5\ nm$, which is about 30 nm smaller than the other two weevils. BPS and HPS have similar values of the average lattice constant $a = 439 \pm 7\ nm$ and $a = 444 \pm 5\ nm$, respectively. Because the air pore radius R is calculated from the strut radius and lattice constant, LPS weevils, possessing the same strut radius but much smaller lattice constant than BPS and HPS, have smaller calculated pore radius. The R/a of three weevils are very close for around 0.3 because their strut radii are all three times smaller than their lattice constant. I also observed from the equation that in $R/a = 1/2 - \sqrt{2}b/a$ the value of R/a will not be significantly affected by the small value of b/a.

Choice of the diamond-symmetric models

Four possible diamond-symmetric models with different connections between every two lattice points have been reported in weevil scales in the literature [63,107,156,205]. The unit cells of four possible diamond-symmetric models are shown in Figure 5.5A: inverse air sphere (InvSphere), rod-connected (RCD), inverse rod-connected model (InvRCD), and diamond minimum surface (MinSurf). I calculated the theoretical filling fraction (FF) and pore sizes (R) of three weevils based on four models.

To quantify and compare the structural differences between those possible models, each type of model with a various ratio of pore radius and lattice constant (R/a) has been constructed. FF with the corresponding R/a of each model with the four types have

been calculated and the numerical fitting curves of the four models and equations are provided in Figure 5.5B. The different connections can greatly affect the FF. It is interesting that FF in the minimum surface model is the highest among others when R/a is higher than ~0.25, because most insects have been reported possess FF in the range of 0.25- 0.6.

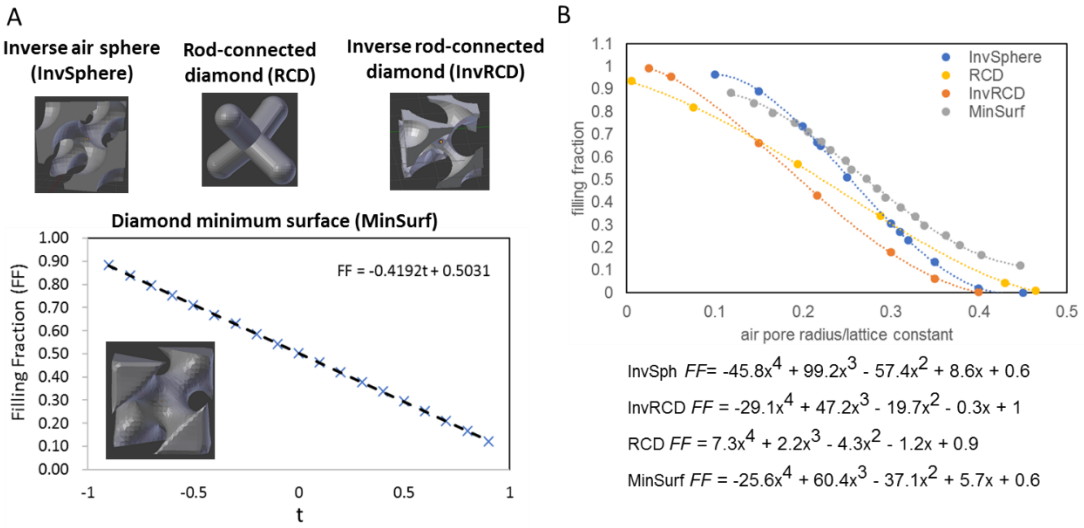

Figure 5.5 Four diamond-symmetric models: inverse air sphere (InvSphere), rod-connected (RCD), inverse rod-connected model (InvRCD), and the diamond minimum surface (MinSurf) proposed in literature to describe photonic crystals in weevils' scales. (A) 3D representation of the unit cells of the different models. Numerically extrapolated equation of FF vs parameter t for the diamond minimum surface model: models with different values of t are constructed and their FF are calculated in Blender. (B) The different connectivity between lattice points results in very different FF, which is reported as function of R/a for the four models investigated.

Table 5.3 shows the calculated FF based on numerical equations of the four models with experimental measured b and a of three weevils. I surprisingly found that different diamond-symmetric lattice configurations can result in large variations of FF in three weevils especially for BPS which can vary from 0.1 to 0.4.

Table 5.3 Calculated volumetric filling fraction (FF) of cuticular proteins in a scale of three weevils based on the four different simulation models: inverse air

sphere (InvSphere), rod-connected (RCD), inverse rod-connected model (InvRCD), and the diamond minimum surface (MinSurf). Three weevils have R/a located in the range of 0.31- 0.32, which based on numerical fitting curves provided in Figure 5.5 predict the highest FF of minimum surface models.

	LPS	BPS	HPS
FF (InvSphere)	0.3	0.2	0.3
FF (RCD)	0.3	0.3	0.3
FF (InvRCD)	0.2	0.1	0.2
FF (MinSurface)	0.4	0.4	0.4

Domain Identification

I characterized the orientation of each domain facing the upper side of the scales by mapping the pattern from cross-sectional SEM images. Domains with the same surface orientation normal in top view can still display different cross-sectional patterns depending on the directions of the surface cut. As illustrated in Figure 5.6A, the three different cutting directions 1, 2, and 3 on the domain with the surface normal to the (110) direction can display a series of cross-sectional patterns. Therefore, to correctly assign the domain, a set of possible cross-sectional patterns were computed for cross-sectional planes oriented every 5^{o}.

It should be noticed that here in this work, I was finding the surface normal on z-axis from the morphologies in x-y planes. Although one can expect many different morphologies are possibly appear in x-y planes with one surface normal on z-axis, those morphologies will follow the symmetry of the cubic lattice. For example, the datasets of three high-symmetric orientations are shown in Figure 5.6A. For the 3-fold axis (111) on z-axis, the patterns on the x-y plane of 0^{o} -60^{o} are recorded to represent all possible

patterns. For the 2-fold axis (110) patterns of 0^o -90^o are recorded; for the 4 fold axis (100) patterns of 0^o -45^o are recorded.

The way to characterize low-symmetry axis from patterns are trivial because one can expect different patterns are possibly generated through the full rotation angles from 0^o -180^o. The first step is to compare the pattern with the high-symmetric one by calculating the distance of the three neighbouring atoms. For example, the distance of three neighbouring atoms in (411) in the Figure 5.6B Lanyu *P. sarcitis* (LPS) is: 1: 1.41:1.70 which is similar to the distances measured from (110). By rotating the guessing plane, i.e. (110) in this case, with fine increments of rotating angles along the direction of (111) and (210) in the open source software OVITO (https://www.ovito.org/docs/current/), I observed the neighbouring distances getting closer to the values of targeted pattern when rotating from (110) to (111). Finally, the plane was found by manually mapping the patterns in the software.

67 domains from different parts of three LPS scales, 79 domains from different parts of four BPS scales, and 60 domains from different parts of three HPS scales were characterized with the surface normal. The amounts, widths, and lengths of every differently oriented domain were measured. Statistical results are provided in Table 5.4.

In general, I observed that all three weevils have scales thickness of 2-3 μm, and differently oriented domains in the same weevil are with similar dimensions. In LPS, 65 out of the 67 domains range between 1.5 to 2.5 μm in width. In BPS, 77 out of 79 domain ranges between 2.5 and 3.5 μm in width, while HPS has more varied domain widths that range from 1.5 to 3.5 μm. Additionally, we observe that: (i) LPS has a smaller average domain size than BPS and HPS, and possesses many domains connecting both the top and the base of the scale; (ii) at the edges of the scale, domains

that connect the top and the base of the scale can be observed while this is not the case at the centre of the scale.

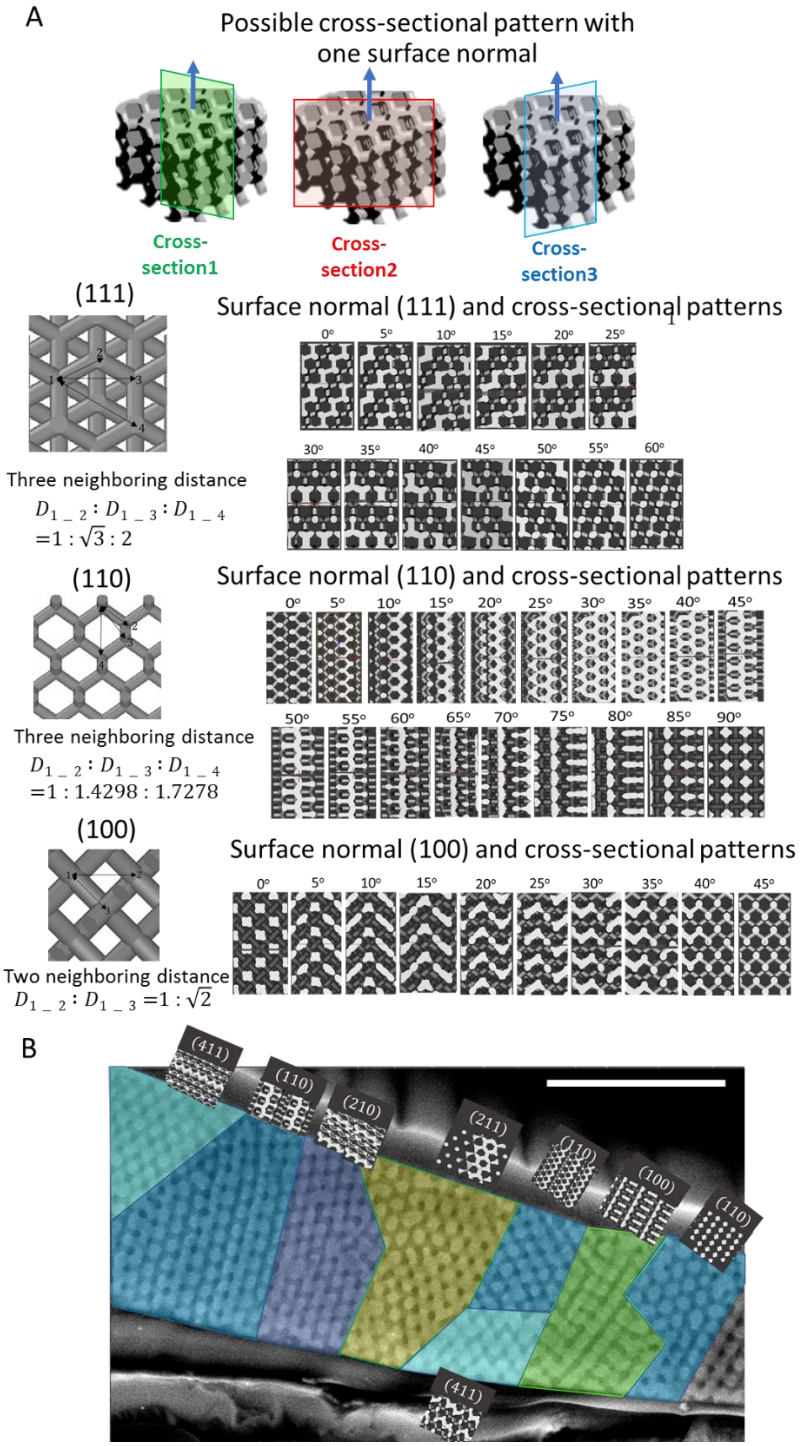

Figure 5.6 (A) Corresponding cross-sectional patterns with a specific plane normal such as (111), (110), (100) faces up to the scale surface. (B) An example image of domain orientations mapping in Lanyu *P. sarcitis* (LPS). Scale bar: 3 μm.

Table 5.4 Amounts of domains and domain geometry of different orientations measured from those connecting to the top surface of the scales based on SEM images. The domain width and thickness of every orientation found in each weevil was provided.

Orientation	LPS (parent)			BPS (parent)			HPS (offspring)		
	Domain (counts)	Width (μm)	Thickness (μm)	Domain (counts)	Width (μm)	Thickness (μm)	Domain (counts)	Width (μm)	Thickness (μm)
100	7	2.0± 0.6	2.5± 0.7	6	2.7± 0.9	2.4± 1.3	8	2.8±0.9	2.2±0.5
411	7	2.2± 0.9	2.6± 0.9	9	2.3± 0.9	3.0± 1.1	9	1.8±0.3	2.9±0.6
111	6	2.1± 1.4	3.5± 1.0	13	2.9± 0.8	3.1± 1.3	8	2.8±1.0	2.2±0.9
210	13	1.9±1.6	2.7±0.7	4	2.8± 0.5	2.2± 0.7	9	2.6±0.9	2.3±1.0
211	9	2.7±1.1	1.9±0.6	16	3.1± 1.1	3.2± 1.2	2	1.5±0.6	2.2±1.2
110	21	2.2±1.4	2.0±0.7	16	2.3± 1.0	2.9± 1.1	12	3.0±1.1	2.3±1.1
123	1	2.6	1.7	6	2.8± 0.5	2.7± 1.3	6	3.6±1.2	1.8±0.3
311	1	1.3	2.3	3	3.0± 0.2	3.2± 0.4	1	2.4	1.9
310	2	4.8±0.1	1.9±0.3	1	2.5	1.2	-	-	-
332	-	-	-	1	2.4	5.2	-	-	-
331	-	-	-	2	1.7± 0.6	3.4± 1.0	-	-	-
431	-	-	-	1	2.7	1.7	2	3.10	2.2
235	-	-	-	-	-	-	1	2.5	2.6
145	-	-	-	-	-	-	1	7.2	4.5
125	-	-	-	-	-	-	1	3.2	3.7

5.3.4 Theoretical modelling of colours of domains

I compared the spectra predicted by MPB with infinitely big model and FDTD with the real domain size with experimentally measured spectra. I used MPB to calculate the first five energy bands along high-symmetric orientations in diamond-based crystals. The reflected wavelength $\lambda_{mid,U}$ and the FWHM of spectra can be derived from the band diagram by the following equations:

$$\omega_{mid,U} = \frac{band3 + band2}{2}$$

$$\lambda_{mid,U} = \frac{lattice\ constant}{\omega_{mid,U}}$$

$$\Delta\lambda_{mid,U}\ (FWHM) = \frac{lattice\ constant}{band2} - \frac{lattice\ constant}{band3}$$

MPB calculated reflected colours of five main orientations in diamond minimum surface models with different lattice constants in three weevils are presented in Figure 5.7A. In general, bigger the lattice constant redder the reflected colours, so LPS with the averaged lattice constant 30 nm smaller than the other two is the only one able to generate blue colours at (210), (110), and (411). BPS and HPS having almost the same lattice parameters generate similar band diagram so does the predicted colours. (111) is the orientation producing the most red-shifted colours. From Figure 5.7A we observed the MPB predicted colours never match the broad spectra possibly generated from domains in each weevil. Also, the MPB predicted spectra are always with FWHM much narrower than the experimental spectra. These mismatches can possibly result from the assumption of infinitely big crystals by ignoring the shape effects.

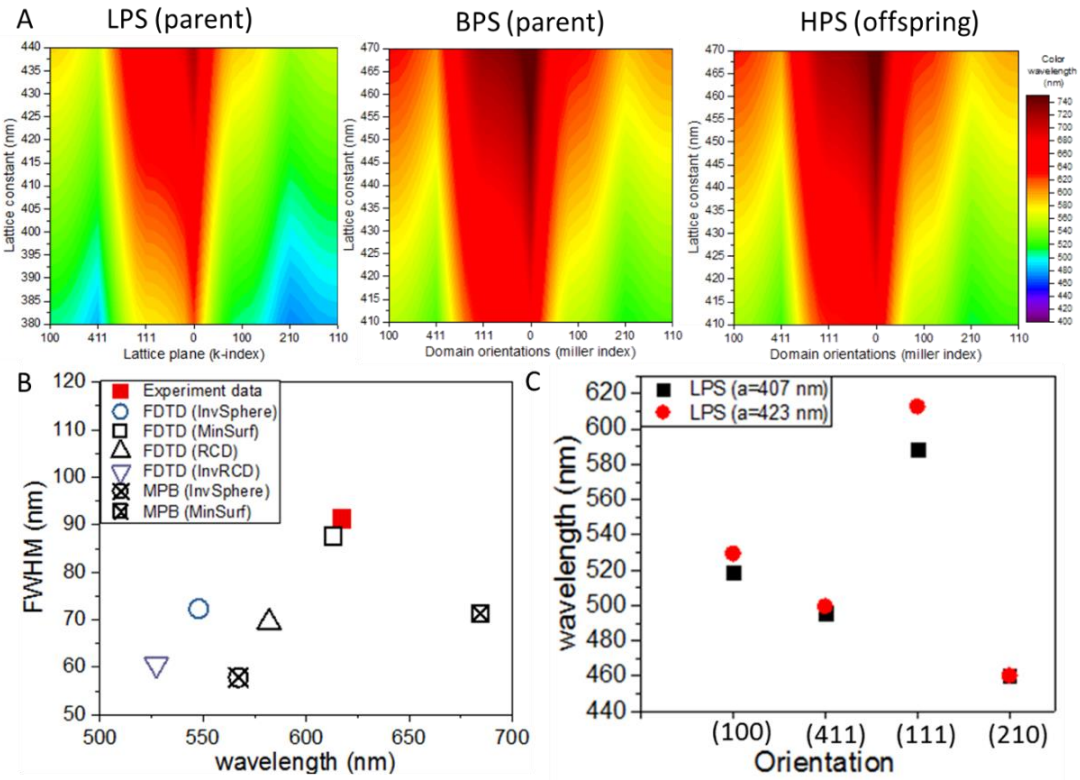

Figure 5.7 MPB calculated reflected colours from three weevils and the comparisons of experimental and FDTD data. (A) I calculated the colours based on the experimentally measured lattice constant (average value ± 30 nm). (B) The experimental measured the reddest spectrum in BPS and the spectral properties of (111) of different diamond-symmetric models calculated by MPB and FDTD. (C) Reflected colours from different orientations in LPS. The influence of uncertainty of the lattice constant (~20 nm) on the reflected colour is small.

I compared the spectra predicted by MPB with infinitely big model and FDTD with real domain sized model of (111) in BPS weevils' scales. Moreover, four possible diamond-symmetric models based on the parameters of BPS weevils were all computed. Figure 5.7B shows the comparisons of experimentally measured spectra of (111) in BPS with computational results from four different crystal models and numerical calculations methods. I observed that: (i) MPB predicts spectra are red-shifted concerning those obtained by FDTD (ii) MPB spectra have smaller FWHM than for FDTD spectra. This latter observation can be explained by the fact that MPB assumes an infinite structure, while finite boundaries matched to measured domain size are considered in the FDTD models.

MPB can provide an efficient way to calculate band diagrams of structures and predict all possible colours reflected from the structures by calculating at frequency domain. However, structural models are assumed infinitely periodic in three dimensions for being Fourier transformed from real space to reciprocal space. As the domain sizes strongly affect the spectral properties, we decided to use FDTD with the experimentally measured domain thickness, filling fraction, and lattice constant. The FDTD calculated spectra of minimum surface diamond crystals are in very good agreements with the experimentally measured domain spectra for all three weevils.

In addition, I have shown very different colours are predicted by four diamond-based lattices models. This result reflects that the connectivity of the diamond lattice can greatly affect the predicted colour range, and the diamond minimum surface model is the only one that successfully predicts both the colour wavelength and FWHM of three weevils considered in this study. While this calculation could be a pure exercise as in the previous studies that only one single species is involved [156,209,212,218], it becomes relevant for matching all colours observed for different domains in the three weevils in this study. Here we showed that three weevils with exact the same type of crystal, same domain sizes, same filling fraction differ their colours by lattice constant and orientations. Moreover, the clarification of the diamond lattice with minimum surface models is worth mentioned as they support the hypothesis of the growth mechanism that diamond crystals in *P.sarcitis* are formed by membrane folding into minimum energy surface.

To further clarify the effects of uncertainty of lattice constant on the visual colour of the weevil, I took LPS as an example and use FDTD to calculate spectra from four main orientations (with corresponding domain geometry) with a varied lattice constant of

about 20 nm. The calculation results are plotted in Figure 5.7C. Generally, FDTD results show structures with a larger lattice constant generate more red-shifted spectra of all orientations. However, the shifts of wavelengths differ from orientations, and greater variations have been observed for orientations producing more reddish colours (such as (100) and (111)). While predicted spectra can be different from the uncertainty of 20 nm of the lattice constant, the variations of 2- 24 nm of wavelengths have ignorable effects on the visual colour. Therefore, the errors of 5- 10 nm in our SEM measurements make non-significant effects on the visual colours of three weevils.

I computed FDTD reflection spectra of highly occurred domains. The constructed models and simulation setups were shown in Figure 5.8A. Figure 5.8B shows FDTD calculated spectra of differently oriented domains in three weevils. Each spectrum is coloured based on the experimentally measured visual colour in Figure 5.10. The domain orientations and the corresponding spectral properties calculated by FDTD are listed in Table 5.5 which shows a very good agreement with the spectra properties measured by the optic fibre in Table 5.4.

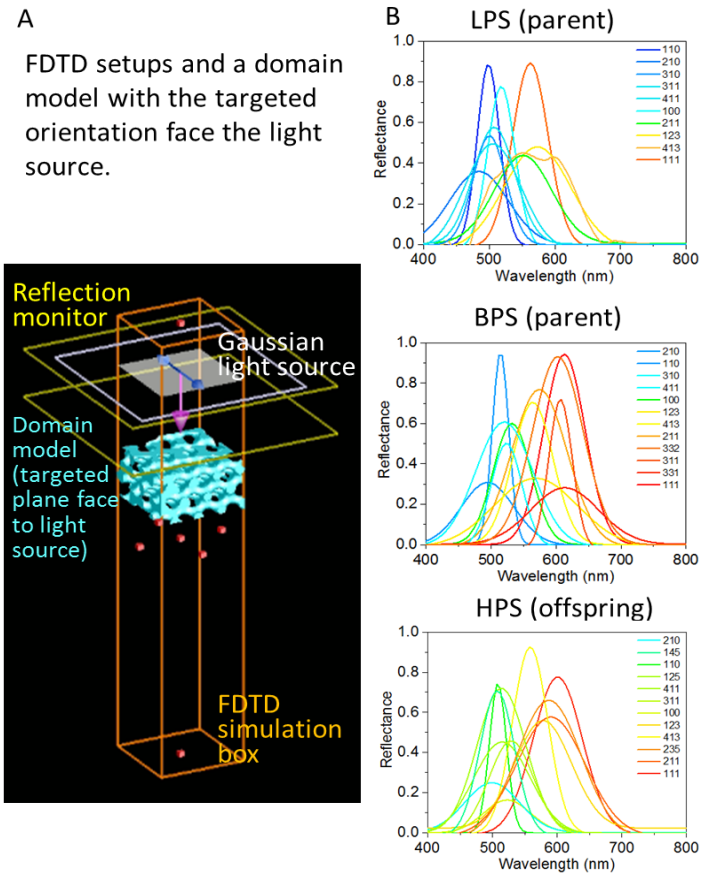

Figure 5.8 (A) FDTD simulation set-up, and (B) the calculated spectra of frequently appeared orientations in three weevils.

Table 5.5 Optical properties including the reflection wavelength, the full width at the half maximum (FWHM), and the reflectance of a spectrum of each domain found in the three weevils.

Orientation	Lanyu (LPS)			Babuyan (BPS)			Hybrid (HPS)		
	Wavelength (nm)	FWHM (nm)	Reflectance	Wavelength (nm)	FWHM (nm)	Reflectance	Wavelength (nm)	FWHM (nm)	Reflectance
100	518.5	53.7	0.8	547.8	73.0	0.5	535.4	56.1	0.7
411	507.0	78.0	0.6	522.0	81.8	0.6	516.1	99.5	0.8
111	563.0	64.9	0.9	619.2	94.9	0.9	600.4	80.7	0.8
210	492.0	82.5	0.3	502.8	62.8	0.5	498.7	103.9	0.2
211	554.1	95.5	0.4	575.0	90.9	0.9	588.1	129.9	0.6
110	499.0	41.5	0.9	507.7	29.9	0.9	509.0	38.9	0.7
123	573.8	113.0	0.5	568.1	152.9	0.4	577.9	115.3	0.6
311	505.8	95.4	0.5	608.8	51.2	0.8	526.9	79.2	0.5
310	502.6	58.8	0.5	520.5	62.2	0.5	-	-	-
332	-	-	-	604.2	85.5	1.0	-	-	-
331	-	-	-	614.0	123.5	0.3	-	-	-
431	-	-	-	563.2	76.6	0.7	558.4	64.8	0.9
235	-	-	-	-	-	-	585.1	120.2	0.7
145	-	-	-	-	-	-	507.4	60.2	0.7
125	-	-	-	-	-	-	513.5	90.4	0.4

5.3.5 Domain sizes and shape effects on visual colouration

Therefore, to take into account the finite size of the domain in the optical response FDTD calculated spectra with different boundary conditions were calculated for different domain sizes. I used the lattice parameters of BPS and construct models with varied dimensions of few μm.

To do so, boundary conditions at x, y dimensions were set while, PML in the z-direction with different unit cells of (100), (110), (111) were considered with varied thickness. Results shown in Figure 5.9A-C reveal thicker domains produce higher reflectance and narrower FWHM. The relationship between the spectral properties and the thickness of the model is non-linear and depends on the crystal orientation. To consider also the limited size of domains in x, y dimensions, we calculated spectra of (111) orientation in the BPS weevil with different domain width, thickness, and with a numerical aperture (NA=0.4) as in the experimental condition (Figure 5.9D- F). Figure 5.9D reports the spectra for a domain with a fixed width of 2.3 μm (averaged value based on SEM images) but varied thicknesses from 1- 3.08 μm under light source with NA=0.4. These produce similar conclusions as Figure 5.9C with infinite domain widths that higher reflection and narrower FWHM is produced by thicker domains. Figure 5.9E reports the spectra for a domain with a fixed thickness of 3.08 nm (averaged value based on SEM images) but different widths of 1 μm, 2 μm, and 2.3 μm. Along with the (111) orientation, both the reflectance and FWHM of spectra increase with the width of domains. It is interesting to observe that FWHM of one spectrum is broader with increasing domain width but decreasing domain thickness.

Even if I considered the limited domain size and the aperture of the microscope objective used to measure the reflection, the calculated spectra still have a higher

intensity than the experimental spectra. I addressed this point by considering a certain amount of disorder in the structure. In fact, all the results presented above are based on the assumption of a perfect crystalline structure, while in the SEM images a non-negligible amount of disorder in the real architecture can be observed, both in terms of their lattice constant (deviation of 5.4-6.7 nm), strut radius (deviation of 5.9-6.5 nm), and filling fraction (deviation of 0.1). Such role of disorder in the optical response is therefore estimated by weighting the probability results from the variation of the mentioned structural parameters. Figure 5.9F shows that the presence of disorder can decrease the intensity of the peak and increase its FWHM. I assumed that the residual differences between theory and experiments can be attributed to additional sources of disorders such as irregular crystal geometry that cannot be easily captured by 2D imaging techniques.

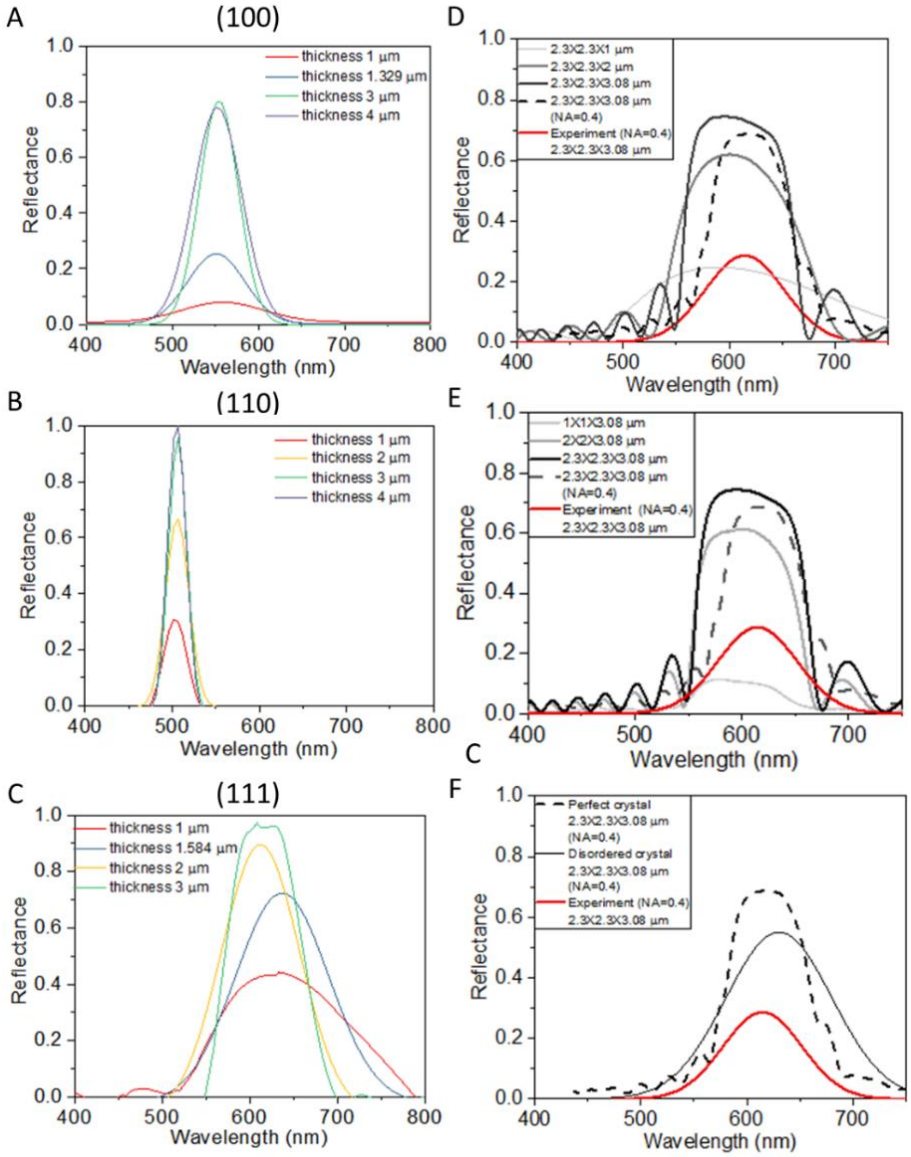

Figure 5.9 FDTD simulated spectra of (A) (100), (B) (110), (C) (111) with different domain thickness (1-4 μm) and experimentally measured domain thickness. (D-F) The spectra reflectance and FWHM change non-linearily with domain geometries, applied light source, and disorder. Spectra of (111) in BPS with varied domain width (D), domain thickness (E), applied with plane-wave light source, or with NA of 0.4 (F). The disorder is incorporated in the calculated spectrum by semi-analytical analysis method, which combines numerically simulated line shape with gaussian fitted peak positions and the uncertainties in experimentally measured strut radius, the lattice constant, and filling fraction.

5.3.6 Domain orientations and visual colour appearance

I visualized the FDTD calculated results in Figure 5.10A that the surface normal of each domain in the cross-sectional SEM images was characterized and the domain was painted with the calculated colours. I observed different preferred orientations are in three weevils and this preference correlates to the visual appearance of weevils. I plotted the area covered by each oriented domain in three weevils on a stereographic projection as Figure 5.10B-D. In the projections, markers colour correspond to the colour reflected from the specific orientation and the marker size is proportional to the occurrence of the domain. I defined the normal of crystal plane (100) as the centre pole with the horizontal angle Φ and tilting angle ρ of 0^o. For any other crystal planes, the Φ angle will be measured from the pole in a clockwise sense in the equator plane, and ρ angle is measured from vertical direction and downward from the centre pole. Interestingly, we observe different features of the angular relationships of preferred domain orientations in three weevils. The preferred domains orientations in LPS are along 0^o or 45^o of the horizontal angle (Φ) to the crystal face (100) and with decreasing coverage of domains from 45^o to 0^o of the vertical angle (ρ). In BPS, most of the domains are along $\Phi=45^o$ for which the reflected colours are red-shifted. Also, there are more preferred domains along $\rho=45^o$ and domain coverage also decreases from 26.6^o to 0^o of the vertical angle. In contrast, the preferred domain orientations in HPS are more evenly distributed. Our observation of different angular relationships of preferred domain orientations in three weevils can be explained by crystallography and crystal growth mechanisms which therefore strengthens our hypothesis that three weevils adjust their living colours by tuning preferred orientations.

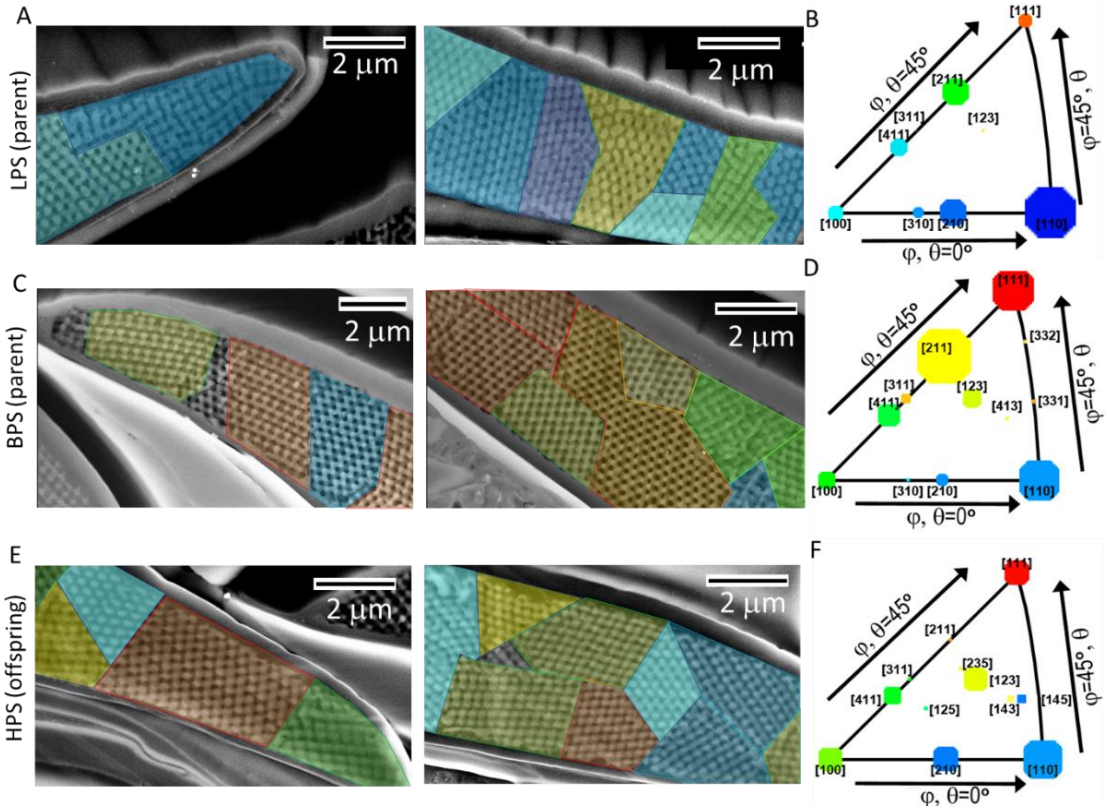

Figure 5.10 Differently oriented domains in three weevils coloured by the FDTD calculated colour of the domain in (A) LPS (C) BPS and (E) HPS. In (B, D, F) we illustrate the preferred domain orientations in LPS, BPS, and HPS, respectively on stereographic projection with the marker size proportional to the domain occurrence and the marker colour the same as the reflected colour

The histograms of colours from the RGB image analysis with the histograms of the domain orientations multiplied by the average lateral size of the domains in Figure 5.11. The histograms derived from the two methods show similar distributions of colours and explain the visual appearance of three weevils. For example, LPS has large domain areas of (210) with wavelength 460 nm, (211) with wavelength 465 nm, and (110) with wavelength 472 nm which produce visual colours from blue and cyan. In BPS scales, (211), (111), (110) are the three orientations covering a larger area, and they reflect yellow (575 nm), red (619 nm), and cyan (508 nm) contributing to the majority yellow and some bluish colours. Finally, HPS has more uniformly distributed domain orientations and has more (110) which reflects green colours, so we confirm that the

preferred orientations and bigger domain size in each weevil contribute to their overall colour.

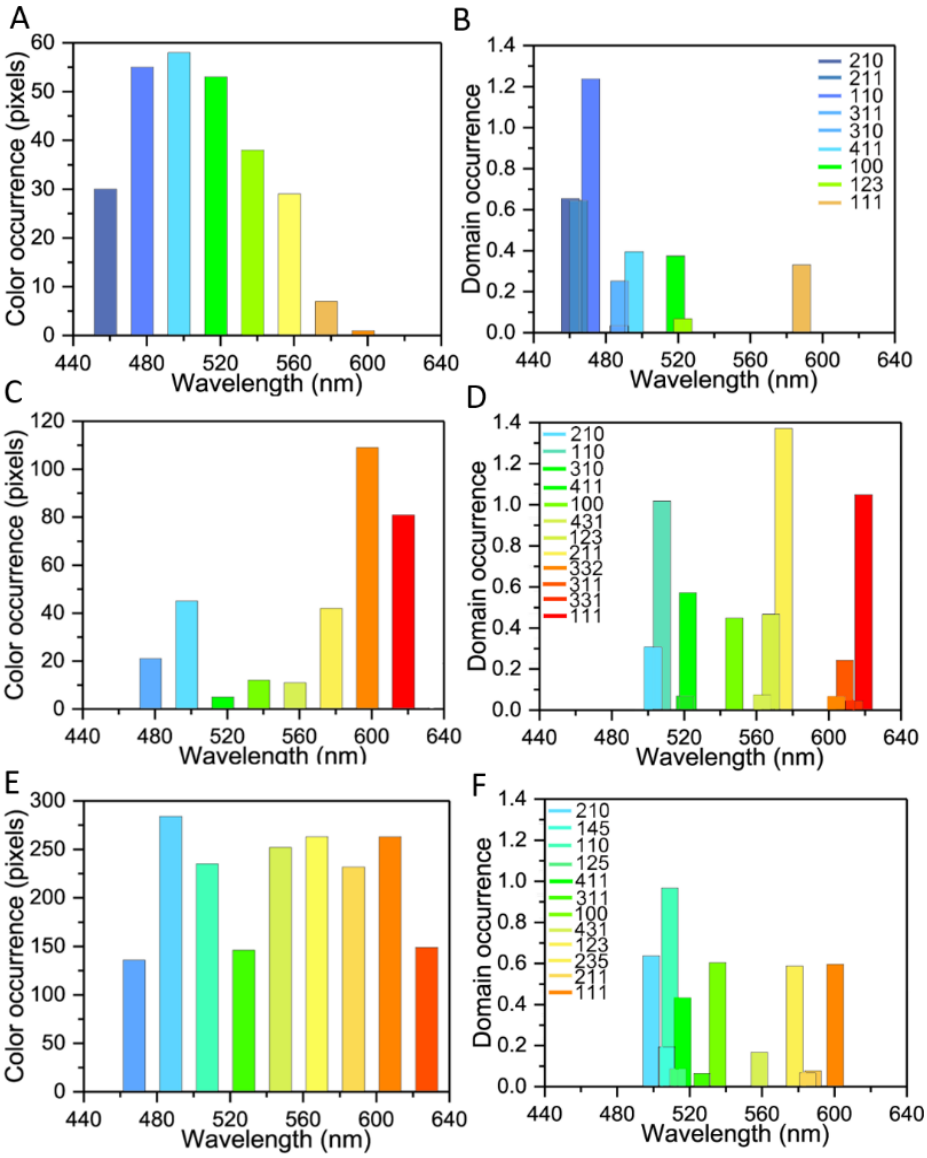

Figure 5.11 Comparison of colour occurrence derived by RGB colour analyses and domain occurrence derived by structure analyses. (A, C, E) show the colour histograms reporting the distribution of colour on the scales of (A) LPS, (C) BPS and (E) HPS. (B, D, F) show the histograms of the area covered by each domain orientation in the scales of (B) LPS, (D) BPS and (F) HPS. The histograms of domains are obtained by multiplying the occurrence of a domain as identified by its average size identified by SEM cross-sections and normalized on the average size of the scale. (Averaged radius of scales of LPS: 38.08± 1.1 μm, BPS:36.42± 0.5 μm, HPS: 37.10± 6.3 μm).

I showed that the macroscopic colour of each weevil is the sum of the contribution of individual domains and that the domain geometry and orientations are determining factors in the different colour appearances of three weevils. LPS having a much smaller lattice constant than BPS and HPS reflects wavelengths in the more bluish colour range. BPS and HPS having almost the same lattice constant, strut radius, filling fraction reflect different colouration and brightness with a different distribution of domains and domain sizes.

5.4 Discussion

The possibility to captive-breed and hybridize different structurally coloured *Pachyrhynchus* weevils allowed me to systematically investigate how photonic structures can be modified from ancestors to descendent. By carefully studying the anatomy of the scales of the three weevils, we observed that the F1 Hybrid *P. sarcitis* (HPS) obtain green colouration by maintaining the lattice constant of its yellow ancestors Babuyan *P. sarcitis* (BPS) and succeeding the domain orientations of both blue Lanyu *P. sarcitis* (LPS) and yellow Babuyan *P. sarcitis* (BPS). Interestingly, these observations remain valid irrespectively of the sex of the parents. Hybrid *P. sarcitis* weevils from blue and yellow parents are always green.

I speculated that changing orientation of domains to tune colours might be more successful than an adjustment of the lattice constant. In this hypothesis, a change of lattice constant will require a re-design of the compositional materials in the cuticles of these photonic crystals. In contrast, crystal domain orientations can be simply changed by different surface properties in the scale interior membrane.

Functions of such structural colours of *Pachyrhynchus* weevils have been fascinating many researchers, and interestingly, crypsis and aposematism have been proposed. The former has often been proposed by physicists who compared the optical appearance of the weevils with the optical features produced in their habitat. On the other hand, aposematism has always been proposed by biologists because many beetles have developed similar structural colours as the local *Pachyrhynchus* weevils. Even though my results cannot explain the functions of any specific colour of the *Pachyrhynchus* weevils, the easiness for them to diverse colours via changing crystal orientations without redesigning the compositions in cuticles might possibly explain their diversity of the appearances across different oceanic Southeast Asia islands.

Chapter 6
Convergent traits of the mimicry pair: *Pachyrhynchus nobilis* and *Doliops similis*

How different species evolved similar traits and appearance has fascinated biology research field since the time of Darwin. A classic example of the Batesian mimicry is the model weevils *Pachyrhynchus nobilis* (Coleoptera: Curculionidae) and the mimic beetles *Doliops similis* (Coleoptera: Cerambycidae). These two species are sympatric but from distantly related lineages.

P. nobilis uses its vivid structural colours and robust exoskeletons to defence. *D. similis* develops a similar appearance of *P. nobilis* to reduce the rate of being hunted. I am curious how these distantly related species develop similar phenotypes, and how similar their traits are for effective aposematic functions. Because the mechanical and optical properties are key features leading to *P. nobilis*'s success on defence, I focused on the comparisons of the morphology and the mechanical properties as well as the behind production mechanisms developed by this mimicry pair.

I acknowledge Dr. Tseng for capturing the *Pachyrhynchus nobilis* and *Doliops similis* in Taiwan and keeping providing us with the samples.

6.1 Introduction

In the evolutionary process, many closely related species show similar phenotypes because they share genetic similarities. Interestingly, some distantly related lineages (i.e. in different taxonomic groups) can also develop convergent traits and showing nearly undistinguishable appearances. Such convergent traits are always developed to benefit species under natural selection. Examples of mimicry pairs have been found in snakes [222,223], frogs [224,225], and insects [14,226–228]. The Batesian mimicry is one type of mimicry patterns that harmless species (mimics) that resemble the appearance of the dangerous ones (models) to deceive predators and avoid the predators' attacks.

As many of these Batesian mimics show imperfect mimicry, one might wonder if the inaccuracy results from a limitation in the capability of the mimics to produce exactly the same phenotypes or not. Several possible hypotheses for imperfect Batesian mimicry have been proposed: (i) genetic variations within mimetic species are not sufficient for evolving perfect mimicry; (ii) the mimics are in the process of evolving towards perfect mimicry. (iii) imperfect mimicry is good enough to maintain mimics survival under relaxed selection [222]; (iv) predators identify the preys by multiple signals such as the preys' behaviours resulting in a relaxed selection on the resemblance of the appearances [229–231]; (v) smaller size of the mimics providing low calories to predators thus lower predators' incentives to attack so that relaxed the selection [232]. Finally, (vi) imperfect mimicry reflects a trade-off between physiological cost or other advantageous functions such as thermoregulation [231].

One of the fantastic cases of mimetic relationship has been found in beetles in Southeast Asia. Several species in different families of Coleoptera such as longhorn beetles (*Doliops* spp. In Cerambycidae) display a similar appearance of *Pachyrhynchus* weevils

(in Curculionidae) living within the same geographical area. Also, one cricket (*Scepastus pachyrhynchoides*) belonged to Orthoptera has taken on the shape and colouration of a species of *Apocyrtus* weevil (in Curculionidae) [233]. Mimetic pairs of longhorn beetles and *Pachyrhynchus* weevils can be found on different islets and featured with diverse convergent appearances by locations [3,233,234].

Pachyrhynchus weevils are renowned as unpalatable to many possible predators because their robust exoskeleton forms a strong protective armour for protecting the important organs and soft tissues inside [234]. Their bright colouration has been proved to provide a secondary defence function that efficiently decreases the predation rate [3]. In contrast with no-flying *Pachyrhynchus* weevils, *Doliops* beetles have opened elytra and can unfold their hindwing and fly. Importantly, such opened elytra cause *Doliops* beetles have a low resistance to predators' attacks. This limitation in mechanical response is however compensated by the fact that *Doliops* resembled the appearance of *Pachyrhynchus* weevils, cheating the predators in considering them as hard to eat as the *Pachyrhynchus* ones [214,215,233,235].

Here, we investigated the performance of the models *Pachyrhynchus nobilis* and the mimics *Doliops similis* in terms of optical responses and mechanical properties to quantitively estimate the degree of perfection in mimicry.

6.2 Materials and Methods

6.2.1 Sample Preparations

Adult *Pachyrhynchus nobilis* and *Doliops similis* beetles were collected by my collaborators Dr. Hui-Yun Tseng's group from Lanyu Island (22°4'44.57"N,

121°33’15.25”E) in Taiwan. Dry samples were obtained from fresh adult beetles immersed in 70% ethanol and desiccated at room temperature before tests.

6.2.2 Optical microscopy and image analysis

Optical microscopy with a 5X EPI objective (Zeiss, NA=0.9), or 50X SLWD objective (Nikon, NA=0.4) were used. Spectra were collected *via* optical fibre. Spectra detected in the bright field were normalized with a silver mirror (Thorlabs, PF10-03-P01). Spectra detected in the dark field were normalized with a white diffuser. Readers are referred to Chapter 3 for detailed setups.

6.2.3 Compression tests and puncture tests

The intact beetles were firmly fixed on glass slides and subsequently tested using a 5 cm diameter compression clamps equipped on a ProLine universal testing machine (Zwick/Roell, Germany), and the force was measured by a 200 N load cell. The loading rate of 0.001 mm/s was applied for characterizing mechanical properties under static conditions. The contact region of the clamps and samples was checked on the isolated elytra (without contacting the head, thorax, or legs of the beetles). Three *P. nobilis* and two *D. similis* intact beetles were compressed.

Since the results of puncture tests strongly depend on the way they are measured, I built completely the same setup of puncture test as described by Sanson et al. [236,237] to ensure my measurements on the mimicry pair are under comparable conditions as their measurements on many sclerotized and non-sclerotized insects’ wings and elytra. The detail setups include (1) applying forces on a fixed sample by moving a 0.7 mm diameter flat-ended pin (area 0.385 mm^2) with displacement controlled rate at 0.3 mm/s., (2) a clamp device composed of two acrylic bulks with a 2 x 2 mm^2 hole at the centre of each bulk. A fragment of the elytron was placed at the centre and in between the two

acrylic bulks, and the two acrylic bulks were then tightened together by four screws at the four corners of the bulks. Puncture tests were conducted on the ProLine universal testing machines. Eight relatively flat fragments cut from the elytra of each beetle have been subjected to the puncture test. Data of four successfully punctured samples (fractured at the centre of the specimen) were used for analysing the puncture stress (N m^{-2}) and work to puncture (J m^{-2}).

6.2.4 Nanoindentation

Nanoindentation tests were conducted at room temperature in ambient air. The samples were firmly fixed to the Hysitron nanoindenter (TriboScope, Hysitron) stage with magnets. Indentation tests were performed using a three-sided Berkovich tip. Each indent was completed by loading to a maximum displacement of 600 nm in 10 seconds, followed by 10 seconds creep time, and finally unloading to zero force in 10 seconds. The modulus of each indent was calculated through Oliver-Pharr method. Three samples were measured for each species with more than 20 tests per sample. All tests were at room temperature, and the samples were firmly fixed to the holder.

6.2.5 AFM-IR

Local IR spectra were recorded with an Anasys NanoIR2 instrument. For analysis with the AFM-IR, the beetle elytra and its scales were ethanol-dried and embedded in LR White hard resin (Agar Scientific, UK). The embedded material was then transversely microtomed to produce slices with a thickness of 300 nm. Thin slices were collected on a 1x1 cm^2 glass and the glass was fixed on a small magnetic plate for stably attaching with the AFM-IR sample stage.

6.3 Results

6.3.1 Microstructures and mechanical properties of elytra

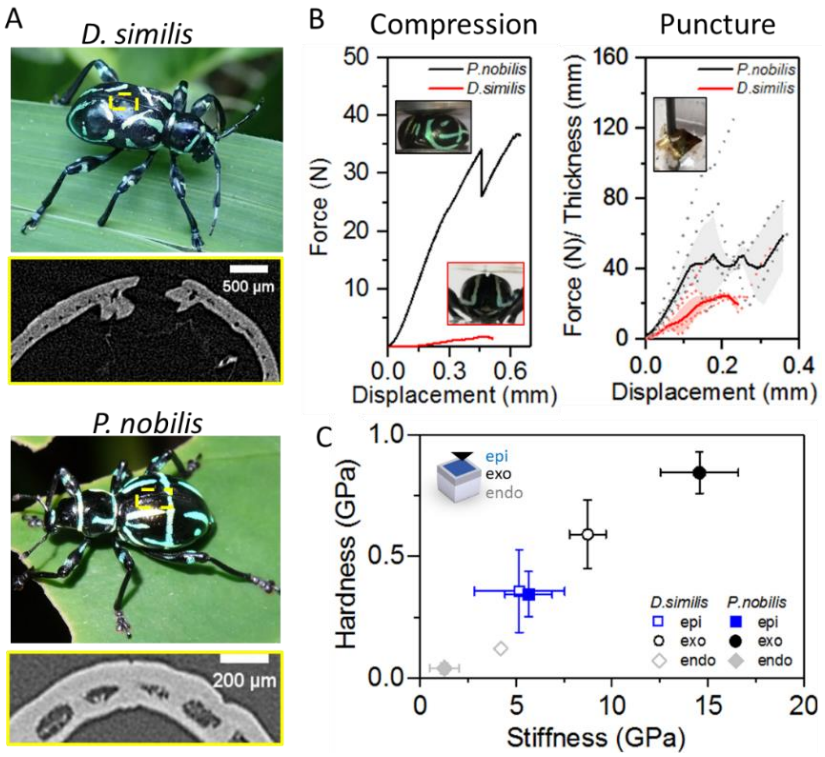

Figure 6.1 Microtomography of the interlock structures of elytra and mechanical properties of the Batesian mimics *Doliops similis* and Batesian models *Pachyrhynchus nobilis.* (A) Computed tomography at the fused line of elytra (yellow square) shows the elytra are opened in *D. similis* and fully fused in *P. nobilis*. (B) Force-displacement curves for compressing to break the two species (left panel) and for penetrating their elytron (right panel). *P. nobilis* (black line) can endure higher compression force and its elytra are with higher tolerance to punch force than *D. similis* (red line). (C) Nanoindentation tested stiffness and hardness of different cuticles in elytra of two species. Note: because the epicuticle is extremely thin (~ 100 nm), the mechanical results of epicuticle is a combination of epicuticle and some underneath exocuticle.

Adult *D. similis* beetles have many macroscopic resemblances to *P. nobilis* weevils including their body size (length of 1.2- 1.5 cm and width of 0.5 cm), the dome-shaped abdomen with a big hollow space in the centre, and finally the distribution of the green stripes on black exoskeletons.

The major difference between the two species is the interlocking of elytra (Figure 6.1A).

D. similis usually keeps its elytra loosely interlocked when not flying, and it can use the scutellum to actuate the wings stroke, open elytra, and unfold the hindwings to fly. *P. nobilis*, on the other hand, lost the fly ability because their elytra are fully fused and their hindwing and scutellum are reduced. By recording the stress and strain responses of two beetles under a compression load (Figure 6.1B), I found the fused elytra and the round body shape enable *P. nobilis* to endure higher compression force (35 N for initiating cracks and 37- 40 N for fracturing) than *D. similis* (2N for fracturing) as shown in. The measurement consistently shows that the resistance of the compression force of *P. nobilis* is slightly higher when compared to the local predators' bite force of about 20 N [234], ensuring *P.nobilis*'s survival under attack. Moreover, the stiffness of every single elytron of *P. nobilis* is higher (as normalized force-displacement curves shown in Figure 6.1B) and tougher (work to punch: 5.3±1.69 x10^3 J m^{-2}) than the single elytron of *D. similis* (work to punch: 1.8±0.86 x10^3 J m^{-2}).

For both species, the elytra are composed of three differently structured regions: the epicuticle, the exocuticle, and the endocuticle. The epicuticle is the outermost layer made from waxy lipo-proteins without contribution to the mechanical strength of the entire cuticle [238–241]. Underneath the epicuticle is the exocuticle region where the chitin-protein fibres are highly sclerotized.

We used nanoindentation to measure the modulus and hardness of each layer. To avoid detecting anisotropic mechanical strength resulting from differently oriented chitin fibres, we indent each layer from the top-vertical direction. By indenting through the thin epicuticle, similar stiffness (4 GPa) and hardness (0.3 GPa) are observed of the two species. The exocuticle of *P. nobilis* is stiffer (stiffness: 14.5±2 GPa) and harder (hardness: 0.8±0.09 GPa) than the one of *D. similis* (stiffness: 8.7±0.9 GPa; hardness:

0.6±0.14 GPa). The endocuticle, which is the thickest region in the elytra, is softer than the exocuticle. The stiffness (2-4 GPa) and hardness (0.1 GPa) of endocuticles of *P. nobilis* and *D. similis* are similar. This is expected as the endocuticle is composed of loosely staked, unsclerotized chitin and proteins [242].

The mechanical tests cross nano- to macro-scaled indicate that *P. nobilis* is stronger than *D. similis* in three aspects: (1) stiffer and harder exocuticle, (2) higher resistance to penetration of single elytron, and (3) higher resistance to compression force of the fused elytra. These differences make *D. similis* beetles vulnerable to compression force and therefore undefended to most predators' attacks when compared to *P. nobilis*.

6.3.2 Mechanisms for enhancing mechanical strength

It is worth noticing that this mimicry pair *P. nobilis* and *D. similis* both possess strengthened elytra which is prominent among other sclerotized beetles. Figure 6.2A shows published data on puncture tests data of unsclerotized and sclerotized moths wings and beetles' elytra plotted in function of the maximum force used to penetrate them with their thickness. *P. nobilis* weevils have resistance to puncture stress of 30-50 MPa and *D. similis* have resistance to puncture stress of 10-20 MPa which are extremely high among studied beetles' elytra [237]. We observed *P. nobilis*'s and *D. similis*'s resistances to puncture stress follow the trend line of fully sclerotized insects, while they have outstanding puncture strength mainly because they develop relatively thick elytra. Interestingly, *P.nobilis* has similarly robust elytron with other *Pachyrhynchus* weevils in the Curculionidae family, whereas *D. similis* has relatively robust elytron than the other flyable longhorns in the Cerambycidae family, which show averaged resistance to puncture stress of 1-10 MPa even with very thin elytra.

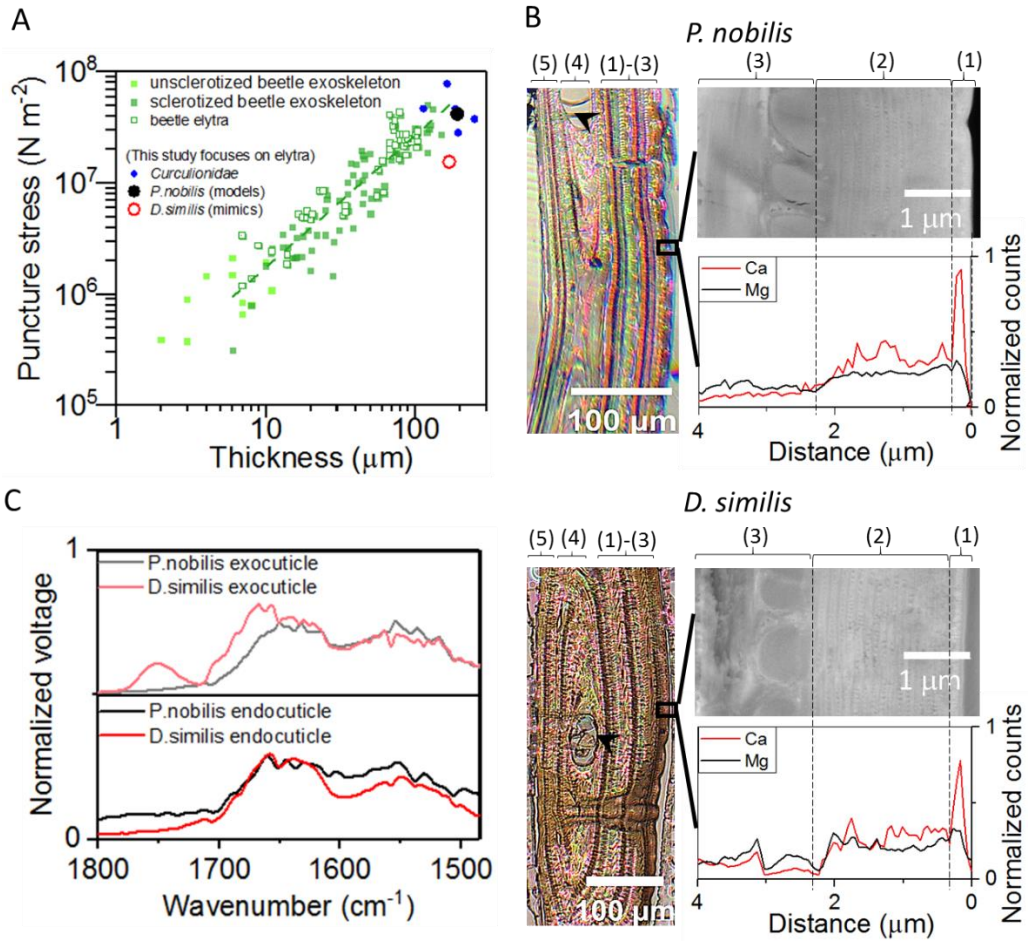

Figure 6.2 Microstructures and components of the elytra of the two species. (A) Puncture strength of the mimicry pair comparing to other unsclerotized or sclerotized wings of insects. (B) Microstructures and EDS mapped metal ions distribution in different cuticle layers in the elytra. Differently structured layers are labelled with numbers: from outside to inside of the beetle is (1) epicuticle, (2) exocuticle, (3) dorsal endocuticle, (4) hemolymph space (hs, as pointed by a black arrowhead), (5) ventral endocuticle. The thickness of each layer is provided in Table 6.1 (C) AFM-IR spectra detected from the exocuticle and endocuticle of *P. nobilis* (black line) and *D. similis* (red line)

Insect cuticle is a structural composite composed of mainly chitin/chitosan, cuticular proteins, some polyphenols [243], lipid, and water [244]. It was proposed the mechanical differences of epi-, exo-, and endo-cuticles arise from different factors: (i) Different interactions between the various components mainly the chitin filament with the protein matrix. (ii) Different crystallinity and orientations of chitin nanofibers that longitudinal modulus of highly crystalline chitin can reach 150 GPa [26,124], (iii) Different levels of

sclerotization (crosslinked proteins) that unsclerotized cuticles are soft with a modulus of 1 kPa- 50 MPa or fully sclerotized cuticles, which can enhance modulus for 100-1000 times of about 1–20 GPa [26,245]. (iv) Presence of metal ions (Ca, Zn, Mn, Fe, Mg) in some thickened and armoured parts of insects (such as in the biting mouthparts) [246–248], that have been as a hardening mechanism for rigidifying insect tissues [26,242,245,249,250].

To resolve the factors contributing to the high mechanical properties of the two beetles and to understand the reasons why *P. nobilis* have higher modulus and hardness of exocuticle and higher tolerance to penetration stress than *D. similis* (Figure 6.2A), I compare the microstructures (Figure 6.2B) and inorganic (Figure 6.2B) and organic phases (Figure 6.2C) in elytra of the mimicry pair. From Figure 6.2B, I observed that the two species show high resemblances not only on the thickness of elytra (>100 μm), which are relatively thicker than most studied beetles (Figure 6.2A) but also on the microstructures of exo- and endo-cuticles (Figure 6.2B and Table 6.1).

Table 6.1 Thickness of different layers (as labelled in Figure 6.2) and structures in the elytra of *Doliops similis* and *Pachyrhynchus nobilis*.

	D. similis	*P. nobilis*
(1) epicuticle (μm)	0.1±0.02	0.1±0.03
(2) exocuticle (μm)	2.0±0.09	2.3±0.06
(3) dorsal endocuticle (μm)	89.8±11.0	95.3±4.8
(4) hemolymph space (μm)	50.8±4.7	47.5±7.3
(5) ventral endocuticle (μm)	24.8±2.3	48.9±5.1
(6) total thickness (μm)	168.4±4.1	190.6±7.3

I used TEM-EDS to map the metal ions in the elytra of two species. The elytra of *P. nobilis* and *D. similis* are both non-mineralized with only few Ca detected in the exocuticles regions (~2 μm) (Figure 6.2B). Therefore, metal ions might not play an important role in hardening cuticles of either *P. nobilis* or *D. similis*.

AFM-IR was used to qualify the organic phases in exocuticles and endocuticles in *P. nobilis* and *D. similis* (Figure 6.2C). The AFM-IR spectra reveal in the elytra of two species the main components are cuticular proteins while more lipid (IR peak at 1750 cm^{-1}) was detected in the exocuticles in *D. similis*.

Based on these measurements, I found the models *P. nobilis* and the mimics *D. similis* show high resemblances in the microstructures and compositions in their elytra. The higher resistance to puncture force and higher modulus and hardness of the *P. nobilis*'s elytra are more possibly associated with higher sclerotized levels.

The thick elytra of *D. similis* while it might serve as robust armour for secondary defence, it comes as a disadvantage for flying due to the increased weight. From Dr. Hui-Yun Tseng's fieldwork experiences, the numbers of *D. similis* are distributed more widely than *P. nobilis*, indicating that their ability to flight might be more valuable than producing a perfect mimicking of the defence strategy of *P. nobilis*. Flying is necessary for species with small numbers of amounts to keep high mobility to increase mating opportunities, to expand the area, and to confront environmental changes. Moreover, it also implies that *D. similis* has developed quite a successful appearance mimicry as the primary defence strategy, so it relaxes the predators' selections on secondary defence.

Anbutsu et. al. found the development of *Pachyrhynchus infernalis*'s elytra is easy to be affected by environmental factors such as bacterial symbiont [251]. It is in fact showing the high phenotypic plasticity on development of elytra because the same bacterial symbionts can be acquired by the mimics through mediating the dietary as the models. Especially the Batesian mimicry pairs are always sympatric, it is therefore not difficult for *D. similis* to innovate physiological conditions through dietary and develop their elytra following the same pathways as the sympatric models *P. nobilis*.

6.3.3 Optical properties at different length-scales

Reflection spectra of the two species reported in Figure 6.3A reveal *P.nobilis* and *D.similis* reflect almost the same green colour with the wavelength of 550 nm, while the reflectance produced by *D.similis* is lower. Similarly, the full width at half maximum (FWHM) of the spectra for *D. similis* is slightly smaller than that of *P.nobilis.* These differences in intensity and width of the spectra imply predators might be able to tell the differences of two species: either in terms of brightness, contrast or colour saturation. In addition, *P.nobilis* produces not only intense green colour from the stripes but also strong UV signals at about 300nm and a more intense gloss of the elytra at the side and tail positions. The different spectral responses in the UV between the two species might also be recognised by the predators.

The differences in colourations produced by *D. similis* and *P. nobilis* are related to their different colour production mechanisms. By measuring the optical responses of the scales of the two species under bright field and dark field (Figure 6.3), I observed that *P. nobilis* generates strong specular reflection colours while *D. similis* produces colours mainly by scattering the incident light.

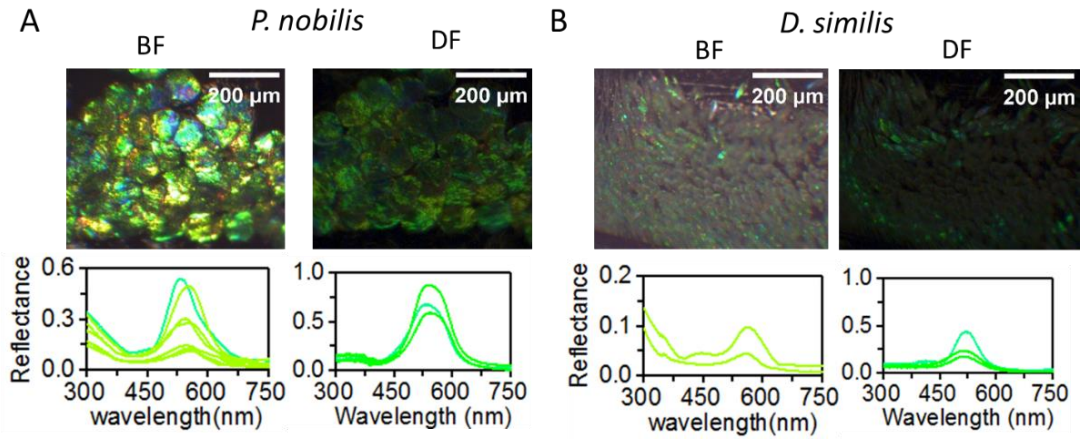

Figure 6.3 Different optical responses produced by the scales of (A) *P. nobilis* and (B) *D. similis* under bright field, BF, or dark field, DF.

Next, I looked into the microstructures and components in their bright scales to study how these two species produce colours. The stripes on these two species are both composed of many micro-sized scales which are plate-like and bigger in *P. nobilis* whereas needle-like in *D. similis* (Figure 6.4A). From the cross-sectional SEM images in Figure 6.4A, various domains (each domain is framed by yellow lines on the SEM images) of differently oriented photonic crystals are within the scales of both species. Photonic crystal structures and reflection spectra from scales of two species are shown in Figure 6.4A. Inside a scale of adult *P. nobilis* and *D. similis,* photonic crystals are made of cuticles and in between the cuticles are *in vivo* air spaces. *P. nobilis* has diamond photonic crystals woven by cuticular nanofibers with a diameter of 130 nm. The diamond photonic crystals and the *in vivo* air spaces both are continuous phases in the scales of *P. nobilis*. In contrast, the scales of *D. similis* are composed of an opal-structured photonic crystals stacked by layers of nanospheres with a diameter of 200 nm. The *in vivo* air spaces in the scales of *D. similis* do not form continuous phases. The diamond structures in the scales of *P. nobilis* produce stronger specular reflection light and diverse colours than the opal-like structures in the scales of *D. similis*.

I used the structural parameters of photonic crystals derived from EM images and conducted computer simulations to investigate the relationships of their produced colouration with structures. Energy band diagrams of the diamond structured photonic crystals in *P. nobilis* and the opal structured photonic crystals in *D. similis* are calculated through the MIT Photonic-Bands package (MPB). I extracted the calculated spectra properties from their band diagrams and plotted the FWHM against the wavelength of the two structural systems in Figure 6.4B. The full bandgap of the diamond crystals explains why diverse colours are displayed in *P. nobilis*‘s scales. Because every crystal

orientation reflects certain colour, differently rotated domains with diamond structures then reflect the light of cyan with the crystal plane of (210) to yellow with the crystal plane of (111). The opal structures in *D. similis* form partial energy bandgap, and only domains with (100) and (111) normal to the scale surface can generate cyan and green colours and be detected by the optic fibre. My simulation predicts well with the optical fibre detected reflection responses of the two species, so it confirms the imperfect mimicry on the colouration of *D. similis* and *P.nobilis* results from the different photonic crystal structural designs at the nanoscale.

I used AFM-IR to probe the local compositions in the photonic crystals and shells of the scales of two species. As the IR spectra shown in Figure 6.4C, I found high lipid contents (IR peak at 1750 cm^{-1}) in the shell and opal photonic crystals of scales of the *D. similis,* especially the lipid seems to be the main component forming the shell of the scales of *D. similis*. On the other hand, *P.nobilis* developed the outer shell and inner diamond photonic crystals using similar cuticular proteins with no lipid detected. These very different IR signals from the scales of the two species refer to that *P.nobilis* and *D. similis* develop the photonic crystals following very different processes. Photonic crystal structures of Coleoptera shown in Appendix Table S1 reveals that most *Pachyrhynchus* weevils have diamond structured photonic crystals (8/11 have diamond structures, 2/11 have amorphous fibrous structures, 1/11 has diamond+ gyroid mixing phases), and most studied longhorn beetles have opal structures (6/8 have opal structures, 2/8 have amorphous phases). Therefore, we proposed the lattice structure of the photonic crystals seems to be a homological phenotype in species. The perfect mimicry with structural colours can be very difficult because it might require gene mutations in the mimics to overcome huge phylogenetic constraints.

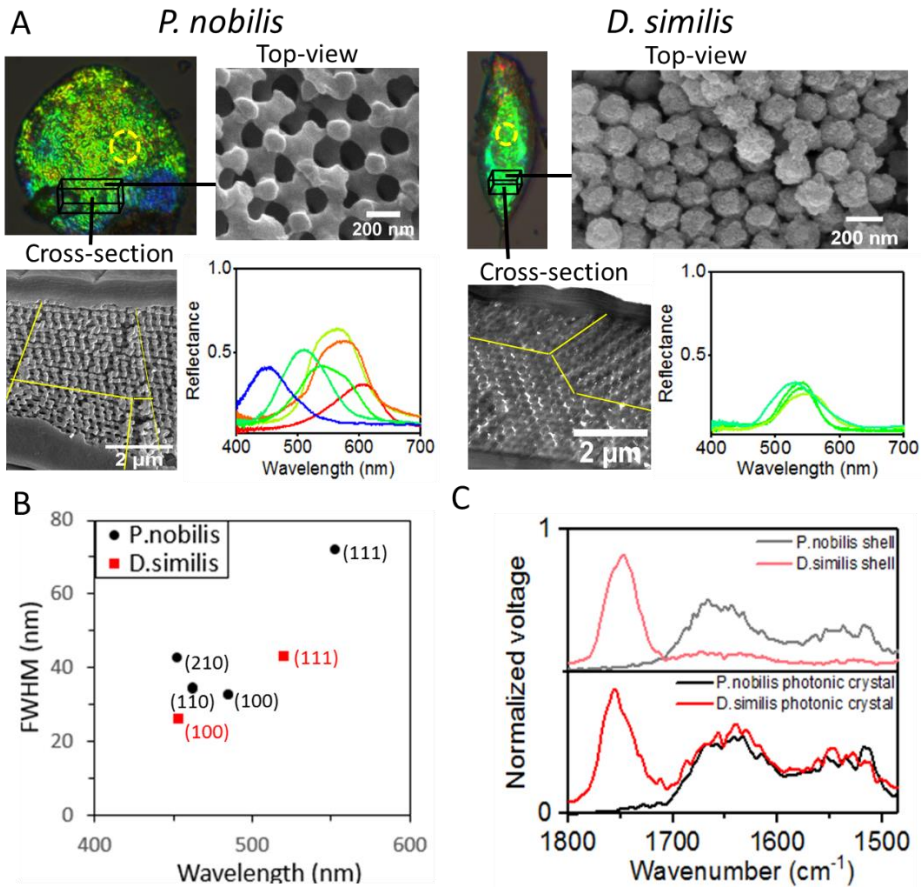

Figure 6.4 The coloured scales, SEM images of photonic crystals in scales, and reflection spectra detected with the spot size of 6 μm (yellow-dashed circle on images). (A) *P. nobilis* has bigger and plate-like scales and the photonic crystal is the diamond structure woven by many nanofibers with a diameter of 130 nm. Differently coloured domains and scales (from cyan to yellow) are observed in *P. nobilis*. *D. similis* has small and needle-like scales and the photonic crystal is the opal structure piled up by nanospheres with a diameter of 200 nm. (B) MPB calculated band diagrams of *D. similis* and *P. nobilis*. Four orientations of the diamond structure of *P. nobilis* can generate colours from green to amber. Two orientations (100) and (111) of the opal structure of *D. similis* possibly generate colours of cyan and green. (C) AFM-IR spectra of the photonic crystals and shells of the scales of two species.

6.4 Discussion

The difference between the interlocking of elytra makes *P. nobilis* and *D. similis* divergent on the secondary defence strategy that the former uses fused elytra for defence while the latter needs to fly for escape. However, we found *D. similis* shows

convergent phenotypes as *P. nobilis* not just on their visual appearances but also the components and microstructure designs of thick elytra. None of the other flyable longhorns in Cerambycidae shows such similar elytra structures as *D. similis*. Our field experiences showed that *D. similis* are very rare in the wild. I speculated due to such rarity, the opened elytra and the capability of flight may benefit *D. similis* to remain high mobility [227,228]. However, the opened elytra with such heavy designs seem lower *D. similis*'s efficiency of flight also risks them of death from predators' attacks [252,253]. This might imply *D. similis*'s success on the primary defence to confuse potential predators by mimicking the appearance of *P. nobilis*.

P. nobilis and *D. similis* both generate structural colours but with different photonic crystals with completely different pathways. It is less possible for *P. nobilis* and *D. similis* succeed shared ancestral genes to produce high-fidelity mimicry. *P. nobilis* uses chitin/protein fibres to assemble three-dimensional diamond lattices in the scales, whereas *D. similis* uses lipid-rich chitin/protein nanospheres to form three-dimensional opal lattices. The two photonic crystals create colours through different light-structure interference mechanisms leading to diverse coloured domains in *P. nobilis* while single green coloured domains in *D. similis*. At the macroscale, *P. nobilis* shows the overall visual colour of green, and *D. similis* successfully displays similar green colours by adjusting the diameters and packing of the nanospheres in the opal structure. The two species may develop their photonic crystals under strong phylogenetic constraints since most studied beetles in Curculionidae family have three-dimensional diamond photonic crystal structures [62,205–207,209,212,220,254], on the other hand, most longhorn beetles in Cerambycidae family have been reported possessing opal photonic crystals [22,107,206,255].

Moreover, because the colour producing mechanisms of diamond and opal structures are after all very different, *D. similis* cannot generate the same intense colours as *P.*

nobilis. The limited cognition of predators relaxes the selection level and allows such imprecision on brightness and patterns to achieve effective aposematic functions. The production of colours through structures rather than pigments lets *D. similis* tune colour as similar as *P. nobilis* without gene mutations or innovations on compositions which further lowers the energy cost in evolution for *D. similis*. This result is very different from previously studied Batesian mimicry pairs in snakes and butterflies in that the same pigments or genes were adapted by the models and the mimics. For example, Kikuchi and Pfenning found the scarlet kingsnake *Lampropeltis elapsoides* (the Batesian mimics) produces its colour with exactly the same physiological mechanisms as the eastern coral snake *Micrurus fulvius* (the Batesian models) [223]. It is possible because not many selections of pigments and chromatophores are in snakes.

To conclude, thorough this investigation of Batesian mimicry pair of *P. nobilis* and *D. similis*, I found such imperfect mimicry is based on phylogenetic constraints, and on constraints due to multifunctionality as well as the availability of alternative mechanisms. For such, I emphasized the role of structural colours in the development of convergent because the structural designs provide the mimics the alternative mechanisms to develop similar colours without developing the same genes or compositional materials such as pigments which might be difficult due to the phylogenetic constraints.

7 Conclusions and future works

Diverse living colours are displayed by organisms with many different strategies. This thesis shows the joint efforts from entomology, physic, and chemistry communities on investigating functional structures and their association with living colours and mechanical properties. In addition, the findings in this thesis provide some new concepts or implications on the development of those functional structures. My results also highlight the importance of the identification of the molecular properties in order to understand the morphogenesis of living structures in future works.

Chapter 4 is in fact the following work after the discovery of left-handed and right-handed helicoidal structures in the cell walls of *Pollia condensata* fruits in our group back in 2012 (DOI:10.1073/pnas.1210105109). We have been curious how the reversal chirality of cells is formed in the same tissues in *P. condensata*. I developed a new physical method to probe cell compositions as the separation of the polysaccharide molecules and characterization of the molecular properties in the cell wall of each single cell is impossible *via* current techniques or microscopes available in our lab or collaborator's lab. My findings of the correlations of stiffness, pitch lengths, and handedness strengthen one of the hypotheses of growth in plants that the orientations of cellulose microfibrils are controlled by hemicellulose. My findings shed new light on the study of the morphogenesis of cellulose helicoidal plant cell walls, and future works should focus on comparing the compositional differences of each individual cells with different pitches and chirality. For example, we are currently applying to access the high-resolution TEM in Diamond Light Source in the UK which is equipped with a finer probe (< 10 nm). I expect to see different properties and densities of cellulose microfibrils in individual cells with enhanced probe sensitivity.

In Chapter 5, by hybridizing differently coloured *Pachyrhynchus sarcitis* in the lab, I found the first generations of *P. sarcitis* always possess a mixing colour of their parents. Complemented with my study on the nanostructures of their photonic crystals, I showed direct evidence of the inheritable structural parameters of the three-dimensional photonic crystals in beetles. Future works will focus on hybridizing *P. sarcitis*, breeding second filial generations (F2) of *P. sarcitis*, and comparing the phenotypes such as colour and structural changes of photonic crystals in different generations. By comparing the F2 phenotypes and the frequency with which they occur, it could reveal how many genes are involved in the colour phenotypes and associated with the structural parameters such as the lattice constant and crystal orientations.

In Chapter 6, I compared the convergent traits of the Batesian mimicry pair of *Pachyrhynchus nobilis* and *Doliops similis* and found the mimicry pair developed similar structural colours *via* completely different nanostructures. This differs from other Batesian mimicry pairs such as butterflies or snakes that the same genetically controlled pigments or compositions have been developed. This highlights the importance of structural designs in the evolution of Batesian mimicry pairs. Future works will focus on comparing the molecular compositions of photonic crystals between *Pachyrhynchus nobilis* and *Doliops similis* to resolve the factors of forming diamond photonic crystals and opal photonic crystals. Another interesting investigation will be on the growth of their elytra. Being inspired by Anbutsu et al.'s findings on the relationships of symbiont and the development of elytra [251], together with my observations on the very similar designs of elytra of *Pachyrhynchus nobilis* and *Doliops similis*, I suspect that the development of elytra might associate with the environment and possibly with the diet of insects. A more careful investigation on comparing the

inorganic compositions in the elytra and on the host plants of the species will be conducted by using the high-resolution Raman or TEM EELS.

Finally, my current comparisons of colours are based on the spectra properties or human vision. However, how different the appearance of the mimicry pairs viewed by the potential predators is unknown. Future works will focus on behaviour studies and the analyses of vision models of potential predators in order to resolve possible functions of such convergent traits developed in *Pachyrhynchus nobilis* and *Doliops similis*.

References

1. Siefferman, L. &Hill, G. E. Structural and melanin coloration indicate parental effort and reproductive success in male eastern bluebirds. *Behav. Ecol.* **14**, 855–861 (2003).

2. Kinoshita, S., Yoshioka, S. &Miyazaki, J. *Physics of structural colors*. *Reports on Progress in Physics* (2008). doi:10.1088/0034-4885/71/7/076401

3. Tseng, H. Y., Lin, C. P., Hsu, J. Y., Pike, D. A. &Huang, W. S. The functional significance of aposematic signals: Geographic variation in the responses of widespread lizard predators to colourful invertebrate prey. *PLoS One* **9**, e91777 (2014).

4. Lee, C. Y. *et al.* The role of different visual characters of weevils signalling aposematism to sympatric lizard predators. *J. Zool.* **306**, 36–47 (2018).

5. Vallin, A., Jakobsson, S., Lind, J. &Wiklund, C. Prey survival by predator intimidation: an experimental study of peacock butterfly defence against blue tits. *Proceedings. Biol. Sci.* **272**, 1203–1207 (2005).

6. Bezzerides, A. L., McGraw, K. J., Parker, R. S. &Husseini, J. Elytra color as a signal of chemical defense in the Asian ladybird beetle Harmonia axyridis. *Behav. Ecol. Sociobiol.* **61**, 1401–1408 (2007).

7. Kemp, D. J. Female mating biases for bright ultraviolet iridescence in the butterfly Eurema hecabe (Pieridae). *Behav. Ecol.* **19**, 1–8 (2007).

8. Carroll, S. B. How Great Wings Can Look Alike. *Science (80-.).* **333**, 1100–1101 (2011).

9. Cuthill, I. C. *et al. The biology of color*. *Science* (2017). doi:10.1126/science.aan0221

10. Kingsolver, J. G. Thermoregulation, flight, and the evolution of wing pattern in pierid butterflies: the topography of adaptive landscapes. *Am. Zool.* **28**, 899–912 (1988).

11. Kingsolver, J. G. &Huey, R. B. Evolutionary analyses of morphological and physiological plasticity in thermally variable environments. *Am. Zool.* **38**, 545–560 (1998).

12. Nishimoto, S. &Bhushan, B. Bioinspired self-cleaning surfaces with superhydrophobicity, superoleophobicity, and superhydrophilicity. *Rsc Adv.* **3**, 671–690 (2013).

13. Bixler, G. D. &Bhushan, B. Fluid drag reduction and efficient self-cleaning with rice leaf and butterfly wing bioinspired surfaces. *Nanoscale* **5**, 7685–7710 (2013).

14. Dell'Aglio, D. D., Stevens, M. &Jiggins, C. D. Avoidance of an aposematically coloured butterfly by wild birds in a tropical forest. *Ecol. Entomol.* **41**, 627–632 (2016).

15. Hong, C., Maosheng, C. &Jiurong, S. Histological structures of the dung beetle, Copris ochus motschulsky integument. *Kun chong xue bao. Acta Entomol. Sin.* **46**, 429—435 (2003).

16. Thompson, D. W. On growth and form. *On growth and form.* (1942).

17. Fratzl, P. &Weinkamer, R. Nature's hierarchical materials. *Prog. Mater. Sci.* **52**, 1263–1334 (2007).

18. Lakes, R. Materials with structural hierarchy. *Nature* **361**, 511–515 (1993).

19. Kinoshita, S. *Structural colors in the realm of nature*. *World* (2008). doi:10.1016/B978-008043924-2/50055-9

20. Chen, P.-Y., McKittrick, J. &Meyers, M. A. Biological materials: functional adaptations and bioinspired designs. *Prog. Mater. Sci.* **57**, 1492–1704 (2012).

21. Middleton, R. Structural colour in fruits. (University of Cambridge, 2019).

22. Seago, A. E., Brady, P., Vigneron, J. P. &Schultz, T. D. Gold bugs and beyond: A review of iridescence and structural colour mechanisms in beetles (Coleoptera). *J. R. Soc. Interface* **6**, (2009).

23. Sun, C.-Y. &Chen, P.-Y. Structural design and mechanical behavior of alligator (Alligator mississippiensis) osteoderms. *Acta Biomater.* **9**, 9049–9064 (2013).

24. Neville, A. &Levy, S. The helicoidal concept in plant cell wall ultrastructure and morphogenesis. in *Biochemistry of plant cell walls* **28**, 99–124 (CUP, 1985).

25. Wilts, B. D., Whitney, H. M., Glover, B. J., Steiner, U. &Vignolini, S. Natural Helicoidal Structures: Morphology, Self-assembly and Optical Properties. *Mater. Today Proc.* **1**, 177–185 (2014).

26. Vincent, J. F.V &Wegst, U. G. K. Design and mechanical properties of insect cuticle. *Arthropod Struct. Dev.* **33**, 187–199 (2004).

27. Thomas, K. R., Kolle, M., Whitney, H. M., Glover, B. J. &Steiner, U. Function of blue iridescence in tropical understorey plants. *J. R. Soc. Interface* **7**, 1699–1707 (2010).

28. Brady, P. &Cummings, M. Differential response to circularly polarized light by the jewel scarab beetle Chrysina gloriosa. *Am. Nat.* **175**, 614–620 (2010).

29. Gutierrez, R., Lindeboom, J. J., Paredez, A. R., Emons, A. M. C. &Ehrhardt, D. W. Arabidopsis cortical microtubules position cellulose synthase delivery to the plasma membrane and interact with cellulose synthase trafficking compartments. *Nat. Cell Biol.* **11**, 797–806 (2009).

30. Paredez, A. R., Somerville, C. R. &Ehrhardt, D. W. Visualization of cellulose synthase demonstrates functional association with microtubules. *Science (80-.).* **312**, 1491–1495 (2006).

31. Chan, J. Microtubule and cellulose microfibril orientation during plant cell and organ growth. *J. Microsc.* **247**, 23–32 (2012).

32. Kurata, Y. *et al.* Variation in hemicellulose structure and assembly in the cell wall associated with the transition from earlywood to latewood in Cryptomeria japonica. *J. Wood Chem. Technol.* **38**, 254–263 (2018).

33. Yi, H. &Puri, V. M. Architecture-based multiscale computational modeling of plant cell wall mechanics to examine the hydrogen-bonding hypothesis of the cell wall network structure model. *Plant Physiol.* **160**, 1281–1292 (2012).

34. Kutschera, U. The growing outer epidermal wall: design and physiological role of a composite structure. *Ann. Bot.* **101**, 615–621 (2008).

35. Neville, A. C. A pipe-cleaner molecular model for morphogenesis of helicoidal plant cell walls based on hemicellulose complexity. *J. Theor. Biol.* **131**, 243–254 (1988).

36. Reis, D. &Vian, B. Helicoidal pattern in secondary cell walls and possible role of xylans in their construction. *C. R. Biol.* **327**, 785–790 (2004).

37. Dinwiddie, A. *et al.* Dynamics of F-actin prefigure the structure of butterfly wing scales. *Dev. Biol.* **392**, 404–418 (2014).

38. Ghiradella, H. Structure and development of iridescent butterfly scales: Lattices and laminae. *J. Morphol.* **202**, 69–88 (1989).

39. Wilts, B. D. *et al.* Butterfly gyroid nanostructures as a time-frozen glimpse of intracellular membrane development. *Sci. Adv.* **3**, e1603119 (2017).

40. Liu, K. &Jiang, L. Bio-inspired design of multiscale structures for function integration. *Nano Today* **6**, 155–175 (2011).

41. La, Y. *et al.* Templated synthesis of cubic crystalline single networks having large open-space lattices by polymer cubosomes. *Nat. Commun.* **9**, 1–9 (2018).

42. Jativa, F., Schütz, C., Bergström, L., Zhang, X. &Wicklein, B. Confined self-assembly of cellulose nanocrystals in a shrinking droplet. *Soft Matter* **11**, 5374–5380 (2015).

43. Galisteo-López, J. F. *et al.* Self-Assembled Photonic Structures. *Adv. Mater.* **23**, 30–69 (2011).

44. Goerlitzer, E. S. A., Klupp Taylor, R. N. &Vogel, N. Bioinspired Photonic Pigments from Colloidal Self-Assembly. *Adv. Mater.* **30**, 1706654 (2018).

45. Wilts, B. D., Clode, P. L., Patel, N. H. &Schröder-Turk, G. E. Nature's functional nanomaterials: Growth or self-assembly? *MRS Bull.* **44**, 106–112 (2019).

46. Wilts, B. D., Michielsen, K., Kuipers, J., DeRaedt, H. &Stavenga, D. G. Brilliant camouflage: Photonic crystals in the diamond weevil, Entimus imperialis. *Proc. R. Soc. B Biol. Sci.* **279**, 2524–2530 (2012).

47. Hecht, E. *Optics, 4th*. **3**, (2002).

48. Glover, B. J. &Whitney, H. M. Structural colour and iridescence in plants: the poorly studied relations of pigment colour. *Ann. Bot.* **105**, 505–511 (2010).

49. Crowson, R. A. *The Biology of the Coleoptera*. (Elsevier Science, 2013).

50. Parker, A. R., Mckenzie, D. R. &Large, M. C. J. Multilayer reflectors in animals using green and gold beetles as contrasting examples. *J. Exp. Biol.* **201**, 1307–1313 (1998).

51. McNamara, M. E. *et al.* Cryptic iridescence in a fossil weevil generated by single diamond photonic crystals. *J. R. Soc. Interface* **11**, 20140736 (2014).

52. Vinther, J., Briggs, D. E. G., Clarke, J., Mayr, G. &Prum, R. O. Structural coloration in a fossil feather. *Biol. Lett.* **6**, 128 (2009).

53. Strutt, J. W. On the reflection of light from a regularly stratified medium. *Proc. R. Soc. London. Ser. A, Contain. Pap. a Math. Phys. Character* **93**, 565–577 (1917).

54. Yablonovitch, E. Photonic band-gap structures. *Photonic Band Gap Mater.* **10**, 283–295 (1993).

55. Joannopoulos, J. D., Johnson, S. G., Winn, J. N. &Meade, R. D. *Photonic crystals: molding the flow of light*. (Princeton university press, 2011).

56. Maka, T., Chigrin, D., Romanov, S. &Sotomayor Torres, C. Three Dimensional Photonic Crystals in the Visible Regime. in *Progress in Electromagnetics Research-pier - Prog Electromagn Res* **41**, 307- (2003).

57. Newton, I. &Innys, W. *Opticks:: Or, A Treatise of the Reflections, Refractions, Inflections and Colours of Light*. (William Innys at the West-End of St. Paul's., 1730).

58. Johansen, V. E. *et al.* Genetic manipulation of structural color in bacterial colonies. *Proc. Natl. Acad. Sci.* **115**, 2652–2657 (2018).

59. Wilts, B. D., Michielsen, K., DeRaedt, H. &Stavenga, D. G. Sparkling feather reflections of a bird-of-paradise explained by finite-difference time-domain modeling. *Proc. Natl. Acad. Sci.* **111**, 4363 LP – 4368 (2014).

60. Yin, H. *et al.* Amorphous diamond-structured photonic crystal in the feather barbs of the scarlet macaw. *Proc. Natl. Acad. Sci.* **109**, 10798–10801 (2012).

61. Prum, R. O., Dufresne, E. R., Quinn, T. &Waters, K. Development of colour-producing -keratin nanostructures in avian feather barbs. *J. R. Soc. Interface* **6**, S253 (2009).

62. Chang, Y. *et al.* Hereditary Character of Photonics Structure in Pachyrhynchus sarcitis Weevils: Color Changes via One Generation Hybridization. *Adv. Opt. Mater.* **8**, 2000432 (2020).

63. Wilts, B. D., Michielsen, K., Kuipers, J., DeRaedt, H. &Stavenga, D. G. Brilliant camouflage: photonic crystals in the diamond weevil, \textit{Entimus imperialis}. *Proc. R. Soc. B Biol. Sci.* **279**, 2524 (2012).

64. Ghiradella, H. Structure of butterfly scales: patterning in an insect cuticle. *Microsc. Res. Tech.* **27**, 429 (1994).

65. Onelli, O. D. *et al.* Development of structural colour in leaf beetles. *Sci. Rep.* **7**, (2017).

66. Vignolini, S. *et al.* Pointillist structural color in Pollia fruit. *Proc. Natl. Acad. Sci.* **109**, 15712–15715 (2012).

67. Hooke, R. *Micrographia: Or, Some Physiological Descriptions of Minute Bodies Made by Magnifying Glasses. With Observations and Inquiries Thereupon*. (J. Allestry, printer to the Royal Society, 1667).

68. Darwin, C. &Carroll, J. *On the Origin of Species*. (Broadview Press, 2003).

69. Maxwell, J. C. &Torrance, T. F. *A Dynamical Theory of the Electromagnetic Field*. (Wipf & Stock, 1996).

70. Michelson, A. A. LXI. On metallic colouring in birds and insects. *London, Edinburgh, Dublin Philos. Mag. J. Sci.* **21**, 554–567 (1911).

71. Anderson, T. F. &Richards, A. G. An Electron Microscope Study of Some Structural Colors of Insects. *J. Appl. Phys.* **13**, 748–758 (1942).

72. Parker, A. R. 515 million years of structural colour. *J. Opt. A Pure Appl. Opt.* **2**, R15–R28 (2000).

73. Vukusic, P. &Sambles, J. R. Photonic structures in biology. *Nature* **424**, 852 (2003).

74. Johansen, V. E., Onelli, O. D., Steiner, L. M. &Vignolini, S. Photonics in Nature: From Order to Disorder. in *Functional Surfaces in Biology III: Diversity of the Physical Phenomena* (eds. Gorb, S. N. &Gorb, E.V) 53–89 (Springer International Publishing, 2017). doi:10.1007/978-3-319-74144-4_3

75. Parker, A. R. The diversity and implications of animal structural colours. *J. Exp. Biol.* **201**, 2343–2347 (1998).

76. Kinoshita, S. &Yoshioka, S. Structural colors in nature: the role of regularity and irregularity in the structure. *ChemPhysChem* **6**, 1442–1459 (2005).

77. Endler, J. A. Some general comments on the evolution and design of animal communication systems. *Philos. Trans. - R. Soc. London, B* **340**, 215–225 (1993).

78. Srinivasarao, M. Nano-optics in the biological world: beetles, butterflies, birds, and moths. *Chem. Rev.* **53**, 5711–5719 (1999).

79. Wilts, B. D. *et al.* Evolutionary-optimized photonic network structure in white beetle wing scales. *Adv. Mater.* **30**, e1702057 (2018).

80. Xu, Q., Ouyang, J., Yang, Y., Ito, T. &Kido, J. Ultrahigh efficiency green polymer light-emitting diodes by nanoscale interface modification. *Appl. Phys. Lett.* **83**, 4695–4697 (2003).

81. Russell, P. Photonic Crystal Fibers. *Science (80-.).* **299**, 358–362 (2003).

82. Liu, B.-W. *et al.* High-power wavelength-tunable photonic-crystal-fiber-based oscillator-amplifier-frequency-shifter femtosecond laser system and its applications for material microprocessing. *Laser Phys. Lett.* **6**, 44–48 (2009).

83. Mason, C. W. Structural colors in insects. I. *J. Phys. Chem.* **30**, 383–395 (2002).

84. Yoshioka, S., Nakamura, E. &Kinoshita, S. Origin of two-color iridescence in rock dove's feather. *J. Phys. Soc. Japan* **76**, 13801 (2007).

85. Hsiung, B.-K. *et al.* Rainbow peacock spiders inspire miniature super-iridescent optics. *Nat. Commun.* **8**, 1–8 (2017).

86. Monroe, E. A. &Monroe, S. E. Origin of iridescent colors on the indigo snake. *Science (80-.).* **159**, 97–98 (1968).

87. Lee, D. W. *Nature's palette: the science of plant color*. (University Of Chicago Press, 2007).

88. Whitney, H. M. *et al.* Floral iridescence, produced by diffractive optics, acts as a cue for animal pollinators. *Science (80-.).* **323**, 130–133 (2009).

89. Denton, E. J. &Land, M. F. Mechanism of reflexion in silvery layers of fish and cephalopods. *Proc. R. Soc. London B Biol. Sci.* **178**, 43–61 (1971).

90. Land, M. F. The physics and biology of animal reflectors. *Prog. Biophys. Mol. Biol.* **24**, 75–106 (1972).

91. Noyes, J. A., Vukusic, P. &Hooper, I. R. Experimental method for reliably establishing the refractive index of buprestid beetle exocuticle. *Opt. Express* **15**, 4351 (2007).

92. Campos Fernández, C. *et al.* Visible light reflection spectra from cuticle layered materials. *Opt. Mater. Express* **1**, 85–100 (2011).

93. Cook, C. Q. &Amir, A. Theory of chirped photonic crystals in biological broadband reflectors. *Optica* **3**, 1436–1439 (2016).

94. McKenzie, D. R., Yin, Y. &McFall, W. D. Silvery fish skin as an example of a chaotic reflector. in *Proceedings of the Royal Society of London A: Mathematical, Physical and Engineering Sciences* **451**, 579–584 (1995).

95. Denton, E. J. Review lecture: on the organization of reflecting surfaces in some marine animals. *Philos. Trans. R. Soc. London B Biol. Sci.* **258**, 285–313 (1970).

96. Neville, A. C. Metallic gold and silver colours in some insect cuticles. *J. Insect Physiol.* **23**, 1267–1274 (1977).

97. Denton, E. J. &Nicol, J. A. C. Reflexion of light by external surfaces of the herring, Clupea harengus. *J. Mar. Biol. Assoc. United Kingdom* **45**, 711–738 (1965).

98. Arrigo, M. I. *et al.* Phylogenetic mapping of scale nanostructure diversity in snakes. *BMC Evol. Biol.* **19**, 91 (2019).

99. Vignolini, S. *et al.* The flower of Hibiscus trionum is both visibly and measurably iridescent. *New Phytol.* **205**, 97–101 (2015).

100. Michielsen, K. &Stavenga, D. G. Gyroid cuticular structures in butterfly wing scales: Biological photonic crystals. *J. R. Soc. Interface* **5**, (2008).

101. Winter, B. *et al.* Coexistence of both gyroid chiralities in individual butterfly wing scales of Callophrys rubi *Proc. Natl. Acad. Sci.* **112**, 12911 LP – 12916 (2015).

102. Prum, R. O., Hill, G. E. &McGraw, K. J. Anatomy, physics, and evolution of avian structural colors. in *Bird Coloration* **1**, (Harvard University Press, 2006).

103. Chandler, C. J., Wilts, B. D., Brodie, J. &Vignolini, S. Structural color in marine algae. *Adv. Opt. Mater.* **5**, 1600646 (2017).

104. Liu, F., Dong, B. Q., Liu, X. H., Zheng, Y. M. &Zi, J. Structural color change in longhorn beetles Tmesisternus isabellae. *Opt. Express* **17**, 16183–16191 (2009).

105. González-Segredo, N. &Coveney, P.V. Self-assembly of the gyroid cubic mesophase: lattice-Boltzmann simulations. *EPL (Europhysics Lett.* **65**, 795 (2004).

106. Saranathan, V. *et al.* Structure, function, and self-assembly of single network gyroid (I4132) photonic crystals in butterfly wing scales. *Proc. Natl. Acad. Sci.* **107**, 11676–11681 (2010).

107. Dong, B. Q. *et al.* Structural coloration and photonic pseudogap in natural random close-packing photonic structures. *Opt. Express* **18**, 14430–14438 (2010).

108. Gibson, L. J. &Ashby, M. F. *Cellular Solids: Structure and Properties*. (Cambridge University Press, 1999).

109. Wegst, U. G. K. &Ashby, M. F. The mechanical efficiency of natural materials. *Philos. Mag.* **84**, 2167–2186 (2004).

110. Voigt, W. Ueber die Beziehung zwischen den beiden Elasticitätsconstanten isotroper Körper. *Ann. Phys.* **274**, 573–587 (1889).

111. Ritchie, R. O. The conflicts between strength and toughness. *Nat. Mater.* **10**, 817–822 (2011).

112. Sarkar, P. *et al*. Cryo-Electron tomography 3D structure and nanoscale model of Arabidopsis thaliana cell wall. *bioRxiv* 492140 (2018).

113. Wegst, U. G., Bai, H., Saiz, E., Tomsia, A. P. &Ritchie, R. O. Bioinspired structural materials. *Nat. Mater.* **14**, 23–36 (2015).

114. Chung, C.-Y. Evaluation of the Mechanical Behavior and Material Properties of Native and Tissue-engineered Cartilage Using Finite Element Analysis and Ultrasonic Elastography Measurement. (Case Western Reserve University, 2015).

115. Badylak, S. F., Freytes, D. O. &Gilbert, T. W. Reprint of: Extracellular matrix as a biological scaffold material: Structure and function. *Acta Biomaterialia* **5**, 1–13 (2015).

116. Han, L., Grodzinsky, A. J. &Ortiz, C. Nanomechanics of the cartilage extracellular matrix. *Annu. Rev. Mater. Res.* **41**, 133–168 (2011).

117. Hermans, P. H. *Contribution to the physics of cellulose fibres*. (Elseview Publishing Company, Iinc.; London, 1946).

118. Ikoma, T., Kobayashi, H., Tanaka, J., Walsh, D. &Mann, S. Microstructure, mechanical, and biomimetic properties of fish scales from Pagrus major. *J. Struct. Biol.* **142**, 327–333 (2003).

119. Lin, Y. S., Wei, C. T., Olevsky, E. A. &Meyers, M. A. Mechanical properties and the laminate structure of Arapaima gigas scales. *J. Mech. Behav. Biomed. Mater.* **4**, 1145–1156 (2011).

120. Chang, Y. &Chen, P.-Y. Hierarchical structure and mechanical properties of snake (Naja atra) and turtle (Ocadia sinensis) eggshells. *Acta Biomater.* **31**, 33–49 (2016).

121. Giraud-Guille, M.-M. Twisted plywood architecture of collagen fibrils in human compact bone osteons. *Calcif. Tissue Int.* **42**, 167–180 (1988).

122. Ribbans, B. Bioinspired study on the mechanical performance of helicoidal fiber structures. (University of Vermont, 2015).

123. Neville, A. C. *Biology of fibrous composites: development beyond the cell membrane*. (Cambridge University Press, 1993).

124. Neville, A. C. *Biology of the Arthropod Cuticle*. (Springer-Verlag Berlin, 1975).

125. Neville, A. C. Molecular and mechanical aspects of helicoid development in plant cell walls. *BioEssays* **3**, 4–8 (1985).

126. Weaver, J. C. *et al.* The stomatopod dactyl club: a formidable damage-tolerant biological hammer. *Science (80-.).* **336**, 1275–1280 (2012).

127. Natarajan, B. &Gilman, J. W. Bioinspired Bouligand cellulose nanocrystal composites: a review of mechanical properties. *Philos. Trans. R. Soc. A Math. Phys. Eng. Sci.* **376**, 20170050 (2018).

128. deVries, H. Rotatory power and other optical properties of certain liquid crystals. *Acta Crystallogr.* **4**, 219–226 (1951).

129. Oseen, C. W. The theory of liquid crystals. *Trans. Faraday Soc.* **29**, 883–899 (1933).

130. Kats, E. I. Optical Properties of Cholesteric Liquid Crystals. *Sov. Phys. JETP* **32**, 1004 (1971).

131. Neville, A. C. &Caveney, S. Scarabaeid beetle exocuticle as an optical analogue of cholesteric liquid crystals. *Biol. Rev.* **44**, 531–562 (1969).

132. Chiou, T.-H. *et al.* Circular Polarization Vision in a Stomatopod Crustacean. *Curr. Biol.* **18**, 429–434 (2008).

133. Gagnon, Y. L., Templin, R. M., How, M. J. &Marshall, N. J. Circularly Polarized Light as a Communication Signal in Mantis Shrimps. *Curr. Biol.* **25**, 3074–3078 (2015).

134. Goldstein, D. H. Polarization properties of Scarabaeidae. *Appl. Opt.* **45**, 7944–7950 (2006).

135. Goldstein, D. H. *Polarized light*. (CRC press, 2017).

136. Caveney, S. Cuticle reflectivity and optical activity in scarab beetles: the role of uric acid. *Proc. R. Soc. London. Ser. B. Biol. Sci.* **178**, 205–225 (1971).

137. Jewell, S. A., Vukusic, P. &Roberts, N. W. Circularly polarized colour reflection from helicoidal structures in the beetle Plusiotis boucardi. *New J. Phys.* **9**, 99 (2007).

138. Fox, A. M. &Fox, D. P. A. M. *Optical Properties of Solids*. (Oxford University Press, 2001).

139. Joannopoulos, J. D., Johnson, S. G., Winn, J. N. &Meade, R. D. *Photonic Crystals: Molding the Flow of Light - Second Edition*. (Princeton University Press, 2011).

140. Macleod, H. A. *Thin-film optical filters*. (CRC press, 2017).

141. Kolle, M. Photonic Structures Inspired by Nature. (University of Cambridge, 2011). doi:10.1007/978-3-642-15169-9_2

142. Sakurai, J. J. &Commins, E. D. *Modern quantum mechanics, second edition*. (Cambridge University Press, 2017).

143. Yablonovitch, E. Inhibited spontaneous emission in solid-state physics and electronics. *Phys. Rev. Lett.* **58**, 2059 (1987).

144. Zheng, Y.-P., Choi, A. P. C., Ling, H. Y. &Huang, Y.-P. Simultaneous estimation of Poisson's ratio and Young's modulus using a single indentation: a finite element study. *Meas. Sci. Technol.* **20**, 45706 (2009).

145. Oliver, W. C. &Pharr, G. M. An improved technique for determining hardness and elastic modulus using load and displacement sensing indentation experiments. *J. Mater. Res.* **7**, 1564–1583 (1992).

146. Johnson, K. L., Greenwood, J. A. &Higginson, J. G. The contact of elastic regular wavy surfaces. *Int. J. Mech. Sci.* **27**, 383–396 (1985).

147. Oyen, M. L. *et al. Handbook of nanoindentation: with biological applications*. *Applied Physics Letters* **82**, (CRC Press, 2003).

148. Oyen, M. L. Mechanical characterisation of hydrogel materials. *Int. Mater. Rev.* **59**, 44–59 (2014).

149. Labonte, D., Lenz, A.-K. &Oyen, M. L. On the relationship between indentation hardness and modulus, and the damage resistance of biological materials. *Acta Biomater.* **57**, 373–383 (2017).

150. Huber, M. T. Zur Theorie der Berührung fester elastischer Körper. *Ann. Phys.* **319**, 153–163 (1904).

151. Tabor, D. *The hardness of metals*. (Oxford university press, 2000).

152. Field, J. S. &Swain, M.V. Determining the mechanical properties of small volumes of material from submicrometer spherical indentations. *J. Mater. Res.* **10**, 101–112 (1995).

153. Lin, D. C., Shreiber, D. I., Dimitriadis, E. K. &Horkay, F. Spherical indentation of soft matter beyond the Hertzian regime: numerical and experimental validation of hyperelastic models. *Biomech. Model. Mechanobiol.* **8**, 345 (2009).

154. Guidetti, G. Cellulose photonics: designing functionality and optical appearance of natural materials. (University of Cambridge, 2018).

155. Johnson, S. G. &Joannopoulos, J. D. Block-iterative frequency-domain methods for Maxwell's equations in a planewave basis. *Opt. Express* **8**, 173–190 (2001).

156. Nance, D.V. *Practical photonic bandgap calculations using MPB.* (2013).

157. Yee, K. Numerical solution of initial boundary value problems involving Maxwell's equations in isotropic media. *IEEE Trans. Antennas Propag.* **14**, 302–307 (1966).

158. Taflove, A. &Brodwin, M. E. Numerical solution of steady-state electromagnetic scattering problems using the time-dependent Maxwell's equations. *IEEE Trans. Microw. Theory Tech.* **23**, 623–630 (1975).

159. Zhang, X., Fang, J., Mei, K. K. &Liu, Y. Calculations of the dispersive characteristics of microstrips by the time-domain finite difference method. *IEEE Trans. Microw. Theory Tech.* **36**, 263–267 (1988).

160. Gedney, S. D. An anisotropic perfectly matched layer-absorbing medium for the truncation of FDTD lattices. *IEEE Trans. Antennas Propag.* **44**, 1630–1639 (1996).

161. Berenger, J.-P. A perfectly matched layer for the absorption of electromagnetic waves. *J. Comput. Phys.* **114**, 185–200 (1994).

162. Taflove, A. *Computational Electrodynamics: The Finite-difference Time-domain Method*. (Artech House, 1995).

163. Gould, K. S. &Lee, D. W. Physical and ultrastructural basis of blue leaf iridescence in four Malaysian understory plants. *Am. J. Bot.* **83**, 45–50 (1996).

164. Graham, R. M., Lee, D. W. &Norstog, K. Physical and Ultrastructural Basis of Blue Leaf Iridescence in Two Neotropical Ferns. *Am. J. Bot.* **80**, 198–203 (1993).

165. N Boyce, A. &Duckett, J. G. Dimorphic epidermal cell chloroplasts in the mesophyll-less leaves of an extreme–shade tropical fern, Teratophyllum rotundifoliatum (R. Bonap.) Holtt.: a light and electron microscope study. *New Phytol.* **119**, 433–444 (1991).

166. Sheue, C.-R. *et al.* Bizonoplast, a unique chloroplast in the epidermal cells of microphylls in the shade plant Selaginella erythropus (Selaginellaceae). *Am. J. Bot.* **94**, 1922–1929 (2007).

167. Strout, G. *et al.* Silica nanoparticles aid in structural leaf coloration in the Malaysian tropical rainforest understorey herb Mapania caudata. *Ann. Bot.* **112**, 1141–1148 (2013).

168. Middleton, R. *et al.* Using structural colour to track length scale of cell-wall layers in developing Pollia japonica fruits. *New Phytol.* **n/a**, (2021).

169. Steiner, L. M. *et al.* Structural colours in the frond of Microsorum thailandicum. *Interface Focus* **9**, 20180055 (2019).

170. DelRio, L. F., Arwin, H. &Järrendahl, K. Polarizing properties and structure of the cuticle of scarab beetles from the Chrysina genus. *Phys. Rev. E* **94**, (2016).

171. Äkerlind, C., Arwin, H., Hallberg, T. &Landin, J. Scattering and polarization properties of the scarab beetle Cyphochilus insulanus cuticle. *Appl. Opt.* **54**, 6037 (2015).

172. Tze, W. T. Y., Wang, S., Rials, T. G., Pharr, G. M. &Kelley, S. S. Nanoindentation of wood cell walls: Continuous stiffness and hardness measurements. *Compos. Part A Appl. Sci. Manuf.* **38**, 945–953 (2007).

173. Kutschera, U. &Niklas, K. J. The epidermal-growth-control theory of stem elongation: an old and a new perspective. *J. Plant Physiol.* **164**, 1395–1409 (2007).

174. Neville, A. C. &Luke, B. M. Molecular architecture of adult locust cuticle at the electron microscope level. *Tissue Cell* **1**, 355 (1969).

175. Warrant, E. J. Polarisation Vision: Beetles See Circularly Polarised Light. *Curr. Biol.* **20**, R610–R612 (2010).

176. Horváth, G., Blahó, M., Egri, Á., Hegedüs, R. &Szél, G. Circular polarization vision of scarab beetles. in *Polarized Light and Polarization Vision in Animal Sciences* 147–170 (Springer, 2014).

177. Horvath, G., Horváth, G., Varju, D. &Horváth, G. *Polarized Light in Animal Vision: Polarization Patterns in Nature*. (Springer, 2004).

178. Vigneron, J. P., Colomer, J. F., Vigneron, N. &Lousse, V. Natural layer-by-layer photonic structure in the squamae of Hoplia coerulea (Coleoptera). *Phys. Rev. E - Stat. Nonlinear, Soft Matter Phys.* **72**, 061904 (2005).

179. Partridge, J. C. &Douglas, R. H. Far-red sensitivity of dragon fish. *Nature* **375**, 21–22 (1995).

180. Nixon, M. R., Orr, A. G. &Vukusic, P. Covert linear polarization signatures from brilliant white two-dimensional disordered wing structures of the phoenix damselfly. *J. R. Soc. Interface* **14**, 20170036 (2017).

181. Thoen, H. H., How, M. J., Chiou, T.-H. &Marshall, J. A different form of color vision in mantis shrimp. *Science (80-.).* **343**, 411–413 (2014).

182. Ogawa, Y. Electron microdiffraction reveals the nanoscale twist geometry of cellulose nanocrystals. *Nanoscale* **11**, 21767–21774 (2019).

183. Belli, S., Dussi, S., Dijkstra, M. &vanRoij, R. Density functional theory for chiral nematic liquid crystals. *Phys. Rev. E* **90**, 20503 (2014).

184. Usov, I. *et al.* Understanding nanocellulose chirality and structure-properties relationship at the single fibril level. *Nat. Commun.* **6**, (2015).

185. Paavilainen, S., Róg, T. &Vattulainen, I. Analysis of Twisting of Cellulose Nanofibrils in Atomistic Molecular Dynamics Simulations. *J. Phys. Chem. B* **115**, 3747–3755 (2011).

186. Sturcova, A. *et al.* Elastic Modulus and Stress-Transfer Properties of Tunicate Cellulose Whiskers. *Biomacromolecules* **6**, 1055–1061 (2005).

187. Ruben, G. C., Bokelman, G. H. &Krakow, W. Triple-stranded left-hand helical cellulose microfibril in Acetobacter xylinum and in Tobacco Primary Cell Wall. in *Plant Cell Wall Polymers* **399**, 20–278 (American Chemical Society, 1989).

188. Vignolini, S. *et al.* Structural colour from helicoidal cell-wall architecture in fruits of Margaritaria nobilis. *J. R. Soc. Interface* **13**, 20160645 (2016).

189. Shishehbor, M. &Zavattieri, P. D. Effects of interface properties on the mechanical properties of bio-inspired cellulose nanocrystal (CNC)-based materials. *J. Mech. Phys. Solids* **124**, 871–896 (2019).

190. Nishiyama, Y., Langan, P. &Chanzy, H. Crystal Structure and Hydrogen-Bonding System in Cellulose Ibeta from Synchrotron X-Ray and Neutron Fiber Diffraction. *J. Am. Chem. Soc.* **124**, 9074 (2002).

191. Moon, R. J., Martini, A., Nairn, J., Simonsen, J. &Youngblood, J. Cellulose nanomaterials review: structure, properties and nanocomposites. *Chem. Soc. Rev.* **40**, 3941–3994 (2011).

192. Plimpton, S. Fast parallel algorithms for short-range molecular dynamics. *J. Comput. Phys.* **117**, 1–19 (1995).

193. Leach, A. R. &Leach, A. R. *Molecular modelling: principles and applications*. (Pearson education, 2001).

194. Martyna, G. J., Tobias, D. J. &Klein, M. L. Constant pressure molecular dynamics algorithms. *J. Chem. Phys.* **101**, 4177–4189 (1994).

195. Moerman, K. M. GIBBON: the geometry and image-based bioengineering add-on. *J. Open Source Softw.* **3**, 506 (2018).

196. Maas, S. A., Ellis, B. J., Ateshian, G. A. &Weiss, J. A. FEBio: finite elements for biomechanics. *J. Biomech. Eng.* **134**, 11005 (2012).

197. Wu, K. *et al.* Discontinuous fibrous Bouligand architecture enabling formidable fracture resistance with crack orientation insensitivity. *Proc. Natl. Acad. Sci.* **117**, 15465–15472 (2020).

198. Yang, Y. *et al.* Biomimetic Anisotropic Reinforcement Architectures by Electrically Assisted Nanocomposite 3D Printing. *Adv. Mater.* **29**, 1605750 (2017).

199. Kha, H., Tuble, S. C., Kalyanasundaram, S. &Williamson, R. E. WallGen, software to construct layered cellulose-hemicellulose networks and predict their small deformation mechanics. *Plant Physiol.* **152**, 774–786 (2010).

200. Yi, H. &Puri, V. M. Contributions of the mechanical properties of major structural polysaccharides to the stiffness of a cell wall network model. *Am. J. Bot.* **101**, 244–254 (2014).

201. Sakurada, I., Nukushina, Y. &Ito, T. Experimental determination of the elastic modulus of crystalline regions in oriented polymers. *J. Polym. Sci.* **57**, 651–660 (1962).

202. Resh, V. H. &Cardé, R. T. *Encyclopedia of Insects*. (Elsevier Science, 2009).

203. Pouya, C., Stavenga, D. G. &Vukusic, P. Discovery of ordered and quasi-ordered photonic crystal structures in the scales of the beetle Eupholus magnificus. *Opt. Express* **19**, 11355–11364 (2011).

204. Welch, V. L. &Vigneron, J. P. Beyond butterflies-the diversity of biological photonic crystals. *Opt. Quantum Electron.* **39**, 295–303 (2007).

205. Bartl, M. H., Galusha, J. W., Richey, L. R., Gardner, J. S. &Cha, J. N. Discovery of a diamond-based photonic crystal structure in beetle scales. *Phys. Rev. E - Stat. Nonlinear, Soft Matter Phys.* **77**, 050904 (2008).

206. Saranathan, V. *et al.* Structural diversity of arthropod biophotonic nanostructures spans amphiphilic phase-space. *Nano Lett.* **15**, 3735–3742 (2015).

207. Seago, A. E., Oberprieler, R. &Saranathan, V. K. Evolution of Insect Iridescence: Origins of Three-Dimensional Photonic Crystals in Weevils (Coleoptera: Curculionoidea). *Integr. Comp. Biol.* **59**, 1664–1672 (2019).

208. Ho, K. M., Chan, C. T. &Soukoulis, C. M. Existence of a photonic gap in periodic dielectric structures. *Phys. Rev. Lett.* **65**, 3152–3155 (1990).

209. Wilts, B. D. &Saranathan, V. A literal elytral rainbow: tunable structural colors using single diamond biophotonic crystals in Pachyrrhynchus congestus weevils. *Small* **14**, 1870212 (2018).

210. Galusha, J. W., Richey, L. R., Jorgensen, M. R., Gardner, J. S. &Bartl, M. H. Study of natural photonic crystals in beetle scales and their conversion into inorganic structures via a sol–gel bio-templating route. *J. Mater. Chem.* **20**, 1277–1284 (2010).

211. Parker, A. R., Welch, V. L., Driver, D. &Martini, N. Structural colour: Opal analogue discovered in a weevil. *Nature* **426**, 786–787 (2003).

212. Nagi, R. K., Montanari, D. E. &Bartl, M. H. Photonic crystal micro-pixelation and additive color mixing in weevil scales. *Bioinspiration and Biomimetics* **13**, 035003 (2018).

213. Ebihara, R., Hashimoto, H., Kano, J., Fujii, T. &Yoshioka, S. Cuticle network and orientation preference of photonic crystals in the scales of the weevil Lamprocyphus augustus. *J. R. Soc. Interface* **15**, 20180360 (2018).

214. Schultze, W. A monograph of the pachyrrhynchid group of the Brachyderinae, Curculionidae: part I. The genus Pachyrrhynchus germar. *Philipp. J. Sci.* **23**, 609–673 (1923).

215. Hiraku, Y. Notes on Pachyrhynchini jewel weevils (Coleoptera: Curculinidae: Entiminae) and other insects showing remarkable resemblance in color and body pattern characteristics. *Gekkan-Mushi* **553**, 22–40 (2017).

216. Rukmane, A. *New species of the genus Pachyrhynchus germar (Coleopetra, Curculionidae, Entiminae) from the Greater Mindanao Pleistocene Aggregate Island Complex (Philippines)*. *Acta Biologica Universitatis Daugavpiliensis* **17**, (2017).

217. Hsu, C. F., Tseng, H. Y., Hsiao, Y. &Ko, C. C. First record of the host plant and larvae of pachyrhynchus sonani (Coleoptera: Curculionidae) on Lanyu Island, Taiwan. *Entomol. Sci.* **20**, 288–291 (2017).

218. Welch, V., Lousse, V., Deparis, O., Parker, A. &Vigneron, J. P. Orange reflection from a three-dimensional photonic crystal in the scales of the weevil Pachyrrhynchus congestus pavonius (Curculionidae). *Phys. Rev. E - Stat. Nonlinear, Soft Matter Phys.* **75**, 041919 (2007).

219. Chen, Y. T. *et al.* Integrated species delimitation and conservation implications of an endangered weevil Pachyrhynchus sonani (Coleoptera: Curculionidae) in Green and Orchid Islands of Taiwan. *Syst. Entomol.* **42**, 796–813 (2017).

220. Wilts, B. D., Michielsen, K., DeRaedt, H. &Stavenga, D. G. Hemispherical Brillouin zone imaging of a diamond-type biological photonic crystal. *J. R. Soc. Interface* **9**, 1609–1614 (2012).

221. Huang, L. C. *et al.* Captive breeding of two insular populations of Pachyrhynchus sarcitis (Coleoptera: Curculionidae) from Lanyu and Babuyan Islands. *J. Asia. Pac. Entomol.* **21**, 1233–1238 (2018).

222. Kikuchi, D. W. &Pfennig, D. W. Predator cognition permits imperfect coral snake mimicry. *Am. Nat.* **176**, 830–834 (2010).

223. Kikuchi, D. &Pfennig, D. A Batesian mimic and its model share color production mechanisms. *Curr. Zool.* **58**, 658–667 (2012).

224. Noonan, B. P. &Comeault, A. A. The role of predator selection on polymorphic aposematic poison frogs. *Biol. Lett.* **5**, 51–54 (2009).

225. Comeault, A. A. &Noonan, B. P. Spatial variation in the fitness of divergent aposematic phenotypes of the poison frog, Dendrobates tinctorius. *J. Evol. Biol.* **24**, 1374–1379 (2011).

226. Kapan, D. D. Three-butterfly system provides a field test of müllerian mimicry . *Nature* **409**, 338–340 (2001).

227. Brower, L. P. &Brower, J. V. Z. The Relative Abundance of Model and Mimic Butterflies in Natural Populations of the Battus Philenor Mimicry Complex. *Ecology* **43**, 154–158 (1962).

228. Lindström, L., Alatalo, R.V &Mappes, J. Imperfect Batesian mimicry—the effects of the frequency and the distastefulness of the model. *Proceedings of the Royal Society B: Biological Sciences* **264**, 149–153 (1997).

229. Oaten, A., Pearce, C. E. M. &Smyth, M. E. B. Batesian mimicry and signal detection theory. *Bull. Math. Biol.* **37**, 367–387 (1975).

230. Sherratt, T. N. The evolution of imperfect mimicry. *Behav. Ecol.* **13**, 821–826 (2002).

231. Taylor, C. H., Reader, T. &Gilbert, F. Why many Batesian mimics are inaccurate: evidence from hoverfly colour patterns. *Proc. R. Soc. B Biol. Sci.* **283**, 20161585 (2016).

232. Penney, H. D., Hassall, C., Skevington, J. H., Abbott, K. R. &Sherratt, T. N. A comparative analysis of the evolution of imperfect mimicry. *Nature* **483**, 461–464 (2012).

233. Wallace, A. R. Darwinism (1889): An Exposition of the Theory of Natural Selection with some of its Applications. in 232–267 (Macmillan, 1901).

234. Wang, L.-Y., Huang, W.-S., Tang, H.-C., Huang, L.-C. &Lin, C.-P. Too hard to swallow: a secret secondary defence of an aposematic insect. *J. Exp. Biol.* **221**, 172486 (2018).

235. Barševskis, A. &Savenkov, N. Contribution to the knowledge of long-horned beetles (Coleoptera: Cerambycidae) in Latvia. *Balt. J. Coleopterol.* **13**, 91–102 (2013).

236. Sanson, G., Read, J., Aranwela, N., Clissold, F. &Peeters, P. Measurement of leaf biomechanical properties in studies of herbivory: Opportunities, problems and procedures. *Austral Ecol.* **26**, 535–546 (2001).

237. Evans, A. R. &Sanson, G. D. Biomechanical properties of insects in relation to insectivory: cuticle thickness as an indicator of insect hardness and intractability. *Aust. J. Zool.* **53**, 9–19 (2005).

238. Chapman, R. F., Simpson, S. J. &Douglas, A. E. *The Insects: Structure and Function*. (Cambridge University Press, 2013).

239. Pedrini, N., Ortiz-Urquiza, A., Huarte-Bonnet, C., Zhang, S. &Keyhani, N. O. Targeting of insect epicuticular lipids by the entomopathogenic fungus Beauveria bassiana: hydrocarbon oxidation within the context of a host-pathogen interaction. *Front. Microbiol.* **4**, 24 (2013).

240. Neville, A. C. Insect integuments. *Nature* **265**, 88 (1977).

241. van deKamp, T., Riedel, A. &Greven, H. Micromorphology of the elytral cuticle of beetles, with an emphasis on weevils (Coleoptera: Curculionoidea). *Arthropod Struct. Dev.* **45**, 14–22 (2016).

242. Andersen, S. O. 6 - Cuticular Sclerotization and Tanning. in *Insect Molecular Biology and Biochemistry* (ed. Gilbert, L. I.) 167–192 (Academic Press, 2012). doi:https://doi.org/10.1016/B978-0-12-384747-8.10006-6

243. Wigglesworth, V. B. The source of lipids and polyphenols for the insect cuticle: the role of fat body, oenocytes and oenocytoids. *Tissue Cell* **20**, 919–932 (1988).

244. Aberle, B., Jemmali, R. &Dirks, J.-H. Effect of sample treatment on biomechanical properties of insect cuticle. *Arthropod Struct. Dev.* **46**, 138–146 (2017).

245. Büsse, S. &Gorb, S. N. Material composition of the mouthpart cuticle in a damselfly larva (Insecta: Odonata) and its biomechanical significance. *R. Soc. Open Sci.* **5**, 172117 (2018).

246. Cribb, B. W. *et al.* Hardness in arthropod exoskeletons in the absence of transition metals. *Acta Biomater.* **6**, 3152–3156 (2010).

247. Broomell, C. C., Zok, F. W. &Waite, J. H. Role of transition metals in sclerotization of biological tissue. *Acta Biomater.* **4**, 2045–2051 (2008).

248. Schofield, R. &Lefevre, H. Short Communication: High Concentrations of Zinc in the Fangs and Manganese in the Teeth of Spiders. *J. Exp. Biol.* **144**, 577–581 (1989).

249. Andersen, S. O. Insect cuticular sclerotization: A review. *Insect Biochem. Mol. Biol.* **40**, 166 (2010).

250. Andersen, S. O. Chlorinated tyrosine derivatives in insect cuticle. *Insect Biochem. Mol. Biol.* **34**, 1079–1087 (2004).

251. Anbutsu, H. *et al.* Small genome symbiont underlies cuticle hardness in beetles. *Proc. Natl. Acad. Sci.* **114**, E8382--E8391 (2017).

252. van deKamp, T. &Greven, H. On the architecture of beetle elytra. *Entomol. heute* **22**, 191–204 (2010).

253. Zohry, N. M. H. &El-Sayed, A. M. Morphology, histology, and chemistry of the wings of Tribolium castaneum and Tribolium confusum (Coleoptera: Tenebrionidae). *J. Basic Appl. Zool.* **80**, 16 (2019).

254. Galusha, J. W., Jorgensen, M. R. &Bartl, M. H. Diamond-Structured Titania Photonic-Bandgap Crystals from Biological Templates. *Adv. Mater.* **22**, 107–110 (2010).

255. Lafait, J. *et al.* Modeling the vivid white color of the beetle Calothyrza margaritifera. *Mater. Sci. Eng. B* **169**, 16–22 (2010).

256. Dong, B. Q. *et al.* Optical response of a disordered bicontinuous macroporous structure in the longhorn beetle Sphingnotus mirabilis. *Phys. Rev. E* **84**, 11915 (2011).

257. Vigneron, J.-P., Bay, A., Colomer, J.-F., Hooijdonk, E.Van &Simonis, P. Optical reflectance and transmittance of photonic polycrystalline structures from living organisms. in *The Nature of Light: Light in Nature IV* (ed. Liang, R.) **8480**, 87–94 (SPIE, 2012).

258. Bermúdez-Ureña, E., Kilchoer, C., Lord, N. P., Steiner, U. &Wilts, B. D. Structural Diversity with Varying Disorder Enables the Multicolored Display in the Longhorn Beetle Sulawesiella rafaelae. *iScience* **23**, 101339 (2020).

259. Colomer, J.-F. *et al.* Photonic polycrystal in the greenish-white scales of the African longhorn beetle Prosopocera lactator (Cerambycidae). *Phys. Rev. E* **85**, 11907 (2012).

260. Simonis, P. &Vigneron, J. P. Structural color produced by a three-dimensional photonic polycrystal in the scales of a longhorn beetle: Pseudomyagrus waterhousei (Coleoptera: Cerambicidae). *Phys. Rev. E* **83**, 11908 (2011).

Appendix

Table S1 Literature reported photonic structures and structural parameters such as the lattice constant (***a***), the filling fraction of cuticles in a scale (***FF***), crystal orientations of weevils belong to Curculionidae family.

Photonic structure	**Species**	***a* (nm)**	***FF***	**Orientations**	**Reflected wavelength (nm)**
Amorphous	*Pachyrhynchus fimbriatus* [206]	241.42	-	-	-
	Pachyrrhynchus forsteni [206]	302.68	-	-	-
hexagonally ordered air in a cuticle matrix	*Lamprocyphus augustus* [205]	450± 90	-	(210) (110) (100)	541- 598 555- 614 586- 647
	Eupholus chevrolati [212]	360(blue-yellow) 400(green- red)	-	(210)(110)(100)(111)(411)	475- 570
	Pachyrhynchus moniliferus [210]	410(green) 510 (red)	0.5	-	-
	Eupholus schoenherri [210]	380	0.5	-	-
Single diamond ($Fd\bar{3}m$)	*Pachyrrhynchus reticulatus* [206]	443.43	-	(111)(110)(311) (331)(310)	576.5
	Pachyrrhynchus venustus [206]	476.59	-	(111)(110)(311)(331)(852)(551)	-
	Lamprocyphus augustus [207]	401	0.53	(111)	gold 604
	Pachyrhynchus congestus [209]	418.3 (blue) 457.9 (yellow)	0.36(yellow) <0.3(green, blue)	(111)	565- 645
	Entimus imperialis [63]	445± 10	0.3	$(2\bar{1}0)(3\ 2\ 12)$ $(24\bar{1})(834)(524)$	480- 610
	Entimus imperialis[206]	466.98	-	(111)(110)(311) (430)(211)(551)	-
	Pachyr*hynchus orbifer* (green) [206]	449	-	(111)(311)(331) (322)(551)	-
	Pachyr*hynchus orbifer* (orange) [206]	469.5		(111)(311)(331)	
	Eupholus sp [207]	-	-	-	-
	Apodrosus viridium [207]	-	-	-	-
	Pachyrhynchus rufopunctatus [206]	506.69	-	(111)(110)(311) (211)(331)	-
Single diamond	*Lamprocyphus augustus* [206]	374.96	-	(111) (211) (110) (321)	587.1

($Fd\bar{3}m$) + single gyroid ($I4_132$)	*Pachyrrhynchus reticulatus* [206]	468.39	-	(111) (110)(311)	652.5
Face centered orthorhombic (Fddd)	*Apodrosus viridium* [206]	474.15	-	(111)(110)(100) (210)(773)	-

Table S2 Literature reported photonic structures and structural parameters such as strut geometry, the filling fraction of cuticles in a scale ***FF***, crystalline of longhorn beetles belong to Cerambycidae family.

Photonic structure	**Species**	***FF***	**Reflected wavelength (nm)**
Amorphous	*Sphingnotus mirabilis* [256]	0.49	560
Amorphous	*Anoplophora graafi* [107]	-	360, 550
Amorphous	*Calothyrza margaritifera.*[257]	-	white
Multilayer	*Sulawesiella rafaelae* [258]	0.470 (orange) 0.457 (yellow-green) 0.464 (turquoise)	700 (orange) 560 (yellow-green) 490 (turquoise)
Multilayers	*Tmesisternus isabellae* [104]	0.85 (H layer) 0.15 (IH layer)	600
Opal structures	*Prosopocerus lactator* [259]	-	520 nm (green) 850 nm (infrared)
Opal structures	*Pseudomyagrus waterhousei* [260]		Blue
Opal structures	*Acronia alboplagiata* (this study)	-	Pale green
Opal structures	*Acronia decimaculata* (this study)	-	yellow